UNIVERSIDADE DE BRASÍLIA – UnB
INSTITUTO DE GEOCIÊNCIAS – IG
PROGRAMA DE PÓS-GRADUAÇÃO EM GEOLOGIA

GEOLOGIA, GEOCRONOLOGIA, PETROLOGIA E METALOGÊNESE DO PROSPECTO Cu-Mo YANAC, ICA, PERU

DISSERTAÇÃO DE MESTRADO Nº 323

Carlos Javier Collado Medina

Brasília, DF, maio de 2014

UNIVERSIDADE DE BRASÍLIA – UnB
INSTITUTO DE GEOCIÊNCIAS – IG
PROGRAMA DE PÓS-GRADUAÇÃO EM GEOLOGIA

GEOLOGIA, GEOCRONOLOGIA, PETROLOGIA E METALOGÊNESE DO PROSPECTO Cu-Mo YANAC, ICA, PERU

Carlos Javier Collado Medina

Orientadora:

Prof. Dra. Márcia Abrahão Moura

Banca Examinadora:

Prof. Dra. Márcia Abrahão Moura (UnB)

Prof. Dra. Lena Virginia Soares Monteiro (USP)

Prof. Dr. Valmir da Silva Souza (UnB)

Brasília, DF, maio de 2014

RESUMO

O prospecto Yanac está localizado no nordeste de Chincha Alta, Ica, Peru, na superunidade Incahuasi, dentro do segmento Arequipa do batólito costeiro de Peru e na extremidade noroeste da faixa metalogenética de cobre do Cretáceo Superior dos Andes.

Três principais rochas graníticas, contemporâneas com enclaves e diques interminerais diorito-gabróicos, dioríticos e monzodioríticos foram definidas no prospecto Yanac. Primeiramente, a rocha hospedeira do sistema porfirítico Yanac, com idade U/Pb em zircão de 70,6 ± 1,0 Ma, é um granodiorito equigranular com granulação média a grossa, pertencente à superunidade Incahuasi do batólito costeiro. Com uma diferença desprezível de edade e um erro dentro de 1 Ma., ambos, O granodiorito Incahuasi é intrudido por um granodiorito porfirítico, com granulação fina a média, com idade U/Pb em zircão de 71,0 ± 1,0 Ma, e por um granodiorito-diorito porfirítico, com granulação média a grossa, com idade U/Pb em zircão de 67,75 ± 0,80 Ma. Diques traquidacíticos e basálticos cortam as rochas graníticas. Eles são pós-mineralização e podem estar relacionados com os eventos de alojamento do batólito costeiro.

O granodiorito Incahuasi, o granodiorito porfirítico e o granodiorito-diorito porfirítico possuem características petrográficas de magmas oxidados. Geoquimicamente, as rochas graníticas, os diques interminerais e enclaves que ocorrem nos granitos possuem composição cálcio-alcalina, metaluminosa, de magmas do tipo I de arcos vulcânicos. Eles possuem biotita primária de composição annita-flogopita, compatível com biotita de magmas de suítes orogênicas cálcio-alcalinas, e anfibólio no campo da magnésio-hornblenda. O dique basáltico é geoquimicamente semelhante a magmas do tipo-I, enquanto o dique traquidacítico possui características geoquímicas de magmas do tipo S.

Valores de $\varepsilon Hf(T)$ entre -0,28 e +6,65 e de Hf T_{DM} entre 460 e 740 Ma para o granodirito porfirítico e granodiorito-diorito porfirítico, juntamente com εNd(t) entre -1,11 e 1,72, e ^{87}Sr/^{86}Sr entre 0,70450 e 0,70472, e valores de Nd T_{DM} entre 520 e 850 Ma para o granodiorito Incahuasi, granodiorito porfirítico, granodiorito-diorito porfirítico, diques interminerais, enclaves e diques basálticos, sugerem derivação de manto subcontinental, com restritos componentes crustais de sedimentos oceânicos reciclados ou embasamento Pré-Cambriano, e semelhante tendência de evolução. O

dique traquidacítico possui εNd(t) de -2,33, $^{87}Sr/^{86}Sr$ de 0,70778 e Nd T_{DM} de 850 Ma, coerentes com derivação na crosta superior.

As rochas graníticas foram submetidas a diferentes tipos de alteração hidrotermal no prospecto Yanac. A alteração propilítica é menos enriquecida em Cu-Mo e circunscrita às zonas laterais do sistema. É caracterizada por vênulas designadas de subtipo A1, com quartzo-clorita-albita-carbonatos-pirita±calcopirita; A2, com pirita-quartzo±calcopirita±molibdenita; e A3, com assembleias de K-feldspato-epidoto-clorita-pirita±calcopirita. A alteração fílica é mais central e mais enriquecida em Cu-Mo. É caracterizada por diferentes tipos de vênulas. O primeiro, caracterizado como fraca alteração filica cortada por expressivos stockworks, representados pelas vênulas do subtipo B1, com assembleia de quartzo-pirita-calcopirita-molibdenita e fraco halo de alteração de sericita-albita; B2, com quartzo-sericita e halo de albita, com sutura de pirita-molibdenita-calcopirita±K-feldspato; B3, com sericita-clorita-quartzo-pirita±calcopirita; e B4, com quartzo-pirita e com um bem pronunciado halo de sericita atingindo até 2 cm de espessura; e o segundo, caracterizado como forte alteração fílica, representada pelas vênulas do tipo B5, com quartzo-sericita-pirita±albita, destrói completamente a textura original da rocha. Uma zona restrita, contendo brecha hidrotermal, pode ser caracterizada por fraca alteração fílica, pela similaridade da assembleia de alteração e mineralização com o evento B. A alteração mais jovem observada é dominada por vênulas locais designadas C1, com associação de laumontita-quartzo-adulária.

O granodiorito-diorito porfirítico é interpretado como sendo o responsável pela geração de soluções hidrotermais e enriquecimento em Cu e Mo, por sua intrusão tardia em relação às outras fases pré-existentes, a posição espacial da brecha hidrotermal, presença moderada a pervasiva de *stockworks* e teores altos de Cu e Mo relacionados à alteração fílica.

Processos supergênicos tardios e erosão em Yanac definem uma fina zona de oxidação-lixiviação.

Com base no estilo da mineralização, rocha hospedeira, metais, alteração hidrotermal e minerais metálicos, o prospecto Yanac é interpretado como semelhante a depósitos do tipo Cu(-Mo) pórfiro. Considerando-se a mineralização como tendo a

idade mínima de 67,75 ± 0,80 Ma., Yanac situa-se no cinturão cuprífero peruano do Cretáceo Superior.

Recomenda-se investigação nas porções mais profundas do prospecto, com o objetivo de verificar a existência de assembleias hidrotermais de alta temperatura e possíveis teores mais elevados de metais. Concentrações econômicas de Cu-Mo na transição pórfiro-epitermal em Yanac e regiões vizinhas também devem ser consideradas. À medida que mais ocorrências e depósitos sejam estudados ao longo do cinturão metalogenético do Cretáceo Superior dos Andes Centrais, no sul do Peru, é possível que outros depósitos de Cu-Mo ± Au sejam descritos com características semelhantes às de Yanac.

Palavras-chave: Peru, Yanac, pórfiro, metalogênese, cobre, molibdênio, alteração hidrotermal, geocronologia, petrologia, geoquímica, isótopos radiogênicos, Cretáceo.

ABSTRACT

The Yanac prospect is located at northeast of Chincha Alta, Ica Region, Peru, in the Arequipa segment of the coastal batholith of Peru and in the northwestern end of the late Cretaceous copper metallogenic belt of the Andes.

Three major granitic rocks, contemporaneous with gabbroic diorite-diorite-monzodiorite intermineral dykes and enclaves, were defined at Yanac prospect. The host rock of the Yanac porphyritic system, with U/Pb zircon age of 70.6 ± 1.0 Ma, is a medium to coarse-grained equigranular granodiorite from the Incahuasi superunit of the coastal batholith. With an inconsiderable difference age and error within of 1 Ma., both, the Incahuasi granodiorite is intruded by a fine to medium-grained porphyritic granodiorite, with U/Pb zircon age of 71.0 ± 1.0 Ma, and by a medium to coarse-grained porphyritic granodiorite-diorite, with U/Pb zircon age of 67.75 ± 0.80 Ma.

Finally, trachydacite and basaltic dykes cut the porphyry system. They are post-mineralization and could be related with the emplacement events of the coastal batholith.

The Incahuasi granodiorite, the porphyritic granodiorite and the porphyritic granodiorite-diorite have petrographic characteristics of oxidized magmas. Geochemically, the granitic rocks, the dykes and the enclaves that occur in the granites have calc-alkaline and metaluminous composition, similar to I-type magmas from volcanic arcs. They have primary annite-phlogopite biotite, compatible with calc-alkaline orogenic suites, and magnesium-hornblende amphiboles. The basaltic dyke is geochemically similar to I-type magmas, while the trachydacitic dyke has S-type magma signature.

Values of εHf(T) from -0.28 to +6.65 and Hf T_{DM} from 460 to 740 Ma for the porphyritic granodiorite and porphyritic granodiorite-diorite, together with εNd(t) from -1.11 to 1.72, $^{87}Sr/^{86}Sr(i)$ between 0.70450 and 0.70472, and Nd T_{DM} values from 520 to 850 Ma. for the Incahuasi granodiorite, porphyritic granodiorite, porphyritic granodiorite-diorite, intrusive intermineral dykes, enclaves and basaltic dykes, suggest a subcontinental mantle derivation, with minor crustal component of recycled oceanic sediments or precambrian basement, and a similar evolution trend. They are considered as the source of magmas and of Cu-Mo metals. The trackydacite dyke has εNd(t) of

-2.33, $^{87}Sr/^{86}Sr(i)$ of 0.70778 and T_{DM} of 850 Ma., coherent with derivation from the upper crust.

The granitic rocks underwent different types of hydrothermal alteration at Yanac. A less enriched Cu-Mo propylitic alteration is mostly restricted to lateral zones and is characterized by A1 subtype veinlets with quartz-chlorite-albite-carbonates-pyrite±chalcopyrite; A2, with pyrite-quartz±chalcopyrite±molybdenite; and A3, with K-feldspar-epidote-chlorite-pyrite±chalcopyrite assemblages. A more Cu-Mo enriched central phyllic alteration in the system is characterized by different subtypes of veinlets. First, by a weak phyllic alteration, with high stockwork intensity, represented by B1 subtype veinlets, composed of quartz-pyrite-chalcopyrite-molybdenite, and weak alteration halo of sericite-albite; B2, with quartz-sericite, and albite halo, and pyrite-molybdenite-chalcopyrite±K-feldspar suture; B3, with sericite-chlorite-quartz-pyrite±chalcopyrite; and B4, with quartz-pyrite with a very pronounced sericite halo reaching up to 2 cm thick; and second, by a strong phyllic alteration, represented by B5, with quartz-sericite-pyrite±albite veinlets, that completely destroy the original texture of the rock. The hydrothermal breccia may be characterized by a weak phyllic alteration by its similarity of alteration and mineralization assemblage in event B. The latest veins observed are dominated by local C1 veinlets, with laumontite-quartz-adularia association.

The porphyritic granodiorite-diorite is interpreted as the responsible for the generation of hydrothermal solutions and Cu and Mo enrichment, by its later emplacement, the spatial position of the hydrothermal breccia, moderate to pervasive stockwork structures and higher Cu and Mo values related to the phyllic alteration.

Subsequent supergenic process and erosion at Yanac define a thin oxidation-leached zone.

Based on the style of the mineralization, the host rock, the metals, the hydrothermal alteration and the metallic minerals, Yanac is interpreted as similar to porphyry Cu(-Mo) deposits. Considering the mineralization as having the minimum age of 67.75 ± 0.80 Ma, it is situated within the upper Cretaceous metallogenic copper belt of the Peruvian Andes.

Investigation in deeper parts of the prospect is encouraged, in order to verify the existence of high temperature hydrothermal assemblages and possible higher metal concentrations. Economic concentrations of Cu-Mo in the transition porphyry-epithermal at Yanac and nearby should also be considered. It is possible that as more deposits are studied along the metallogenetic late Cretaceous belt of the Central Andes, in southern Peru, other Cu-Mo±Au deposits with characteristics similar to Yanac are described.

Keywords: Peru, Yanac, porphyry, metalogenesis, copper, molybdenum, hydrothermal alteration, geochronology, petrology, geochemistry, radiogenic isotopes, Cretaceous.

SUMÁRIO

LISTA DE FIGURAS

LISTA DE TABELAS

CAPÍTULO 1 – INTRODUÇÃO

1.2. APRESENTAÇÃO

O prospectoYanac está localizado no lado oeste da Cordilheira ocidental dos Andes, possivelmente na faixa metalogénica de cobre do Cretáceo Superior, que contém um grupo de depósitos do tipo pórfiro orientados segundo NW – SE, no noroeste da cidade de Arequipa. Yanac situa-se no extremo noroeste da faixa; os outros depósitos incluem Almacen, Lara, Puquio, Pucacorral Sur, Zafranal, Angostura, bem como várias pequenas ocorrências (Sillitoe e Perello, 2005). Em Yanac, ocorrem associações de alteração e mineralização de quartzo-pirita-calcopirita-molibdenita-sericita-clorita em vênulas e disseminações, hospedados em rocha granodiorítica equigranular média do Batólito da Costa, cortado por intrusões de granodiorito e diorito porfirítico. Trabalhos anteriores de campo no prospecto Yanac e as primeiras interpretações da Estrella Gold Peru S.A.C. (2011) sugeriram que esses dados eram evidência de um possível modelo do tipo Cu-pórfiro.

Embora o plutonismo de arco e a mudança do ângulo de subdução, de um ângulo elevado no Jurásico e Cretáceo inferior para outro menos inclinado a partir do Cretáceo superior possa ser relacionado contemporaneamente com a mineralização de muitos depósitos andinos (Sillitoe e Perelló, 2005), ainda existem em Yanac grandes incertezas quanto ao tipo de magma associado, sua origem, sua relação espacial com o minério e a alteração e a natureza do embasamento subjacente.

Este trabalho teve o objetivo de investigar o possível tipo de modelo mineral existente em Yanac, seu contexto geológico e petrológico, sua relação espacial com as faixas metalogênicas de cobre presentes na região sul peruana, assim como as relações temporais entre a mineralização de Cu (± Mo, Au) e as rochas magmáticas e hidrotermais da área, visando à proposição de um modelo metalogenético para o prospecto.

As interpretações apresentadas baseiam-se em detalhado estudo da geologia local, petrografia de rochas encaixantes e hospedeiras da mineralização, dados litogeoquímicos e de microssonda eletrônica, geocronologia por U-Pb e isótopos de Lu-

Hf em zircão nas rochas magmáticas, assim como isótopos radiogênicos de Rb-Sr e Sm-Nd em rocha total. As conclusões deste estudo têm implicações para a maior compreensão da geologia, geocronologia, petrologia e metalogenia do prospecto Yanac em relação aos afloramentos e depósitos similares presentes na Cordilheira Ocidental do sul do Peru.

1.2. LOCALIZAÇÃO E ACESSO

A área de estudo encontra-se localizada no Peru, na Região de Ica, aproximadamente 35 km ao nordeste da cidade de Chincha Alta (Fig. 1.1). Essa região constitui o lado oeste da Cordilheira Ocidental e a parte central dos Andes sul-americanos. Trata-se de uma zona relativamente habitada, de fácil acesso e com estrada em boa condição. O acesso a partir das principais cidades pode ser conseguido tomando a rodovia principal da Panamericana, seguindo a rota Lima-Chincha Alta por aproximadamente 200 Km (2 horas). Em Chincha Alta, pode-se continuar de carro pela estrada de terra que leva até o prospecto Yanac (Fig. 1.1), por aproximadamente 40 Km (1 hora e 30 minutos).

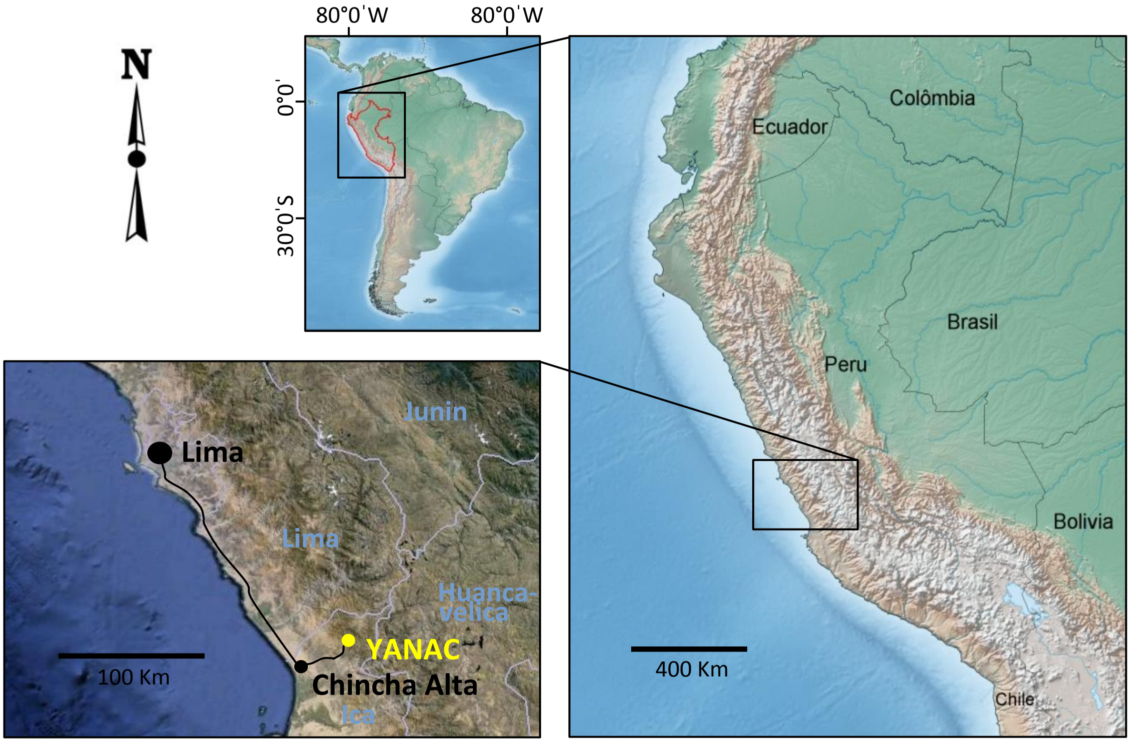

Figura 1.1. *Área de estudo, localizada no lado oeste da Cordilheira Central dos Andes. As linhas cinza indicam os limites regionais do Peru. Informação geográfica e topográfica obtida de www.naturalearthdata.com e Google Earth.*

1.3. OBJETIVOS

O objetivo geral deste trabalho foi integrar dados geológicos, geocronológicos e petrológicos para aprofundar o conhecimento do prospecto de Cu-Mo Yanac e propor um modelo metalogênico para as mineralizações na área de estudo.

Dentre os objetivos específicos estão caracterizar a mineralização de cobre e molibdênio, sua paragênese e sua relação com a alteração hidrotermal, contribuir para o conhecimento da geologia local do prospecto Yanac, em particular das rochas intrusivas em que está hospedada a mineralização, bem como do seu contexto metalogénico regional.

CAPÍTULO 2 – CONTEXTO GEOLÓGICO REGIONAL

2.1. CONTEXTO ANDINO PERUANO

A Cordilheira dos Andes, parte integrante do Ciclo Alpino mundial, se formou no limite entre a Placa Oceânica Pacífica e a Placa Sul Americana. Estende-se em uma faixa estreita ao longo de toda América do Sul (Fig. 2.1a) para logo continuar na América do Norte tendo o nome de Montanhas Rochosas.

Os Andes Peruanos compreendem um conjunto de cordilheiras localizadas entre a Fossa Peruana - Chilena e a Planície Amazônica (Fig. 2.1b). Toda a estratigrafia, estruturas, magmatismo, mineralização e sismicidade da Cordilheira dos Andes e do território peruano são direta ou indiretamente o resultado da subdução da Placa de Nazca por baixo da Placa Sul Americana, ao que se denomina “Subdução Andina” e que se tipifica como uma cordilheira peri-oceânica característica (Chacón, 1995).

O território peruano se localiza na costa central e ocidental da América do Sul, entre 0º e 18º20’ de Latitude Sul, e 68º30’ e 81º25’ de Longitude Oeste, abrangendo uma superfície de 1’285,215 km^2. Grande parte do território compreende a Cordilheira dos Andes, a qual se estende do Sul ao Norte ao longo de toda a América do Sul. A característica orográfica mais proeminente no Peru forma a Cordilheira Ocidental que se constitui na divisória continental entre as bacias hidrográficas do Pacífico e do Atlântico.

A Cordilheira dos Andes determina no território peruano diferentes unidades geomorfológicas próprias de um meio continental e um meio marinho. No âmbito continental, as unidades geomorfológicas, localizadas de Oeste a Leste, correspondem a (1) Cordilheira da Costa, (2) Planície Preandina (Faixa Costeira), (3) Cordilheira Ocidental, (4) Depressões Inter-andinas, (5) Cordilheira Oriental, (6) Bacia de Titicaca, (7) Cordilheira Sub-andina (8) Planície Amazônica e (9) Faixa de cones vulcânicos (Fig. 2.1b). No âmbito marinho, a morfologia submarinha compreende: (1) Plataforma Continental, (2) Talude Continental, (3) Fossas Marinhas (Fossa Peruana - Chilena), (4) Dorsal de Nazca, (5) Fundos Abissais do Pacífico Sul. A geografia do seu território é o resultado de uma antiga evolução de relevos anteriores.

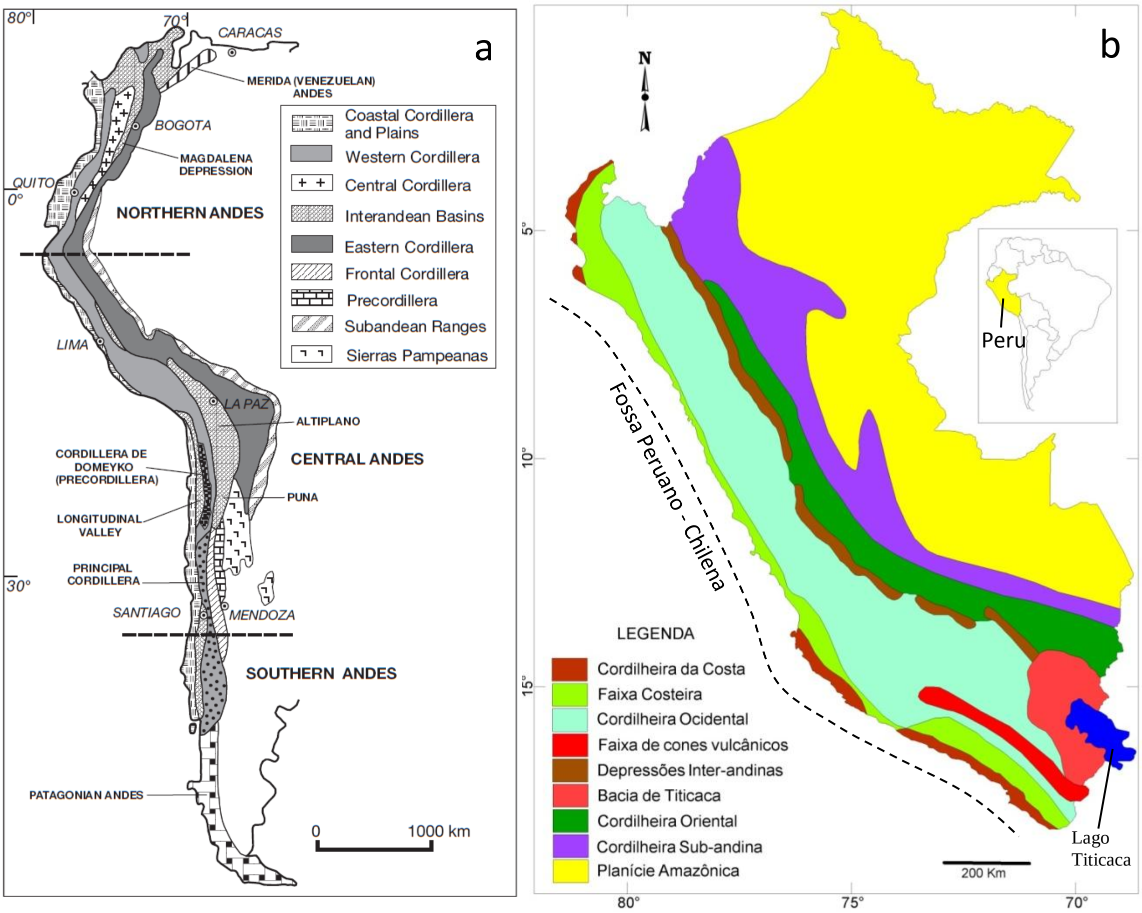

Figura 2.1. *(a) Mapa dos Andes Sul-americanos mostrando suas principais províncias fisiográficas (simplificado de Corvalán, 1990, em Sillitoe e Perelló, 2005) (b) Mapa de unidades morfoestruturais detalhadas do Peru (Tumialán, 2003).*

A geologia histórica baseada no conhecimento da evolução da sua paleogeografía pelo tempo, assim como dos ciclos orogênicos que foram formando suas cadeias montanhosas, nos permite ter um panorama de como foi se modelando o relevo do território até chegar à geografia atual, compreendendo neles várias etapas de sedimentação, de deformação, levantamentos e, finalmente, de erosão e peneplanização.

O sistema andino no Peru tem uma orientação geral NW-SE, que está associado aos principais elementos estruturais tais como eixos de dobramentos, falhas, elongação de corpos intrusivos maiores, alinhamento de cones vulcânicos, etc.

O primeiro perfil da Cordilheira e o início da Subdução Andina são produzidos no Paleozoico superior (Permiano), durante a Fase Tectônica Tardihercínica. Esta fase se reconheceu em muitas cordilheiras e é considerada como a responsável do início da deriva continental, reajuste e ordenamento das placas da Terra. É caracterizada pela deformação originada por fraturas associadas a grandes falhas do tipo de desgarre, inversas e transformantes, muitas das quais limitam as placas tectônicas. Uma das falhas inversas foi a que inicialmente formou a Cordilheira dos Andes, em rochas do embasamento precambriano e paleozóico, que constituem as raízes andinas; mas a subdução propriamente dita só começa a aparecer no decurso da abertura do Atlântico, datada entre 180 e 130 M.a. Entre estas primeiras deformações se localiza a Bacia Peruana, que evolui posteriormente ao denominado "Geossinclinal Andino" (Palacios *et al.*, 1995).

O Continente Sul Americano se formava com a África, Oceania, Índia e a Antártida, o Continente Gondwana, o mesmo que foi parte de outro continente ainda maior, denominado Pangea, cuja ruptura deve ter ocorrido ao final do Paleozóico e começo do Mesozóico. Esta ruptura separa ao Norte o Continente de Laurasia e ao Sul o Continente de Gondwana, localizando-se entre eles o mar de Thetis (Palacios *et al.*, 1995).

No Gondwana, a separação da América do Sul e da África ocorreu entre o Jurássico-Cretácio, dando lugar à abertura do Atlântico Sul e à deriva da América do Sul para oeste (Palacios *et al.*, 1995).

O território peruano é formado por ampla sequência de rochas sedimentares, vulcânicas e metamórficas, cortadas por importantes corpos plutônicos. Estas rochas variam em idades que vão desde o precambriano até o Quaternário recente (Fig. 2.2, Fig. 2.3).

As rochas mais antigas que se encontram no território peruano pertencem ao Pré-Cambriano (Fig. 2.2), como remanescentes de antigas cordilheiras, cuja história é difícil de decifrar, pois perderam suas características. Os ciclos sedimentares e os episódios orogênicos durante o Pré-cambriano são pouco conhecidos, devido a que as rochas foram metamorfisadas, a tal ponto que suas características originais foram apagadas (Palacios *et al.*, 1995).

Estudando a coluna estratigráfica, pode-se estabelecer que as rochas Pré-cambrianas correspondem pelo menos a dois ciclos orogênicos ainda pouco conhecidos, sendo o mais evidente a Orogenia Brasílida cuja cadeia montanhosa provavelmente se formou no Precambriano superior (600 M.a.; Dalmayrac, et. al., 1980; Tabela 2.1).

As rochas precambrianas compõem o embasamento cristalino do território peruano. São constituídas por um complexo de rochas metamórficas e ígneas nas quais se destacam corpos graníticos alcalinos e, em menor proporção, corpos básicos e ultrabásicos.

No Peru as rochas precambrianas agrupam-se em duas séries: a mais antiga, localizada na Cordilheira da Costa, com idade de 600 a 2000 M.a., conhecida como Complexo Basal da Costa (Bellido e Narváez, 1960); e a mais jovem, a Série Metamórfica da Cordilheira Oriental, com idade de 600 a 640 M.a., formando o núcleo da cordilheira mencionada (Dalmayrac, et. al., 1980, Fig. 2.1b, Fig. 2.2).

Nas rochas paleozoicas (Fig. 2.2), são reconhecidas a Orogenia Caledônica, a noroeste, e a Orogenia Hercínica, na Cordilheira Oriental (Tabela 2.1), com dois ciclos sedimentares: um no Paleozóico inferior e outro no Paleozóico superior, culminando cada um deles com uma fase de deformação. A primeira fase é denominada Fase Eohercínica (340 M.a.); a segunda, Fase Tardihercínica (280 M.a.); e a última, Fase Finiherciniana (Triássico Inferior) (Dalmayrac, et. al., 1980; Tabela 2.1).

O Paleozóico Inferior compreende uma série metamórfica pré-Ordoviciana e uma segunda série Ordovíciana-Devoniana. A série Ordoviciana-Devoniana foi depositada em um geossinclinal entre a Cordilheira da Costa e o Plano Amazônico (Fig. 2.1b, Fig. 2.2). Compreende sequências clásticas marinhas, pelíticas e arenosas, que alcançam grande desenvolvimento na Cordilheira Oriental meridional, onde a espessura pode ser maior que 10.000 m (Palacios, 1995).

O Paleozóico superior (Fig. 2.2) compreende o Carbonífero e Permiano. Inicia-se com uma série continental do Mississipiano que inclui níveis marinhos (Grupo Ambo), seguida de uma série marinha do Pensilvaniano ao Permiano inferior (Grupos Tarma y Copacabana), e logo por uma série molássica continental (Grupo Mitu) (Palacios, 1995).

Nas rochas mesozóicas e cenozóicas (Fig. 2.2) reconhece-se o Ciclo Andino, que compreende várias etapas de sedimentação e várias fases de deformação. As principais são a Fase Peruana, ocorrida no Cretácico superior (80 M.a.), a Fase Incaica, no

Terciário inferior (35-30 M.a.), seguida pela Fase Quechua (12-15 M.a.) e outras no fim do Terciário e começo do Quaternário (Tabela 2.1).

A sedimentação marinha na Bacia Peruana é contínua entre o Triássico e Cretáceo inferior (Fig. 2.2), com aportes sedimentares da Cordilheira da Costa ao Oeste e do Geoanticlinal do Marañón ao Leste. Nesta época, na zona de subdução, são geradas abundantes fraturas no embasamento precambriano-paleozóico ao longo do eixo da bacia, as mesmas que conectam o Manto superior com a Bacia Peruana, permitindo que a sedimentação marinha seja constantemente interrompida por derrames vulcânicos submarinos, e fora dela, que a sedimentação se realize sem interrupções magmáticas. A presença do vulcanismo submarino dá como resultado duas sequências estratigráficas características do Geossinclinal Andino: uma intercamada vulcânica - sedimentar ao Oeste da Bacia que tipifica ao Eugeossinclinal, e ao Leste uma sedimentação meramente clástica que caracteriza ao Miogeossinclinal Andino (Palacios *et al*., 1995).

Durante a Fase Tectônica do Cretáceo superior - Terciário inferior (Tabela 2.1) se acentua o dobramento e epirogênese andina. Simultaneamente, ao longo da zona do Eugeossinclinal Andino se localizam a Oeste os demais complexos intrusivos do Batólito da Costa em vários pulsos magmáticos que duram entre 102 e 53 M.a. (Fig. 2.2, Fig. 2.3), e ao Leste, o vulcanismo continental dos Grupos Toquepala e Calipuy no Sul e Norte do Peru respectivamente (Palacios *et al*., 1995).

Durante o Mesozoico se desenvolveu o “Ciclo Andino” cuja sedimentação teve lugar numa bacia geossinclinal marginal ao continente sulamericano; seu eixo longitudinal coincide com a Cordilheira Ocidental (Fig. 2.1b). A sedimentação inclui fácies vulcano - sedimentares na parte mais ocidental (faixa Costeira) e fácies sedimentares na parte central da bacia. A sedimentação mesozoica está acompanhada por mudanças laterais e verticais, os primeiros devido à paleorelevos entre as diferentes sub bacias, e os segundos a movimentos oscilatórios aos que estiveram sometidas essas bacias. A sedimentação se desenvolve desde o Triássico meio até o Cretáceo superior, um lapso de mais de 150 milhões de anos, tendo acumulado uma sequência integrada superior aos 20,000 m (Palacios *et al*., 1995).

O Cenozóico terciário no território peruano compreende sequências sedimentares de fácies marinhas na costa, vulcânico - sedimentares de fácies continentais nos Andes e sedimentares de fácies continental na Região Subandina e na Planície Amazônica (Palacios, 1995; Fig. 2.2).

Edade Absoluta	Era	Período / Piso		Ciclo	Fase
1.8	CENOZÓICO	Quaternário	Pleistoceno	ANDINO	**Fase Quechua 3?** Lev., Falham., Vulcanismo
		Neógeno	Plioceno		**Fase Quechua 2** Lev., Falham., Vulcanismo
			Mioceno		**Fase Quechua 1** (Compressiva) acompanhado de falhamento, levantamento e erosão que gerando o plano Puna, e depois vulcanismo explosivo.
		Paleógeno	Oligoceno		
			Eoceno Paleoceno		**Fase Inca** Fortemente compressiva, gera dobramentos, falhas inversas. Posterior vulcanismo generalizado na Cordilheira Ocidental.
64	MESOZÓICO	Cretáceo	Daniano Maastrichtiano Campaniano		
			Santoniano Coniaciano Turoniano Cenomaniano Albiano Aptiano Barremiano		**Fase Peruana** (Compressiva) gerando dobramentos regionais, falhamentos e fraturamentos **Fase Mochica** Esfoço de contraçao prévia ao Batólito da Costa **Fase Inter Albiana** Localizada na parte central movimentos de deformação prévia a orogenia propriamente ditada
		(Neocomiano)	Hauteriviano Valanginiano Berriasiano		
130		Jurássico (Malm)	Titoniano Kimmeridgiano Oxfordiano		**Movimento Nevadino** Epirogenia levantamento em blocos, geram a separação de duas bacias no Norte e Centro do Perú
		(Dogger)	Caloviano Batoniano Bajociano Aaleniano		
		(Lias)	Toarciano Pliensbachiano Sinemuriano Hettangiano		
190		Triássico Sup.	Retiano Noriano		
		Meio	Carniano Landiniano		
250		Inf.	Anisiano Scythiano		**Fase Finiherciniana:** Deformação localizada no Perú Central
265	PALEOZÓICO	Pérmico	Ochoano Guadalupano Leonardiano Wolfcampiano	Hercínico	**Fase Tardehercínica** (Compressiva) movimento epirogênico de levantamento com dobramento no Sul
290		Pensilvaniano	Stephaniano Westphaliano		
		Mississipiano	Viseano Toumesiano		
355		Devónico	Famenniano Frasniano Givetiano Eifiliano Emisiano Siegeniano Gediniano		**Fase Eohercínica** (Compressiva) Forte dobramento, falhamento e metamorfismo epizonal
410		Silúrico	Ludloviano Wenlockiano Llandoveriano		
438		Ordovícico	Ashigiliano Caradociano Llandeiliano Llanvimiano Arenigiano Tremadociano	Caledoniano	**Fase Compressiva** no Noroeste Movimentos epirogênicos sem deformaçção no Sudeste. Plutonismo na costa Sul.
510 570		Câmbrico	?		
1000	NEOPROTEROZÓICO			Brasilida	**Fase 1** Compressão gerando microdobramento **Fase 2** Xistosidade, metamorfismo epitermal e catazonal **Fase 3** Redobramento da xistosidade II **Fase 4** Dobramento em chevron
1600	MESOPROTEROZÓICO			Transamazônica ?	

Tabela 2.1. *Quadro de idades e os seus ciclos orogênicos correspondente do Pré-cambriano ao Cenozóico (Palacios et al., 1995).*

Durante o Quaternário, depositam-se no território peruano sedimentos de origem vulcânica, glaciares, aluviais, lacustres, marinhos e eólicos (Fig. 2.2). Evidenciam-se principalmente abundantes falhas recentes, dobras observadas na Bacia de Huancayo em depósitos do Quaternário antigo, o levantamento da "Superfície Puna" de idade Plioceno-Quaternaria, o vulcanismo quaternário e o levantamento dos terraços marinhos; assim como a atividade sísmica e vulcânica que ocorre no Peru, caracterizando os Andes como um ativo cinturão sísmico (Palacios *et al*., 1995).

As rochas sedimentares se localizam nas diversas bacias da Cordilheira dos Andes peruanos, tendo sido depositadas em ambientes de fácies marinhas e continentais. As rochas vulcânicas se encontram intercaladas com as rochas sedimentares em numerosas bacias. As rochas metamórficas são produto de processos de metamorfismo regional e de contato, as primeiras por efeitos do tectonismo compressivo e incremento de temperatura durante a formação da Cordilheira dos Andes, e as segundas, por efeito térmico durante a localização dos batólitos e corpos plutônicos (Palacios *et al*., 1995).

A geologia peruana apresenta evidências de intenso magmatismo ocorrido em forma descontínua, como atividade plutônica e/ou vulcânica, em determinadas épocas geológicas desde o Proterozóico até o Holoceno. A relação dos eventos magmáticos ao Plano de Bennioff é evidente por sua disposição espacial. Através do tempo se observa a migração dos eventos de Oeste a Leste, especialmente durante o Mesozóico-Cenozóico (Palacios *et al*., 1995).

Os estudos petroquímicos e mineralógicos apontam que a série magmática, que caracteriza a parte peruana da Cordilheira dos Andes, é sobretudo de tendência cálcio-alcalina, ainda que existam alguns corpos plutônicos de natureza alcalina (Palacios *et al*., 1995).

As rochas plutônicas estão bem representadas por batólitos que se encontram tanto na Cordilheira Ocidental como na Oriental. Os batólitos mais destacados são o de São Nicolás e Camaná na costa Sul e os plutons de idade Permo-Triássica de Aricoma, Limbani, Coasa e San Ramón na Cordilheira Oriental.

O Batólito da Costa de idade Cretáceo - Terciário (Fig. 2.2, Fig. 2.3) e o da Cordilheira Blanca (Mioceno) foram localizados na margem ocidental dos Andes, se destacando por suas notáveis dimensões.

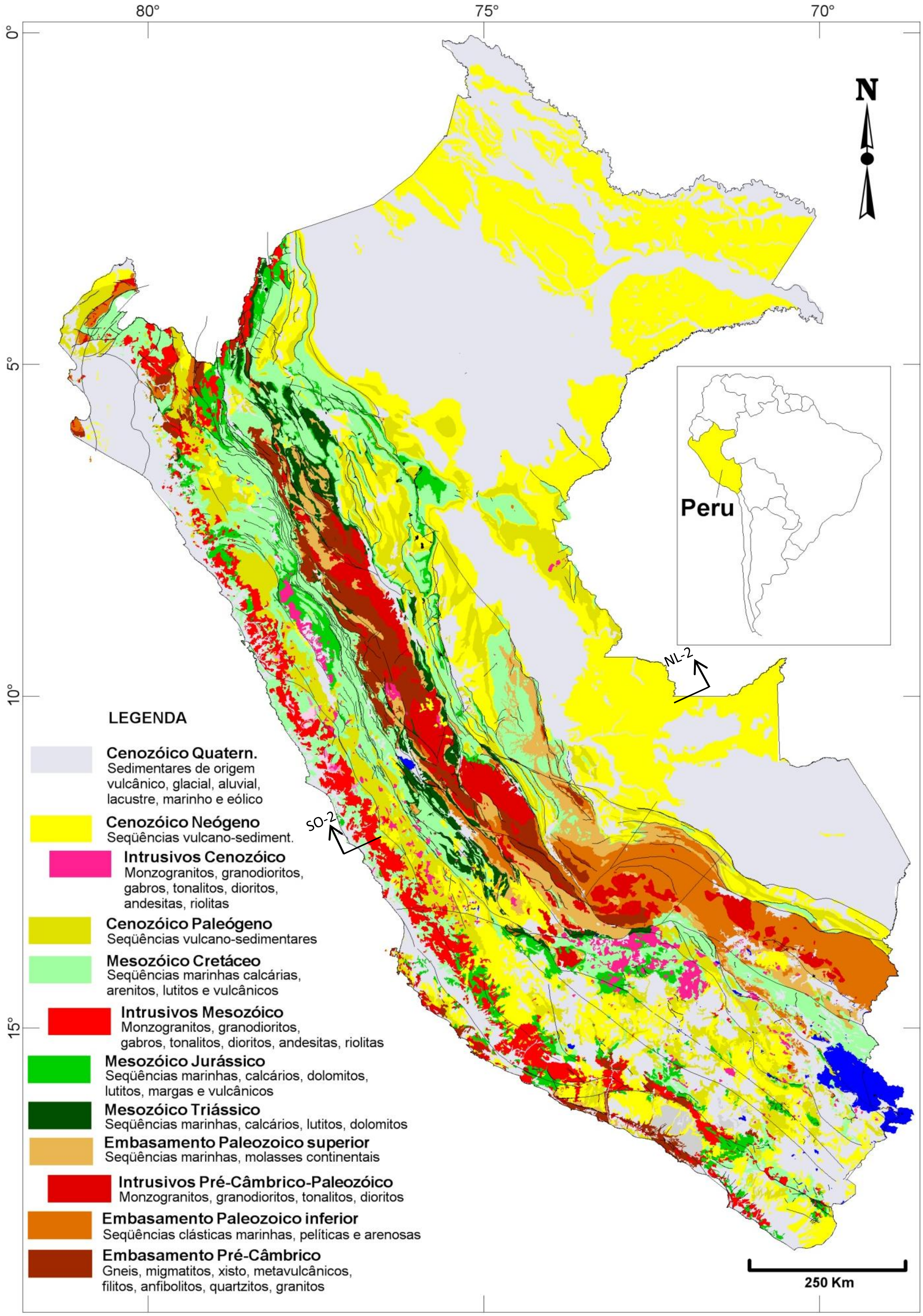

Figura 2.2. *Mapa geológico simplificado do Peru (INGEMMET, 2013).*

As rochas vulcânicas mais antigas se encontram distribuídas no flanco ocidental dos Andes. São conhecidos como vulcânicas Chocolate e Oyotún de idade Jurássica, na costa Sul e Norte respectivamente. As unidades que caracterizam os episódios vulcânicos do Cretáceo são o Grupo Casma, que se encontra ao Norte de Lima, e o Grupo Toquepala, que se encontra amplamente distribuído nos estados de Arequipa, Moquegua e Tacna. O vulcanismo Cenozóico está caracterizado pelos Grupos Calipuy, Tacaza e as formações Huaylillas, Sencca e equivalentes; tendo estas unidades continuidade de afloramentos no SO do Peru (Palacios *et al*., 1995). O vulcanismo Barroso é responsável pela morfologia atual da cordilheira do Sudoeste do Peru, caracterizado pelas estruturas vulcânicas do Misti, Ubinas, Chachani, Tutupaca, Yucamane, etc. (faixa de cones vulcânicos, Fig. 2.1b).

Na Cordilheira Oriental (Fig. 2.1b) se encontram rochas vulcânicas associadas ao vulcanismo Permo-Triássico (Grupo Mitu). Seus afloramentos foram observados desde o NE do Peru (Departamento de Amazonas), até o SE (Departamento de Puno) (Palacios et al., 1995).

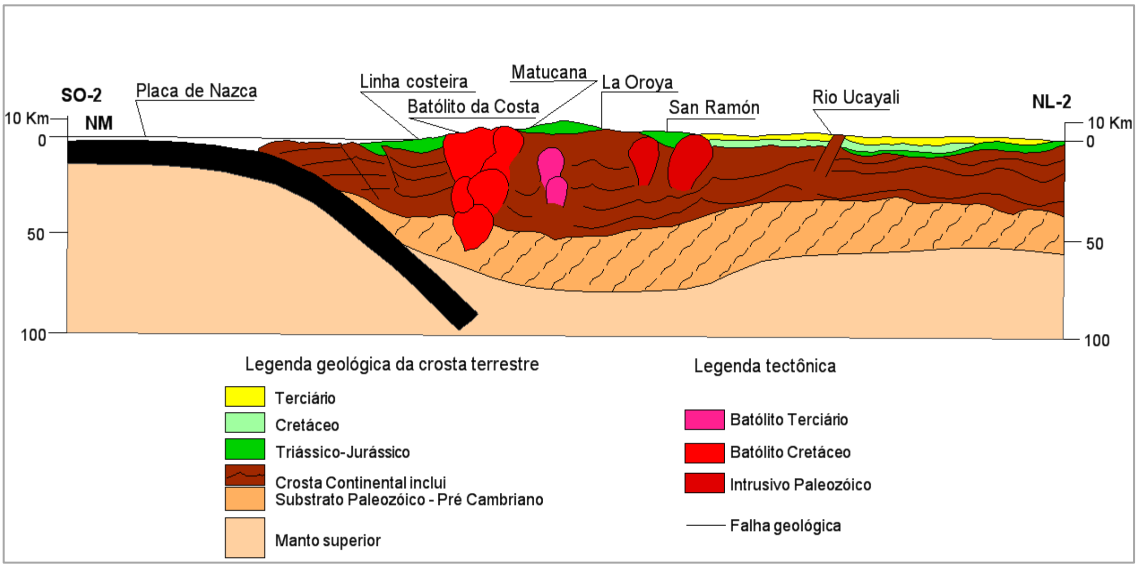

Figura 2.3. *Seção estrutural esquemática SO-2 – NL-2 da Fig. 2.2 mostrando a crosta terrestre atual dos Andes centrais do Peru (Palacios et al., 1995).*

Na região subandina oriental (Fig. 2.1b), não foram determinados eventos magmáticos importantes. São conhecidos pequenos plutons de rochas intermediárias como o pluton dos Cerritos de Mora próximo à fronteira com o Brasil.

Na maioria dos depósitos metálicos peruanos, as soluções mineralizadoras provêm de magmatismo intrusivo, hipabisal e efusivo, encontrando-se depósitos disseminados e veios, formados principalmente por processos hidrotermais, cujos tipos de minérios e volumes dependem das estruturas, magmas e a natureza da rocha hospedeira, que lhes deram origem. Os sistemas porfiríticos, tanto de cobre como de ouro, aparecem associados ao ciclo Andino e são, sem dúvida, os principais tipos de depósitos presentes nos Andes peruanos.

2.1.MARCO TECTONOMAGMÁTICO

Desde o Jurásico e Cretáceo inferior é provável que a Cordilheira da Costa, na área de Yanac, se encontrava sob um quadro tectônico de extensão e transtensão de subdução de ângulo alto (Fig. 2.4a) como aconteceu mais no sul do Peru e norte do Chile (Uyeda e Kanamori, 1979 em Camus, 2003; Sillitoe e Perelló, 2005), no âmbito de um magmatismo de composição basáltica-intermediária durante o Mesozóico médio – superior (Sillitoe, 2003; Sillitoe e Perelló, 2005). Isto poderia estar evidenciado, em parte, pela falha NW dextral “Treinta Libras” (Injoque, 2002) onde este período é caracterizado por uma mineralização do tipo Fe-Cu-Au (IOCG) ao longo da Cordilheira da Costa, alojados principalmente em falhas e camadas nos depósitos desta idade, tais como: Marcona, Mina Justa, Monterrosa e Hierro Acarí.

Trabalhos de Benavides-Cáceres (1999) descrevem um evento de deformação com esforços de contração denominado fase “mochica” (Tabela 2.1), que teria iniciado no Albiano Superior (108-95 Ma) e que se estendeu até o início do Campaniano (80 Ma), antes do alojamento do Batólito da Costa do Peru (Benavides-Cáceres, 1999). Esta fase representa possivelmente o ponto de partida da deformação de contração do Cretáceo. A partir deste período as características da mineralização mudam, predominando pequenos depósitos do tipo pórfiro de cobre e preenchimento de fraturas de ouro e cobre (Fig. 2.4b). Isto é evidenciado com o alinhamento de pórfiros de cobre na faixa do Cretáceo superior do Flanco Pacífico da Cordilheira Ocidental.

A origem do pórfiro de cobre Yanac é considerada como estando relacionada com a mudança do ângulo de subdução, que ocorreu no início do Cretáceo superior, de um ângulo elevado para outro menos inclinado ou tipo chileno (Uyeda e Kanamori, 1979; em Camus 2003), que afetaria também o sul do Peru. Isto é demonstrado pelo magmatismo intenso dessa época, refletido no Batólito da Costa da mesma idade

(Pitcher *et al*., 1985). Esta mudança na subdução provocou modificação do ambiente tectônico de extensão para compressão (Camus, 2003), o que causou neste período o início de um engrossamento cortical, existente desde há 100 a 120 Ma (Clark *et al*., 1990) (Fig. 2.4 a, b, c).

No Peru, o evento foi seguido pela fase “Peruana” do Campaniano (84-79 Ma) e seus efeitos foram observados no sul do país, até a fronteira com o Chile (Benavides-Cáceres, 1999).

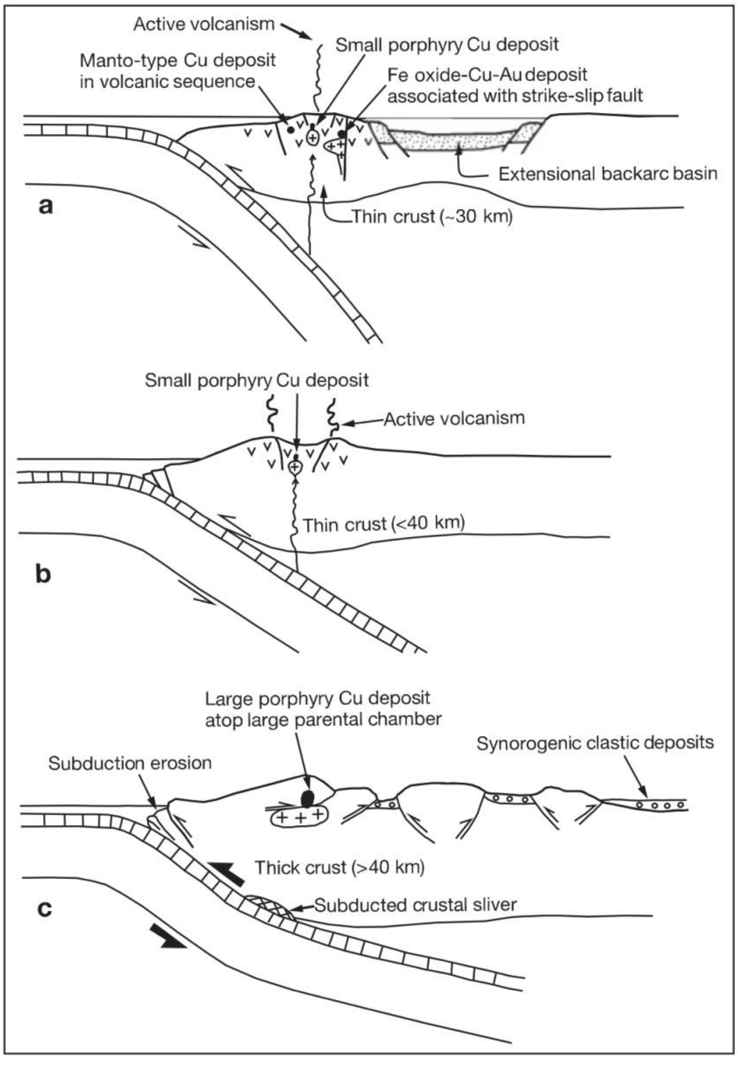

Figura 2.4. *Esquemas de seções tectonomagmáticas da margem central dos Andes do sul do Peru e norte do Chile. (a) Arco em extensão ou transtensão: Faixa do Jurássico-meio-Cretáceo inferior. (b) Arco magmático neutral a extensão meia: Faixa do Paleoceno-Eoceno-inferior. (c) Arco magmático de contração: Faixas Eoceno médio-inicio Oligoceno e Mioceno-inicio Plioceno. (Sillitoe e Perelló, 2005).*

O sul do Peru foi afetado por vários eventos de deformação que causaram rupturas na crosta terrestre e deixaram blocos crustais. Estas rupturas causaram falhas e estão representadas por sistemas regionais NW-SE (Fig. 2.5), denominados: Ica-Islay-Ilo, Nazca-Ocoña, Cincha-Lluta, Incapuquio, Condoroma-Cailloma, Cusco-Lagunillas-Mañazo, Urcos-Sicuani-Ayaviri e Abancay-Andahuaylas-Totos. Estes sistemas de falhas mudaram seus deslocamentos através do tempo geológico e facilitaram a colocaçao de magmas que deram origem à mineralização.

O controle estrutural regional em Yanac é dominado principalmente por falhas NW-SE que podem passar de 100 Km, e mais para o SE da área de estudo, as estruturas parecem ser mais uma prolongação do Sistema de Falhas Incapuquio (SFI) proveniente do sul do Peru (Fig. 2.5).

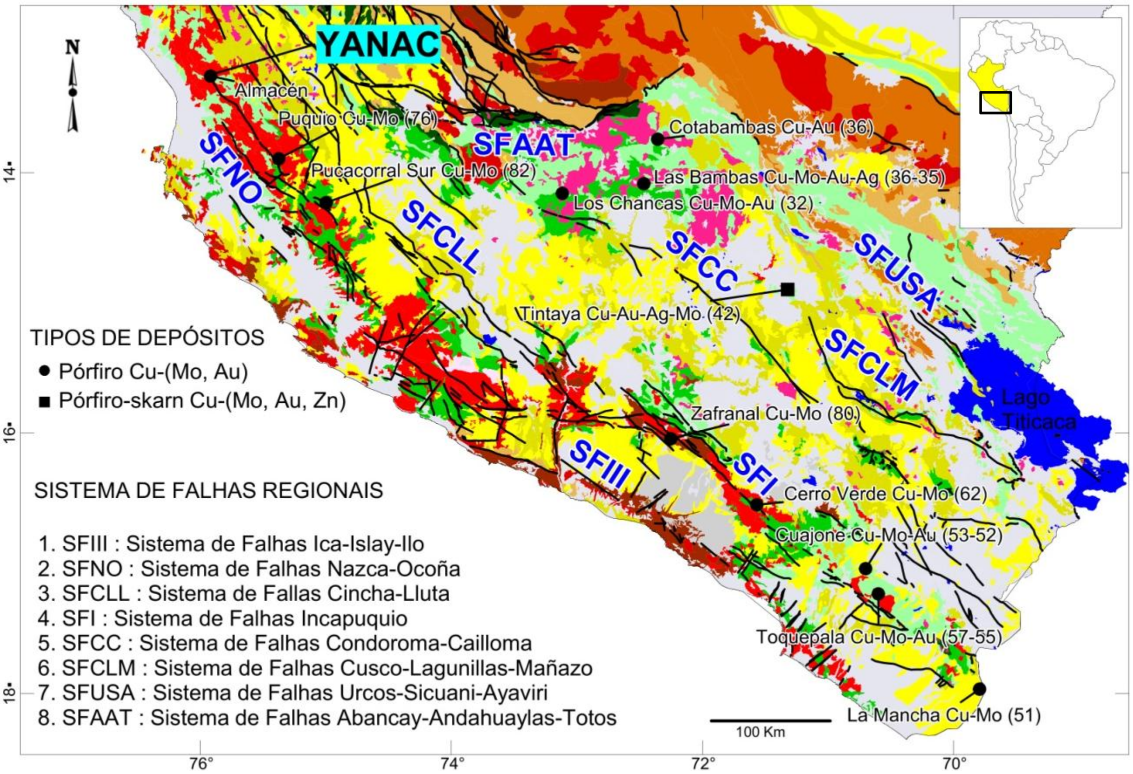

Figura 2. 5. *Mapa do sul do Peru mostrando a localização dos Sistemas de Falhas Regionais relacionados aos depósitos tipo pórfiro de Cu, INGEMMET, 2013.*

2.3. ÉPOCAS METALOGENÉTICAS

A partir da Cordilheira da Costa até o flanco da Cordilheira Oriental (Fig. 2.1a, 2.1b, Fig. 2.6), principalmente nos Andes Centrais do Continente sulamericano, são

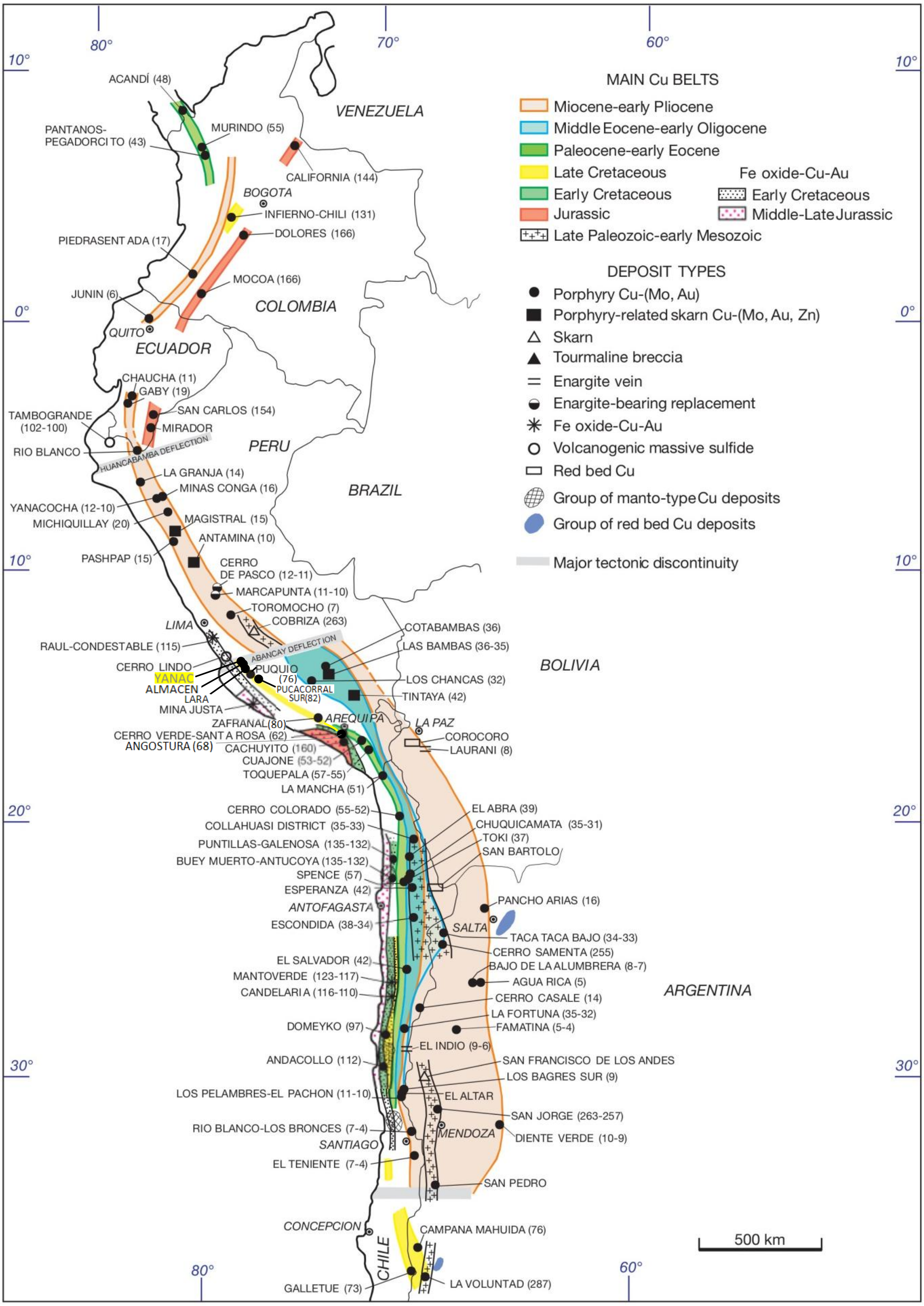

Figura 2. 6. *Faixas metalogénicas de cobre dos Andes mostrando o mapa do Peru e a localização dos pórfiros de provável idade cretácica, incluindo Puquio (76 Ma), Pucacorral Sur (82 Ma), e Angostura (68 Ma). Acosta et al., 2008 e depósitos de Cu (minas em produção), Sillitoe e Perello (2005).*

identificadas épocas metalogenéticas compreendendo idades que são mais jovens para o continente. Essa variação representa a migração sistemática dos arcos magmáticos até sua localização atual na Cordilheira Ocidental (Fig. 2.6).

A mineralização do prospecto Yanac está provavelmente relacionada espacialmente com a faixa metalogénica dos pórfiros de Cu do Cretáceo Superior conjuntamente com outros pórfiros de Cu-Mo que ocorrem no Batólito da Costa (Fig. 2.6).

A SE há um alinhamento com o prospecto Puquio, Pucacorral Sur, Zafranal e Angostura (Fig. 2.6). No prospecto Puquio, os resultados de três datações Ar^{40}/Ar^{39} no pórfiro asociado à mineralização principal do sistema forneceram valores de 77,48 ± 0,53 Ma para sericita hidrotermal, 75,34 ± 0,40 Ma para biotita primária e 76,56 ± 0,87 Ma para biotita hidrotermal (Rivera *et al*., 2007). Obteve-se idade de 82,2 ± 0.5 Ma para dacito porfirítico do prospecto Pucacorral Sur, por Ar^{40}/Ar^{39}em sericita (Silva *et al*., 2008). Os pórfiros do extremo SE da faixa Cretácea, como Angostura, possuem idade de 68 Ma (Acosta *et al*., 2008). No depósito Zafranal, quatro datações Ar^{40}/Ar^{39}, uma em rocha total da unidade vulcânica andesítica e três na biotita secundária das rochas intrusivas principais que controlam a mineralização de cobre, forneceram os seguintes valores: 79,98 ± 0,36 Ma para a rocha vulcânica andesítica, 82,41 ± 0,43 Ma para o Diorito Zafranal, 83,37 ± 0,54 e 81,16 ± 0,43 Ma para o microdiorito Zafranal (Rivera, F., 2012).

CAPÍTULO 3 – MÉTODOS ANALÍTICOS

A presente pesquisa envolveu obtenção de dados geológicos e laboratoriais para que os objetivos propostos fossem alcançados.

Nos períodos entre 11 e 20 de julho e de 13 a 17 de dezembro de 2012, foi realizado o trabalho de campo na área de Yanac na região de Ica, com a intenção de coletar amostras da zona alterada, inalterada e mineralizada, da rocha encaixante e da rocha porfirítica mineralizante e, ainda, visitar pontos importantes com presença de anomalias geoquímicas em Cu e Mo, feitas por amostragem e mapeamento da empresa Estrella Gold Perú S.A.C. em dezembro 2011.

As amostras de rocha foram preparadas para a confecção de lâminas delgadas polidas no Laboratório de Laminação do Instituto de Geociências da UnB – IG/UnB após a serragem apropriada das mesmas no referido laboratório.

O estudo petrográfico de 60 seções polidas de um total de 46 amostras de campo foi realizado no Laboratório de Microscopia do IG/UnB usando microscópio petrográfico. Este estudo permitiu a observação dos minerais, textura, relações de contato entre os grãos, tamanho dos grãos e alteração dos minerais, além de permitir o registro dos diversos tipos de associações mineralógicas de Cu e Mo. Nesta etapa foram tiradas fotografias ilustrativas das lâminas delgadas.

A obtenção de dados de química mineral foi feita na Microssonda Eletrônica Jeol JXA-8230 no IG / UnB. Padrões naturais e sintéticos foram usados para a calibração. As condições de operação foram 15kV e corrente de 20nA, com um tempo de contagem de 10s. A redução e tratamento de dados foram feitas usando planilhas do Excel.

Algumas análises de minerais de argila ou outros minerais em que havia dúvidas sobre sua identificação ou estrutura foram realizadas no Laboratório de raios X da Universidade de Brasília, com o difratômetro de raios X Rigaku-D/MAX – 2, modelo A/C, equipado com tubo de cobre e filtro de níquel, operando a 40 kV e 20 mÅ. A interpretação dos difratogramas foi feita com a ajuda do software MDI JADE 3.0, com banco de dados PC-PDF (Powder Diffraction File – PDF para PC - 1996) produzido pelo Centro Internacional para Dados de Difração – ICDD (ICDD, 1996).

As análises geoquímicas de elementos maiores e traços em rocha total foram realizadas pela AcmeLabs Ltd., seguindo as rotinas analíticas 4A e 4B. A primeira delas consistiu na determinação de elementos maiores e menores por meio de ICP-AES de 0,2 g de amostra moída e homogeneizada após fusão com metaborato/tetraborato de lítio e digestão em HNO_3 diluído. As perdas por ignição foram medidas por diferença em peso após queima a 1000ºC, enquanto as análises de carbono e enxofre totais foram feitas por meio da rotina 2A em forno Leco. Na rotina 4B, as concentrações dos ETR e elementos refratários foram determinadas com ICP-MS aplicando a mesma preparação usada na rotina 4A. Adicionalmente, uma fração separada de 0,5 g foi dissolvida em água régia e analisada por ICP-MS. Os resultados dos elementos maiores e menores foram reportados como porcentagens em peso dos óxidos com limites médios de detecção (LMD) de 0,01 % em peso (exceto para o Fe_2O_3, que teve limite de detecção (LD) de 0,04 % em peso). Todo o ferro nas amostras foi reportado como Fe_2O_3. O LD para as análises 2A Leco foi 0,02 % em peso. Para os elementos traços, os LD obtidos foram 0,01 ppm (Tb, Tm, Hg e Lu), 0,02 ppm (Pr, Eu e Ho), 0,03 ppm (Er), 0,05 ppm (Sm, Gd, Dy e Yb), 0,1 ppm (La, Ce, Cs, Hf, Nb, Rb, Ta, U, Y, Zr, Ag, Bi, Cd, Mo, Ni, Pb, Sb, Tl e Cu), 0,2 ppm (Th e Co), 0,3 ppm (Nd), 0,5 ppm (Ga, W, As, Au, Se e Sr), 20 ppm (Cr), 8 ppm (V) e 1 ppm (Ba, Sn, Be, Sc e Zn).

Na geocronologia de U-Pb, o método e arranjo dos equipamentos usados nas análises isotópicas foram baseados naqueles apresentados por Bühn *et al.* (2009). As análises foram realizadas no laboratório de geocronologia da Universidade de Brasília, usando espectrômetro de massa Thermo Finnigan Neptune Multicollector ICP-MS. A entrada da substância mineral no espectrômetro foi conseguida por meio de ablação com um laser de estado sólido New Wave 213 μm Nd-YAG. As condições de análise variaram segundo as características das amostras com o objetivo de otimizar os sinais isotópicos; o diâmetro do feixe variou entre 10 e 30 μm com uma energia entre 0.5 e 1.2 J/cm^2 e frequência de 10 Hz.

Grãos de zircão separados a mão e concentrados com ajuda de uma bateia a partir de amostras de rocha britada ou de saprólito foram colocados em tubos plásticos de 9 mm de diâmetro preenchidos com resina. Os grãos foram posteriormente polidos usando pasta de diamante de 3 e 1 μm de diâmetro e limpos com ultrassom em HNO_3 a 3% e água purificada. Posteriormente, imagens de catodoluminiscência (CL) foram adquiridas para ajudar a posicionar corretamente o feixe do laser de acordo com a estrutura interna dos minerais durante a fase de ablação.

O preparado com os grãos foi inserido numa câmara com um fluxo de He entre 0,35 e 0,45 l/min. A remoção do ^{204}Hg no fluxo de He foi conseguida passando o gás através de tubos de vidro contendo partículas de quartzo cobertas com ouro; isto foi feito para minimizar a interferência isobárica com o ^{204}Pb e permitir a aplicação das correções do Pb comum.

Depois de passar no plasma de argônio, o material vaporizado foi transportado até a zona do detector que consistiu em seis contadores de íons multicanal (MICs). Para a análise do padrão e as amostras, os sinais foram coletados num bloco único com 40 ciclos de 1.049 s cada, começando as leituras dos sinais só após os últimos terem atingindo a máxima intensidade no início da ablação.

A técnica de *bracketing* entre padrões foi aplicada por meio das leituras da análise de um ponto no padrão e um "branco" a cada quatro ou oito pontos analisados nas amostras, com o objetivo de considerar o erro causado pela deriva instrumental do espectrômetro. O padrão internacional usado foi o zircão GJ-1, fornecido pelo ARC National Key Centre for Geochemical Evolution and Metallogeny of Continents (GEMOC) na Austrália. As suas idades de referência segundo Jackson *et al*. (2004) são: 608,6 ± 1,1 Ma (idade ^{207}Pb/^{206}Pb), 600,4 ± 1,8 Ma (idade ^{206}Pb/^{238}U) e 602,1 ± 3,0 Ma (idade ^{207}Pb/^{235}U).

A redução dos dados foi conseguida usando uma planilha elaborada no mesmo laboratório de geocronologia, avaliando as razões isotópicas dos 40 ciclos com um critério de rejeição baseado num nível de confiança 1σ e 2σ. As razões isotópicas corrigidas junto com as suas idades calculadas associadas foram plotadas usando a rotina ISOPLOT 3.71 (Ludwig, 2009).

Zircões com idades U-Pb concordantes (± 5%) foram selecionados para determinação isotópica de Lu-Hf, cujas análises foram executadas no mesmo local ou na mesma fase onde foram obtidos os dados de U-Pb. A metodologia utilizada foi aquela apresentada por Matteini *et al*., (2010) e Chemale *et al*., (2011).

A microssonda a laser, modelo UP 213 (Nd:YAG) New Wave, utilizada para as análises por ablação em minerais pode emitir alta densidade de energia em vários tamanhos de crateras (4 μm - 110 μm). O gás hélio (He) é o responsável pelo transporte do material da ablação para o ICP com um fluxo de 0,35-0,45 l/min.

Durante as análises de Hf com laser foi utilizado uma taxa de repetição de 10 Hz. Dependendo do tipo de laser utilizado e parâmetros selecionados constituem-se de uma prática corrente valer-se de uma freqüência de 10 a 20 pulsos por segundo. Com o laser UP213 de Nd:YAG, a taxa definida acima revelou-se satisfatória em termos de eficiência e estabilidade dos sinais.

De acordo com as quantidades de Hf dos padrões GJ-1, uma potência de 60% do laser mostrou-se adequada, de modo a fornecer uma densidade de energia de 5-6 J/cm2.

Os dados foram processados em planilhas Excel específicas para Lu-Hf a fim de calcular a idade modelo T_{DM} e o parâmetro εHf do ponto analisado baseadas na idade U-Pb previamente determinada no mesmo grão.

Análises de Sm-Nd e Rb-Sr foram realizadas em 13 amostras de rocha total no Laboratório de Geocronologia da UnB. As análises Sm-Nd foram feitas segundo o método descrito por Gioia & Pimentel (2000). Entre 70 e 100 mg de pó de amostra foram misturados com uma solução troçadora mista (spike) de ^{149}Sm-^{150}Nd e dissolvidos em cápsulas Savillex. A extração dos elementos lantanídeos foi feita através de técnicas convencionais de troca iônica em colunas de quartzo, usando resina BIO-RAD AG-50W-X8. As extrações de Sm e Nd foram realizadas em colunas de teflon empacotadas com resina LN-Spec (resina líquida HDEHP-ácido di-ethylhexil fosfórico impregnada em pó de teflon). As frações de Sr, Sm e Nd foram depositadas em arranjos duplos de filamentos de rênio. As razões isotópicas foram determinadas em espectrômetros de massa multi-coletor Finnigan MAT 262 em modo estático. As incertezas para ^{87}Sr/^{86}Sr são menores do que 0,01% (2σ) e para as razões ^{147}Sm/^{144}Nd e ^{143}Nd/^{144}Nd são melhores do que ±0.2% (2σ) e ±0,045% (2σ) respectivamente, baseadas em análises repetidas dos padrões BHVO-1 e BCR-1. As razões ^{143}Nd/^{144}Nd são normalizadas para o valor de ^{146}Nd/^{144}Nd de 0,7219 e a constante de desintegração (λ) usada é 6,54 x 10^{-12} a^{-1}. Os resultados foram processados utilizando-se o programa ISOPLOT (Ludwing, 2009). Os valores de T_{DM} foram calculados utilizando o modelo DePaolo(1981).

CAPÍTULO 4 – ARTIGO: GEOLOGY, GEOCHRONOLOGY, PETROLOGY AND METALLOGENY OF THE YANAC Cu-Mo PROSPECT, ICA, PERU

Carlos J. Collado[a], Márcia A. Moura[a]

[a]: Instituto de Geociências, Universidade de Brasilia (IG-UnB), Brazil.

ABSTRACT

The Yanac prospect is located at northeast of Chincha Alta, Ica Region, Peru, in the Arequipa segment of the coastal batholith of Peru and in the northwestern end of the late Cretaceous copper metallogenic belt of the Andes.

Three major granitic rocks, contemporaneous with gabbroic diorite-diorite-monzodiorite intermineral dykes and enclaves, were defined at Yanac prospect. The host rock of the Yanac porphyritic system, with U/Pb zircon age of 70.6 ± 1.0 Ma, is a medium to coarse-grained equigranular granodiorite from the Incahuasi superunit of the coastal batholith. With an inconsiderable difference age and error within of 1 Ma., both, the Incahuasi granodiorite is intruded by a fine to medium-grained porphyritic granodiorite, with U/Pb zircon age of 71.0 ± 1.0 Ma,and by a medium to coarse-grained porphyritic granodiorite-diorite, with U/Pb zircon age of 67.75 ± 0.80 Ma.

Finally, trachydacite and basaltic dykes cut the porphyry system. They are post-mineralization and could be related with the emplacement events of the coastal batholith.

The Incahuasi granodiorite, the porphyritic granodiorite and the porphyritic granodiorite-diorite have petrographic characteristics of oxidized magmas. Geochemically, the granitic rocks, the dykes and the enclaves that occur in the granites have calc-alkaline and metaluminous composition, similar to I-type magmas from

volcanic arcs. They have primary annite-phlogopite biotite, compatible with calc-alkaline orogenic suites, and magnesium-hornblende amphiboles. The basaltic dyke is geochemically similar to I-type magmas, while the trachydacitic dyke has S-type magma signature.

Values of εHf(T) from -0.28 to +6.65 and Hf T_{DM} from 460 to 740 Ma for the porphyritic granodiorite and porphyritic granodiorite-diorite, together with εNd(t) from -1.11 to 1.72, $^{87}Sr/^{86}Sr(i)$ between 0.70450 and 0.70472, and Nd T_{DM} values from 520 to 850 Ma. for the Incahuasi granodiorite, porphyritic granodiorite, porphyritic granodiorite-diorite, intrusive intermineral dykes, enclaves and basaltic dykes, suggest a subcontinental mantle derivation, with minor crustal component of recycled oceanic sediments or precambrian basement, and a similar evolution trend. They are considered as the source of magmas and of Cu-Mo metals. The trackydacite dyke has εNd(t) of -2.33, $^{87}Sr/^{86}Sr(i)$ of 0.70778 and T_{DM} of 850 Ma., coherent with derivation from the upper crust.

The granitic rocks underwent different types of hydrothermal alteration at Yanac. A less enriched Cu-Mo propylitic alteration is mostly restricted to lateral zones and is characterized by A1 subtype veinlets with quartz-chlorite-albite-carbonates-pyrite±chalcopyrite; A2, with pyrite-quartz±chalcopyrite±molybdenite; and A3, with K-feldspar-epidote-chlorite-pyrite±chalcopyrite assemblages. A more Cu-Mo enriched central phyllic alteration in the system is characterized by different subtypes of veinlets. First, by a weak phyllic alteration, with high stockwork intensity, represented by B1 subtype veinlets, composed of quartz-pyrite-chalcopyrite-molybdenite, and weak alteration halo of sericite-albite; B2, with quartz-sericite, and albite halo, and pyrite-molybdenite-chalcopyrite±K-feldspar suture; B3, with sericite-chlorite-quartz-pyrite±chalcopyrite; and B4, with quartz-pyrite with a very pronounced sericite halo reaching up to 2 cm thick; and second, by a strong phyllic alteration, represented by B5, with quartz-sericite-pyrite±albite veinlets, that completely destroy the original texture of the rock. The hydrothermal breccia may be characterized by a weak phyllic alteration by its similarity of alteration and mineralization assemblage in event B. The latest veins observed are dominated by local C1 veinlets, with laumontite-quartz-adularia association.

The porphyritic granodiorite-diorite is interpreted as the responsible for the generation of hydrothermal solutions and Cu and Mo enrichment, by its later emplacement, the spatial position of the hydrothermal breccia, moderate to pervasive stockwork structures and higher Cu and Mo values related to the phyllic alteration.

Subsequent supergenic process and erosion at Yanac define a thin oxidation-leached zone..

Based on the style of the mineralization, the host rock, the metals, the hydrothermal alteration and the metallic minerals, Yanac is interpreted as similar to porphyry Cu(-Mo) deposits. Considering the mineralization as having the minimum age of 67.75 ± 0.80 Ma, it is situated within the upper Cretaceous metallogenic copper belt of the Peruvian Andes.

Investigation in deeper parts of the prospect is encouraged, in order to verify the existence of high temperature hydrothermal assemblages and possible higher metal concentrations. Economic concentrations of Cu-Mo in the transition porphyry-epithermal at Yanac and nearby should also be considered. It is possible that as more deposits are studied along the metallogenetic late Cretaceous belt of the Central Andes, in southern Peru, other Cu-Mo±Au deposits with characteristics similar to Yanac are described.

Keywords: Peru, Yanac, porphyry, metalogenesis, copper, molybdenum, hydrothermal alteration, geochronology, petrology, geochemistry, radiogenic isotopes, Cretaceous.

4.1. INTRODUCTION

The Yanac prospect is located in the West side of the Western Cordillera of the Andes, approximately 180 Km southeastern of Lima-Peru (Figs. 4.2, 4.1). Yanac is possibly located in the late Cretaceous of the copper metallogenic belts of the Andes, which contains a NW-SE oriented group of Cu deposits located northweast of the city of Arequipa. Yanac is situated at the northwestern end of the belt; the other deposits include Almacen, Lara, Puquio, Pucacorral Sur, Zafranal, Angostura, as well as several small prospects (Sillitoe and Perello, 2005). Alteration and mineralization at Yanac, have asssociations of quartz-pyrite-chalcopyrite-molybdenite-sericite-chlorite in veinlets and disseminations, in an equigranular granodioritic rock with medium grained of the coastal batholith cut by porphyritic granodiorite-diorite intrusions. Previous fieldworks and first interpretations by Estrella Gold Peru S.A.C. (2011) of the Yanac prospect have led to think this data as evidences of a porphyry copper model.

Although arc plutonism and the change of the subduction angle, of a high angle in the Jurassic and Lower Cretaceous to anoher less inclined starting from the Upper Cretaceous has been shown to be coeval with mineralization for many Andean deposits (Sillitoe and Perello, 2005, and references therein) still major uncertainties regarding the type of associated magmas, their source, their spatial relationship with ore and alteration, and the nature of the underlying basement.

This paper investigates the possible type of deposit at Yanac and temporal relationships between its Cu (±Mo, Au) mineralization and the magmatic rocks of the area, the geology, petrology, spatial relationship with the copper metallogenic belts in southern Peru and the context to a genetic model subduction-related magma of the ore prospect, its alteration halo, and the possible sources and characteristics of the associated magmatism.

The time-constrained geologic model we propose is supported by a local map with a detailed study of the geology, alteration and mineralization, whole-rock geochemical data, U-Pb dating and Lu-Hf isotopes of zircon from magmatic rocks, as well as radiogenic isotopes of Rb-Sr and Sm-Nd in whole-rock. The conclusions of this study have implications for the better understanding of the geology, geochronology, petrology and metallogeny of the Yanac prospect and similar outcrops and deposits present in the Western Cordillera of southern Peru.

4.2. REGIONAL GEOLOGIC FRAMEWORK

The studied area forms part of the western Peruvian trough (Wilson, 1963; Cobbing, 1985; Jaillard *et al*., 1990), which is a mostly Cretaceous volcano-sedimentary belt that crops out along the central coast of Peru. Cobbing (1978) divided the western Peruvian trough into five basins, with the studied area being located in the Cañete basin (Fig. 4.1). This volcano-sedimentary sequence includes basaltic to rhyolitic lava, pyroclastic deposits, tuff, limestone, shale, sandstone, and locally, evaporite. The geology of the western Peruvian trough is complex, with strong lateral facies changes, and the literature dedicated to this sequence is fragmented and frequently contradictory (Wilson, 1963; Rivera *et al*., 1975; Guevara, 1980; Osterman *et al*., 1983; Atherton *et al*., 1985; Jaillard *et al*., 1990; Palacios *et al*., 1992; Salazar and Landa, 1993; Vela, 1997; Benavides-Cáceres, 1999). Many problems remain concerning the nomenclature of lithostratigraphic units (Vela, 1997) and their respective ages, which are essentially based on scarce macropaleontological data (mostly Rivera *et al*., 1975; Palacios *et al*., 1992; Salazar and Landa, 1993; and references therein) considered to correspond to the late Tithonian to Cenomanian interval (~147–93.5 Ma: Gradstein *et al*., 1995).

Apart from the U-Pb zircon ages presented in this dissertation, few absolute ages are available for the western Peruvian trough, all falling within the Late Cretaceous to Paleocene interval (U-Pb ages in Polliand *et al*., 2005; ^{40}Ar/^{39}Ar ages in Noble *et al*., in press, a and b). Farther inland, the western Peruvian trough is intruded by the Peruvian coastal batholith, which has an outcrop length of 1,600 km and is up to 65 km wide (Figs. 4.1 and 4.2; Pitcher *et al*., 1985; Mukasa, 1986a; Haederle and Atherton, 2002). The coastal batholith consists of a series of telescoped tabular intrusions that were emplaced at high crustal level through a combination of roof-lifting and cauldron subsidence (Pitcher *et al*., 1985). It is made up of composite and multiple calc-alkaline to tholeiitic intrusions, dominantly composed of tonalite and granodiorite and subdivided into units and superunits (Pitcher, 1985). The units have been defined as chemically and mineralogically homogeneous and coetaneous magmatic pulses, whereas superunits consist of groups of units with close spatial and temporal association, corresponding to consanguineous rock suites (Fig. 4.1, Atherton and

Sanderson, 1985). Although this “unit” and “superunit” nomenclature is not recognized by the American Geological Institute, it is used in this dissertation for consistency with previous works on the Peruvian coastal batholith (including the geologic map of Peru by the Instituto Geológico Minero y Metalúrgico, INGEMMET, 2013). Age relationships between the superunits show an eastward migration of the magmatic activity with time (Fig. 4.1, Pitcher, 1985; Mukasa, 1986a).

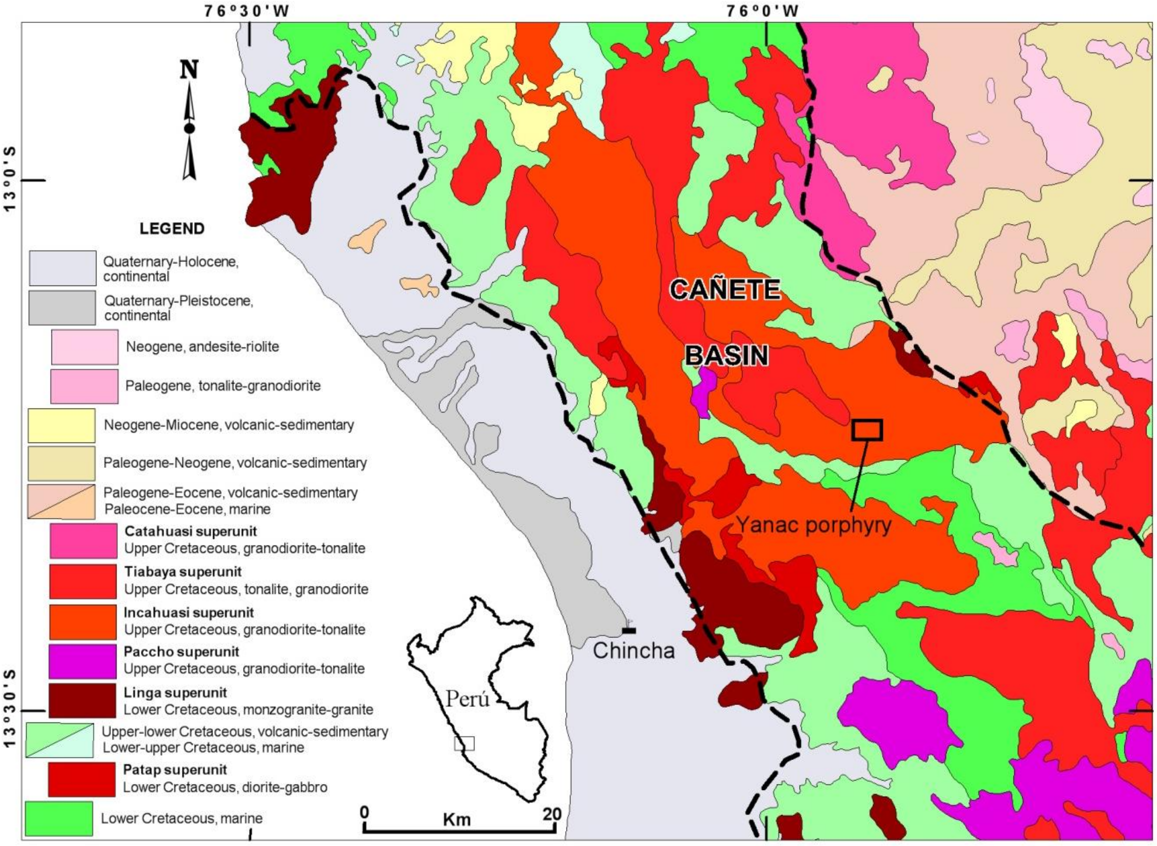

Figure 4.1. *Yanac regional map, INGEMMET, 2013.*

Based on the superunit assemblages, three main segments were defined along the batholith belt from north to south: the Lima segment has ages from ~106 to 37 Ma, the Arequipa segment, from ~106 to 80 Ma, and the Toquepala segment, from about 190 to 57 Ma (Fig. 4.2, Beckinsale *et al*., 1985; Moore and Agar, 1985; Mukasa and Tilton, 1985; Pitcher, 1985; Mukasa, 1986a). The studied area is located within the northern part of the Arequipa segment, close to the boundary with the Lima segment, in the Incahuasi super-unit (Figs. 4.2, 4.1). Common to these two segments, a tholeiitic affinity, on the Patap superunit and the Casma Group (western Peruvian trough: Albian to Cenomanian age) north of Lima (Regan, 1985; Atherton and Webb, 1989 in De

Haller *et al*., 2006) and a recently studied felsic magmatic body in the Raúl Condestable superunit represents oldest plutonic activity described around the area (De Haller *et al*., 2006) but they are not the scope of this dissertation.

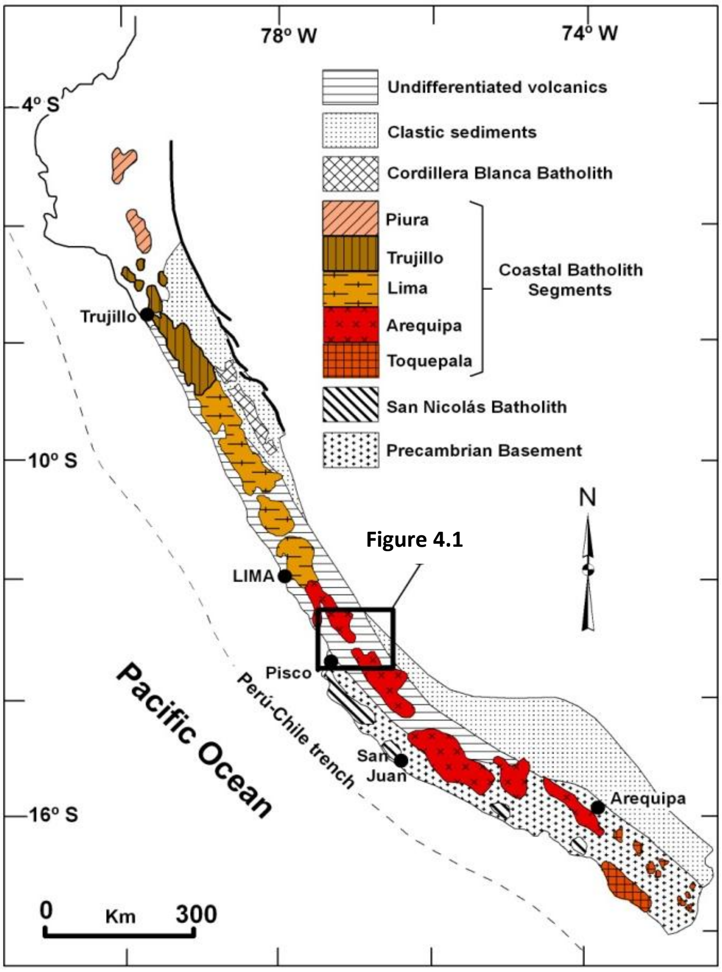

Figure 4.2. *Lithotectonic elements in the Western Cordillera and segments of the coastal batholith of Peru, Mukasa, 1986.*

Eastward of the Cañete Basin, subaerial volcanic flows, agglomerates, breccias and tuffs of the Tertiary belong to Nasca Group and are the products of a later unaltered geologic event in relation to the intrusion-alteration of the Yanac prospect (Fig. 4.1).

4.3. METHODOLOGY

Previous fieldworks on a ~3 km^2 in the Yanac prospect area resulted in an unpublished geological map at a 1:10,000 scale.. In 2012, the area was visited to review obscure data and collect samples of the unaltered, altered and mineralized zones for laboratory analyses.

Obtained data of mineral chemistry was taken in the Electron Microprobe Jeol JXA-8230 at IG / UnB. Natural and synthetic standards were used for calibration. Operating conditions were 15kV and current of 20nA, with a counting time of 10s. The reduction and processing of data were done using Excel spreadsheets.

Nineteen samples were selected for chemical analyses. The analyses were carried out at AcmeLabs Ltd., following 4A and 4B routines. The former involved ICP-AES analysis of major and minor elements after lithium metaborate/tetraborate fusion and dilute HNO_3 digestion. In routine 4B, trace elements were analized by ICP-MS following the same preparation as in 4A and digestion in aqua regia of an additional separate split.

Three samples were separated for geochronological determinations by U-Pb and two of these by Lu-Hf methods in zircon grains. The methodology and equipment set-up used for U-Pb geochronology closely followed those presented by Bühn et al. (2009) to whom the reader is referred for further details. Geochronological U-Pb analyses were carried out at the geochronology laboratory of University of Brasília, using a Thermo Finnigan Neptune multicollector inductively coupled plasma mass spectrometer. The input of mineral substance into the spectrometer was achieved by means of the laser ablation technique, using a New Wave 213μm Nd-YAG solid state laser. The sampling conditions of the latter varied according to the sample characteristics as to optimize isotope signals, with a beam diameter of 10-30 μm and a laser energy ranging from 0.5 to 1.2 J/cm2 at a frequency of 10 Hz. The samples were inserted into a He-flushed laser chamber maintaining the gas flux between 0.35 and 0.45 l/min. Removing of 204Hg from the He flux was attained by passing the gas through glass tubes containing gold-coated quartz particles intended to minimize the isobaric interference with 204Pb, thus allowing the application of common lead corrections where necessary. After passing through argon-sustained plasma, the ablated material was then conveyed to the detector arrangement which for this study consisted of six ion counters or multichannel ion counters (MICs). For standard and sample analysis, the signals were collected in a single block with 40 cycles of 1.049 s each, starting the reading of the signals after the latter had attained their maximum following the onset of ablation.

The standard-sample bracketing technique was applied by analyzing one standard point and one blank every four or eight sample points, thus accounting for instrumental drift. The international standard used here was the GJ-1 zircon, provided by the ARC National Key Centre for Geochemical Evolution and Metallogeny of Continents (GEMOC), Australia. Its reference ages after Jackson et al. (2004) are: ^{207}Pb/^{206}Pb age = 608.6 ± 1.1 Ma, ^{206}Pb/^{238}U age = 600.4 ± 1.8 Ma, ^{207}Pb/^{235}U age = 602.1 ± 3.0 Ma. Data reduction was achieved using a spreadsheet set up at the geochronology laboratory of University of Brasília; this spreadsheet allows evaluating the isotope ratios of the 40 cycles on a 2σ rejection basis. The corrected ratios and associated calculated ages were then displayed using Isoplot 3 (Ludwig, 2009).

Zircons with concordant U-Pb ages (± 5%) were selected for isotopic determination of Lu-Hf, whose analyses were performed at the same location or at the same stage where the U-Pb data were obtained. The methodology used was that presented by Matteini *et al*. (2010) and Chemale *et al*. (2011).

The laser microprobe, model UP 213 (Nd: YAG) New Wave, used for analyses in minerals can emit high energy density in various sizes of craters (4 mm - 110 mM). Helium (He) is responsible for transporting the material ablation for ICP with a flow rate of 0.35-0.45 l/min.

During the analysis of Hf with laser a repetition rate of 10 Hz was used. Depending on the type of laser used and selected parameters, it constitutes a current practice to has a frequency from 10 to 20 pulses per second. With the laser UP213 Nd: YAG, the rate defined above proved to be satisfactory in terms of efficiency and stability of the signals.

According to the amount of Hf of the patterns of GJ-1, a power of 60% of the laser was adequate, to provide an energy density of 5-6 J/cm2.

Data were processed in specific Excel spreadsheets to Lu-Hf in order to calculate the TDM model age and the εHf parameter of the analyzed point based in the U-Pb age previously determined in the same grain.

Thirteen samples were analyzed for Sm, Nd and Sr isotopesat the Geochronology Laboratory of University of Brasília. The analytical procedures applied in this study for measuring the ^{147}Sm/^{144}Nd and ^{143}Nd/^{144}Nd isotope ratios were the same as those described by Gioia & Pimentel (2000). Between 70 and 100 mg of sample powder were mixed with a mixed tracer solution (spike) of ^{149}Sm-^{150}Nd and dissolved in Savillex capsules. The extraction of lanthanide elements was made by conventional techniques of ion-exchange in columns of quartz, using resin Bio-Rad AG-50W-X8. The extraction of Sm and Nd were performed on columns of teflon packed with LN-Spec resin (HDEHP liquid resin-di-ethylhexil phosphoric acid impregnated in powder of Teflon). The fractions of Sr, Nd and Sm were deposited on double rhenium filament arrangements. The isotope ratios were determined in mass spectrometers multi-collector Finnigan MAT 262. Uncertainties for $^{87}Sr/^{86}Sr$ are smaller than 0.01% (2σ) and for reasons $^{147}Sm/^{144}Nd$ and $^{143}Nd/^{144}Nd$ are better than ± 0.2% (1σ) and ± 0.005% (1σ) respectively, based on analysis of repeated patterns of BHVO and BCR-1-1. The $^{143}Nd/^{144}Nd$ ratios are normalized to $^{146}Nd/^{144}Nd$ value of 0.7219 and disintegration constant (λ) used is 6.54×10^{-12} a^{-1}. The results were processed using the ISOPLOT program (Ludwig, 2009). The values of TDM were calculated using the DePaolo (1981) model. Sm and Nd concentration were calaculated by isotopic dilution, whereas Rb and Sr contents were taken from ICP-MS analyses.

4.4. LOCAL GEOLOGY

In the study-area there are porphyritic intrusions with granodiorite-diorite facies, intermineral dykes, hydrothermal breccias, and later basaltic and trachydacite dykes.

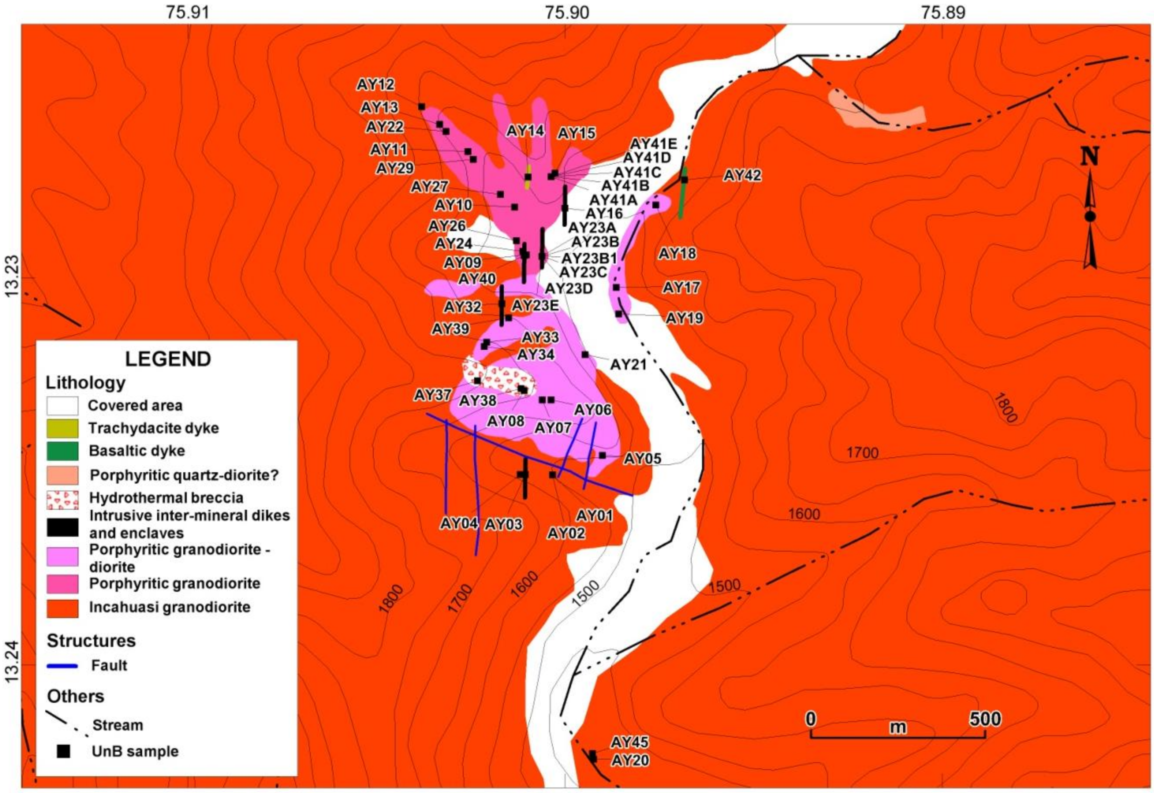

Figure 4.3. *Lithologic local map of Yanac, modified from Estrella Gold Peru (2011), with location of the studied samples.*

These rocks outcrop in a 1 x 1 km area cutting mainly the coastal batholith rocks (Fig. 4.3).

The Incahuasi granodiorite (IG) regional intrusive belongs to the Arequipa segment in the Incahuasi superunit of the coastal batholith of Peru (Figs. 4.3, 4.2). It is in contact and as wall rock of the porphyritic and mineralized rock (Fig. 4.4: D) and, together with the tonalite-granodiorite Tiabaya superunit, comprieses the outcrops of the coastal batholith around the study area (Figs. 4.1, 4.3). The Incahuasi granodiorite is light gray and commonly displays mafic dykes and enclaves (Fig. 4.3, table 4.1: sample AY-02, AY-03, AY-32, AY-41E, and Fig. 4.4: A and B), wich is indicative of magma mixing (Pitcher *et al*., 1985). It mainly presents an undeformed, holocrystalline, phaneritic, hypidiomorphic and equigranular medium to coarse-grained texture (Fig. 4.3, table 4.1: sample AY-01, AY-12, AY-20, AY-45 and Fig. 4.4: C, E). The essential minerals that constitute the rock are plagioclase, quartz, K-feldspar, biotite and hornblende. There are traces of zircon crystals (Fig. 4.4: E). Opaque minerals constitute around 1% of the modal composition and consist of anhedral grains of magnetite. Quartz constitutes a late phase of modal composition and is characterized by small anhedral grains grown interstitially between larger crystals of plagioclase, K-feldspar, amphibole and biotite minerals.

Locally, as observed in sample AY-04 (Fig. 4.3), the rock presents sienogranite to monzogranite modal composition according to Streckeisen (1976) classification, with plagioclase characterized as occurring in medium-grained crystals and polysynthetic twinning without zonation, with a very weak alteration to albite and epidote. Hornblende can be subhedral and often displays chloritization. As a result of this alteration, numerous small opaque grains (pyrite and probably ilmenite) accumulate around the chlorite. Biotite sometimes is skeletal and poikilitic, sorrounding smaller crystals of plagioclase and quartz. It displays variable chloritization and subsequent formation of aggregates of epidote and pyrite.

The porphyritic granodiorite (PG) is interpreted as the early intrusive in the system, on the basis of field observations. It is located in the northern area, in a stock of 400m wide and 500m long (Fig. 4.3) approximately. It is in contact with the Incahuasi granodiorite and in a referential contact zone at south with the porphyritic granodiorite-diorite, described below. It is characterized in many of the outcrops by a weak to moderate magnetism. The PG is light gray, and has a holocrystalline, phaneritic, hypidiomorphic, porphyritic texture with fine to medium-grained phenocrysts (Fig. 4.3, table 4.1: samples AY-13, AY-22, AY-11, AY-27 and Fig. 4.5: E). The essential minerals that constitute the rock occur as phenocrysts of plagioclase, quartz, K-feldspar, biotite and hornblende. Plagioclase crystals are subhedral to euhedral, zoned, with albite twinning. Subhedral to euhedral K-feldspar with Carlsbad twinning, together with crystals of hornblende, anhedral quartz and biotite are surrounded by a microcrystalline matrix, mainly of quartz and plagioclase. The accessory minerals are zircon and magnetite (Fig. 4.3, table 4.1: sample AY-22 and Fig. 4.5: F).

Considered the intermineral porphyritic intrusive in the system, the porphyritic granodiorite-diorite (PGD) constitutes mainly the host rock of the mineralization. It has an area of 500m wide and 500m long approximately (Fig. 4.3) at south of the porphyritic granodiorite and on the east side cutting the Incahuasi granodiorite of the coastal batholith (Fig. 4.3, Fig. 4.4: D). The porphyritic granodiorite-diorite follows a N-S direction, together with the PG, reflecting structural control in its emplacement (Fig. 4.3). The PGD is light gray and displays dykes and enclaves, with mafic composition (Fig. 4.3, table 4.1: sample AY-40, AY-23B, AY-23B-1, AY-16 and Fig. 4.5: A and B). The PGD is light gray, , with porphyritic texture (Fig. 4.3, table 4.1: sample AY-05, AY-07, AY-39, AY-21, AY-19, Fig. 4.5: C). It contains medium to coarse grained phenocrysts of plagioclase, quartz, K-feldspar, hornblende and biotite. Plagioclase, with up to 5 mm, is zoned and contains albite twinning. The phenocrysts of K-feldspar have Carlsbad twinning. The hornblende phenocrysts, with up to 1.5 mm, are subhedral to euhedral. Biotite phenocrysts, with up to 5 mm, are subhedral to euhedral, sometimes with skeletal and poikilitic texture, surrounding smaller crystals of plagioclase and quartz. Rounded quartz phenocrysts have up to 4mm. The matrix that involves these phenocrystals consists of microcrystalline aggregates mainly of quartz and plagioclase (Fig. 4.3, table 4.1: sample AY-05 and Fig. 4.5: D). Accessory minerals are zircon, titanite and magnetite.

Intrusive inter-mineral dykes and enclaves (IIDE) in the granodiorite Incahuasi as well as in the porphyritic granodiorite and the porphyritic granodiorite-diorite (Fig. 4.3, table 4.1: samples AY-02, AY-03, AY-16, AY-23B, AY-23B1, AY-32, AY-40, AY-41E, Fig. 4.4: A, B, Fig. 4.5: A, B, Fig. 4.6: A, B and Fig. 4.7: B) are composed of euhedral zoned plagioclase phenocrysts with albite twinning, euhedral biotite phenocrysts, K-feldspar with Carlsbad twinning, hornblende and apatite. Sometimes the plagioclase is skeletal and poikilitic, sorrounding smaller crystals of hornblende. Sample AY-02 (Fig. 4.3), of an enclave, is constituted of crystals of 0.25mm - 4 mm of hornblende, together with albite-twinned plagioclase from 0.25mm - 5 mm, with apatite inclusions. This sample contains anhedral clinopyroxene and Fe and Ti oxides (ilmenite or titanomagnetite).

In the Yanac prospect a body of siliceous Hydrothermal breccia (HB) with an irregular shape and a size reaching up to 300 m has been mapped. It outcrops southwest of the PGD (Fig. 4.3, table 4.1: samples AY-08, AY-37, AY-38 and Fig. 4.6: C). It is composed of subangular and subrounded fragments, mainly of the IG and PGD rocks. The diameter of the fragments can reach 0.25 m, which are included mainly in a siliceous matrix of hyaline quartz and crystallized quartz with sericite±chlorite aggregates, carbonates, pyrite-chalcopyrite-molybdenite, with subsequent formation of aggregates of epidote and pyrite (Fig. 4.3, table 4.1: samples AY-08, AY-37, AY-38 and Fig. 4.6: D).

Two types of volcanic dykes cut the granites. The first, a trachydacite dyke has greenish-gray color, mainly with plagioclase and K-feldspar within a microcrystalline volcanic matrix containing disseminated pyrite; and the second, a basaltic dyke has dark gray color and volcanic texture. They have a main N-S direction and subvertical dips between 75 º - 90º W with thicknesses from 0.50 to 4.0 m. The dykes cut the prospect and seem to be post-mineralization. They are probably related with the emplacement events of the coastal batholith (IG). They are well-preserved (Fig. 4.3, table 4.1: samples AY-14, AY-42 and Fig. 4.6: E and F). In the dykes that cut the PGD, green copper oxides and black copper oxides (amorphous minerals from an oxided zone of a supergene process), possibly copper pitch (hydrated silicate with Cu, Mn, Fe), copper-wad (oxide and hydroxide of Mn with Cu) or neotocite (hydrated silicate with Mn, Fe and Cu oxides) are common in fractures of the dykes. This does not appear to be caused by primary copper sulphides within the dykes but, rather, by a scavenging affect from the surrounding mineralized prospect they intrude.

A porphyritic quartz-diorite outcrops cutting the Incahuasi granodiorite, located to the northwest of the local geology map (Fig. 4.3). There is not available information in the literature about that rock.

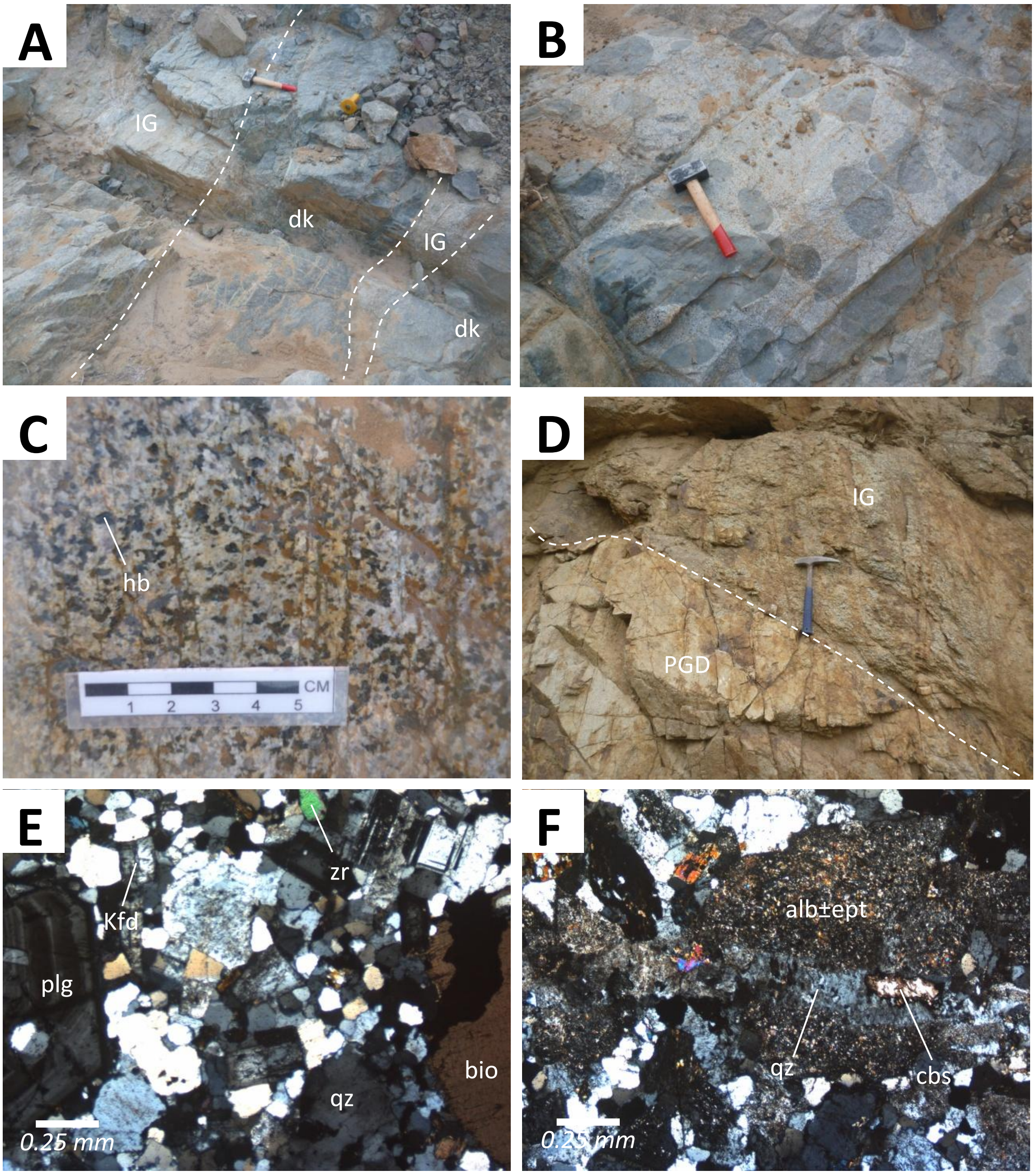

***Figure 4.4. A:** Porphyritic diorite dyke in the Incahuasi Granodiorite (IG),both cut by quartz-pyrite and chlorite-epidote veinlets (sample AY-03), **B:** Mafic enclaves in the IG cut by quartz-pyrite and chlorite-pyrite veinlets (sample AY-02), **C:** Medium to coarse-grained Incahuasi granodiorite, with undeformed phaneritic equigranular texture cut by quartz-pyrite veinlets, **D:** IG (upper right side) in contact with the porphyritic granodiorite-diorite (PGD)(lower left side) cut by stockworks filled mainly by sericite (around AY-17 sample), **E:** Crossed polar light showing essential minerals that constitute the IG (sample AY-01). Note the presence of zoned plagioclase and zircon, **F:** Weak quartz-carbonate alteration along thin veinlets in the IG and weak albite-epidote alteration from plagioclase (sample AY-01). Zr: zircon, qz: quartz, bio: biotite dk: dike, hb: hornblende, plg: plagioclase, kfd: potassic feldspar, alb: albite, ept: epidote, cbs: carbonates*

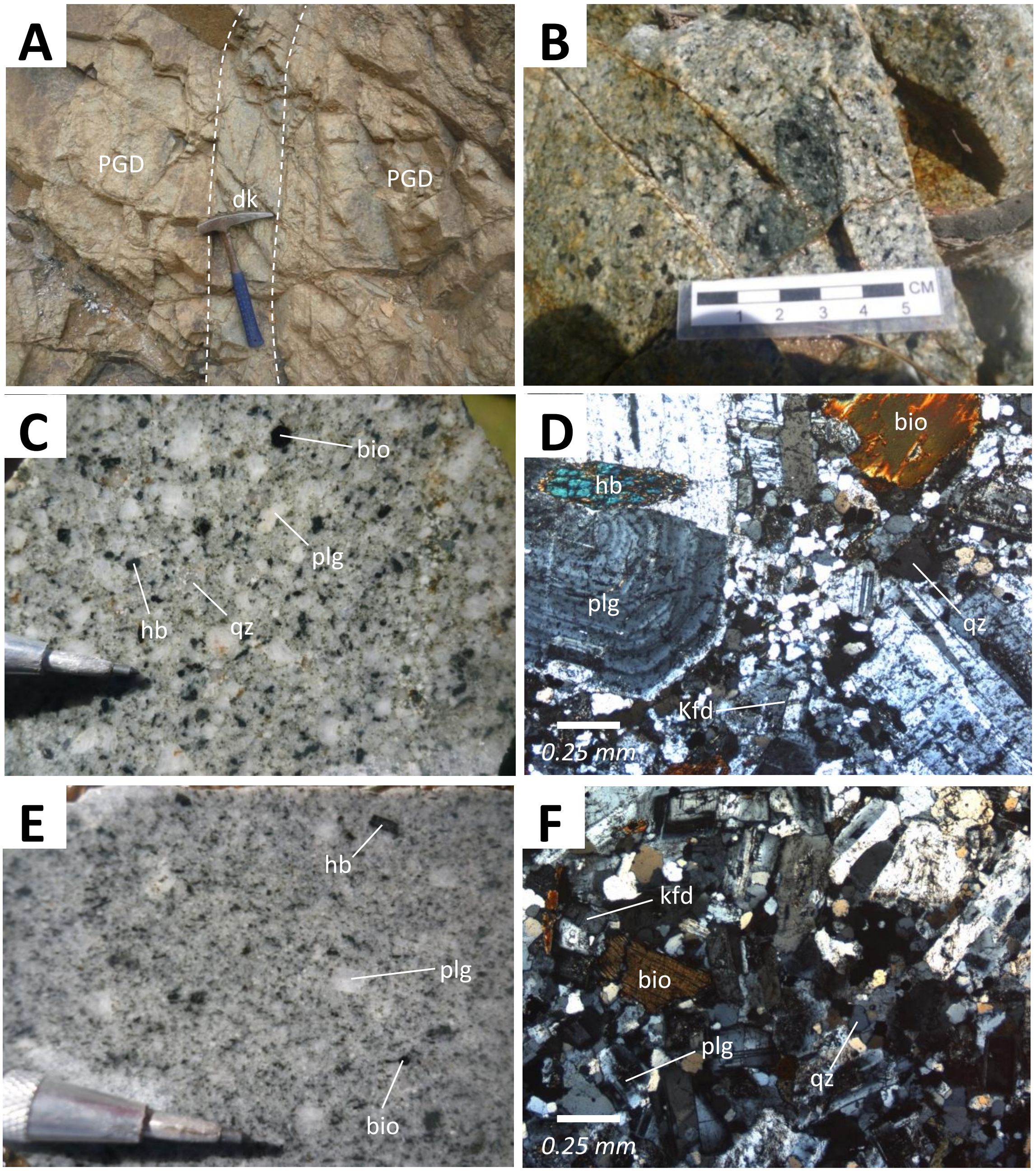

Figure 4.5. ***A:*** *Porphyritic gabbroic diorite dyke in the porphyritic granodiorite-diorite (PGD), cut by stockworks filled by sericite and chlorite (dyke sample: AY-40),* ***B:*** *Medium grained mafic enclave in the PGD cut by veinlets with weak quartz-sericite alteration (around sample AY-23B),* ***C:*** *Medium grained porphyritic diorite (PGD) in the southern stock cut by albite-epidote±pyrite veinlets (sample AY-05),* ***D:*** *Photomicrograph of medium to coarse-grained porphyritic diorite (PGD), undeformed, containing phenocrysts of plagioclase, quartz, K-feldspar, hornblende and biotite involved in a fine matrix of quartz and plagioclase (sample AY-05),* ***E:*** *Porphyritic macroscopic texture with a granodiorite composition in the northern porphyritic stock (PG, sample AY-22),* ***F:*** *Fine-grained porphyritic granodiorite containing phenocrysts of plagioclase, quartz, K-feldspar, hornblende and biotite involved in a fine matrix of quartz and plagioclase (PG, sample AY-22). Qz: quartz, bio: biotite, dk: dike, hb: hornblende, plg: plagioclase, kfd: potassic feldspar.*

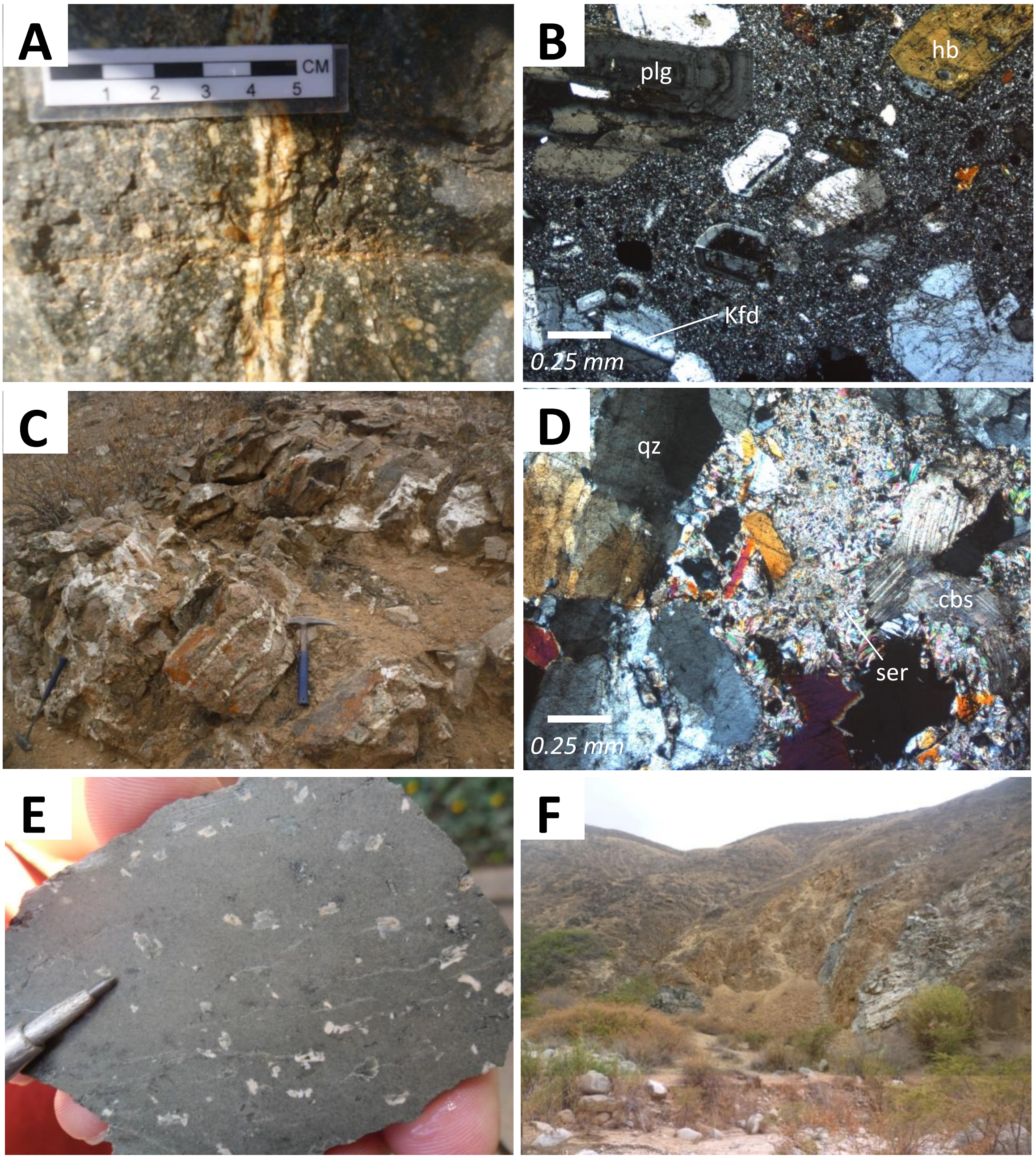

Figure 4.6. A: *Enclave of diorite composition with macroscopic porphyritic texture, cut by a quartz veinlet with suture of pyrite (sample AY-03),* ***B:*** *Enclave of diorite showing phenocrysts of euhedral plagioclase with polysynthetic twinning and zonation, K-feldespar with Carlsbad twinning and hornblende (sample AY-03),* ***C:*** *Outcrop of siliceous hydrothermal breccia conformed by subangular and subrounded fragments mainly of the PGD and IG rocks (around sample AY-08),* ***D:*** *Siliceous matrix of quartz with aggregates of sericite and subsequent formation of aggregates of carbonates (sample AY-38),* ***E:*** *Sample of light greenish gray dyke with plagioclase and K-feldspar phenocrysts in a microcrystalline matrix (trachydacite, sample AY-14),* ***F:*** *N-S dark gray dykes (basalt, sample AY-42, subvertical dip, between 75° - 90° to the west). Qz: quartz, hb: hornblende, plg: plagioclase, kfd: potassic feldspar, cbs: carbonates.*

4.5. ALTERATION AND MINERALIZATION

Hydrothermal alteration at Yanac is diverse. It occurs mainly as stockwork and disseminated. Stockwork structures are planar and continuous, their thickness varies from a few millimeters to a little more than 4 cm, with length exceeding 1 meter. They have an approximate density in the stockwork with intensity greater than 64 veinlets per meter. Primary sufides are represented by pyrite, chalcopyrite and molybdenite. Secondary covellite was observed. Processes of oxidation and leaching leave veinlets with cavities or filled with limonite and black and green copper oxides. The observed veinlets have been divided into three groups based on their mineralogy. Some of these groups contain several subtypes. Crosscutting relationships have enabled the construction of a timeline of the relative ages of veinlets.

The first hydrothermal event, named A, is mostly restricted to the lateral zones of the porphyritic granodiorite-diorite in contact with the Incahuasi granodiorite of the coastal batholith and in the stockwork zones with moderate intensity. It is characterized by veinlets of subtype A1: quartz-chlorite-albite-carbonates-pyrite±chalcopyrite (Fig. 4.3, table 4.1: samples AY-01, AY-04), A2: pyrite-quartz±chalcopyrite±molybdenite (Fig. 4.3, table 4.1: sample AY-11) and A3: K-feldspar-epidote-chlorite-pyrite±chalcopyrite (Fig. 4.3, table 4.1: samples AY-19, AY-33, AY-34). These veinlet types are illustrated in Fig. 4.7: C, D, E, F, and Fig. 4.8: A, B. They cut the IG, PG and PGD in the North and South of the prospect. The degree of alteration in this phase is very small, but it grades into a selective weak alteration phase containing sometimes chloritized amphibole, biotite with chloritized rims and secondary pyrite, epidote, chlorite and carbonates along fine veinlets (Fig. 4.3, table 4.1: sample AY-01 and Fig. 4.4: F). These veinlets are straight and do not have suture. In some places (sample AY-02; Fig. 4.3, table 4.1), the stockwork shows a preferential direction where there is a sheeting trend about 185/85 NE. The mineralization in the IG is not significative and occurs in veinlets, which have traces of pyrite-chalcopyrite.

The second hydrothermal phase, called B, is mostly present in PG and PGD area, with weak to moderate intensities (Fig. 4.3; Table 4.1: samples AY-09, AY-40, AY-24, AY-26, AY-27, AY-29 and from AY-23A to AY-23E). In some areas, a strong pervasive alteration occurs, which occasionally has obliterated the original texture of the rock (Fig. 4.3, table 4.1: AY-15, and from AY-41A to AY-41D). This event is characterized by different types of veinlets and seems to be also responsible for the formation of the hydrothermal breccia (Fig. 4.3, table 4.1: AY-06, AY-07, AY-08, AY-38, AY-37).

Subtype B1 veinlets are weakly sinuous (Fig. 4.3, table 4.1: sample AY-24) and present a mineralogical assemblage of quartz-pyrite-chalcopyrite-molybdenite with thin alteration halo of sericite-albite. B2 subtype veinlets are straight (Fig. 4.3; Table 4.1: samples AY-09 and AY-24), composed of quartz-sericite and albite halo with a pyrite-molybdenite-chalcopyrite±K-feldspar suture. B3 subtype veinlets are green and composed by sericite-chlorite-quartz-pyrite±chalcopyrite assemblage (Fig. 4.3; Table 4.1: AY-24, AY-26 and AY-27). B4 subtype veinlets, with up to 4 cm wide, are composed of quartz-pyrite with a very pronounced sericite halo reaching up to 2 cm thick (Fig. 4.3; Table 4.1: sample AY-29). Locally, irregular veinlets of subtype B5 completely destroy the original texture of the PG and are characterized by the presence of a quartz-sericite-pyrite±albite association (Fig. 4.3: Table 4.1: sample AY-41B). These veinlet types are shown in the Fig. 4.8: C, D, E, F, and Fig. 4.9.

The third hydrothermal alteration, named C, affects the PGD in the central and lateral zones of the Yanac prospect, in areas with high-intensity stockwork. It is present in small localized areas (Fig. 4.3; Table 4.1: samples AY-23C, AY-18). In the outcrop of this hydrothermal phase, the latest veins observed are dominated by distinguished veinlets of subtype C1: laumontite-quartz-adularia (annex 1), which cut the hydrothermal event B (Fig. 4.7: B). Their thickness reaches up to 20 cm (Fig. 4.7: B). The adularia is euhedral and occurs intergrown with subhedral quartz crystals (Fig. 4.7: A).

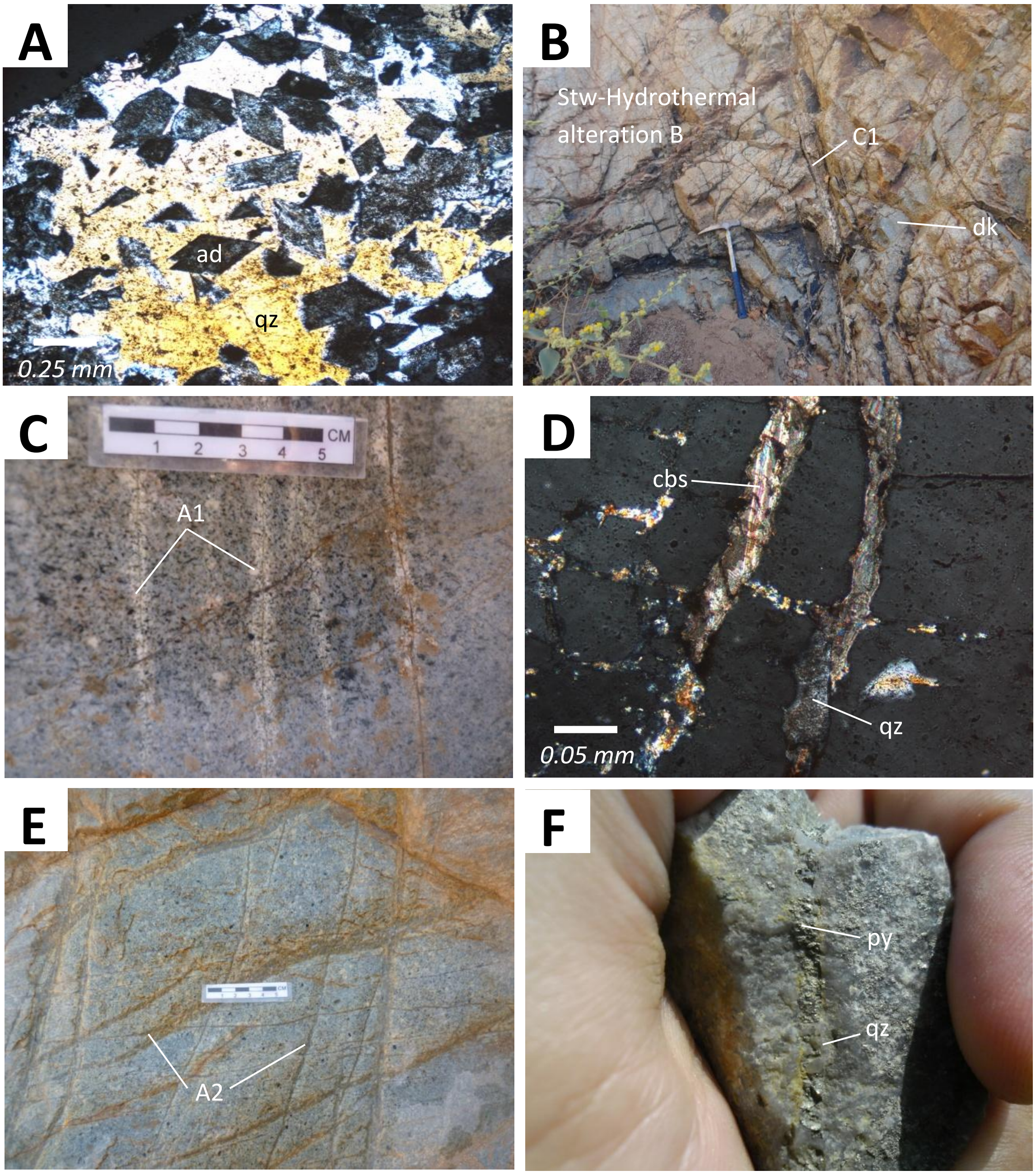

Figure 4.7. A: *Photomicrograph of C1 subtype veinlet, composed of quartz-adularia. Adularia is euhedral and occurs intergrown with subhedral quartz crystals (sample AY-18)* ***B:*** *Dykes of diorite composition in the PG, superimposed by B alteration event and C1 subtype veinlet (sample AY-23C),* ***C:*** *A1 subtype veinlet, composed of quartz-clorite-albite-carbonates-pyrite±chalcopyrite, cutting the IG (around of sample AY-01)* ***D:*** *Photomicrograph showing A1 subtype veinlet (around sample AY-01),* ***E:*** *A2 subtype veinlet, composed of pyrite-quartz±chalcopyrite±molybdenite, cutting the PG (sample AY-11),* ***F:*** *Sample of the PG cut by A2 subtype veinlet, composed of pyrite-quartz association (sample AY-11).*

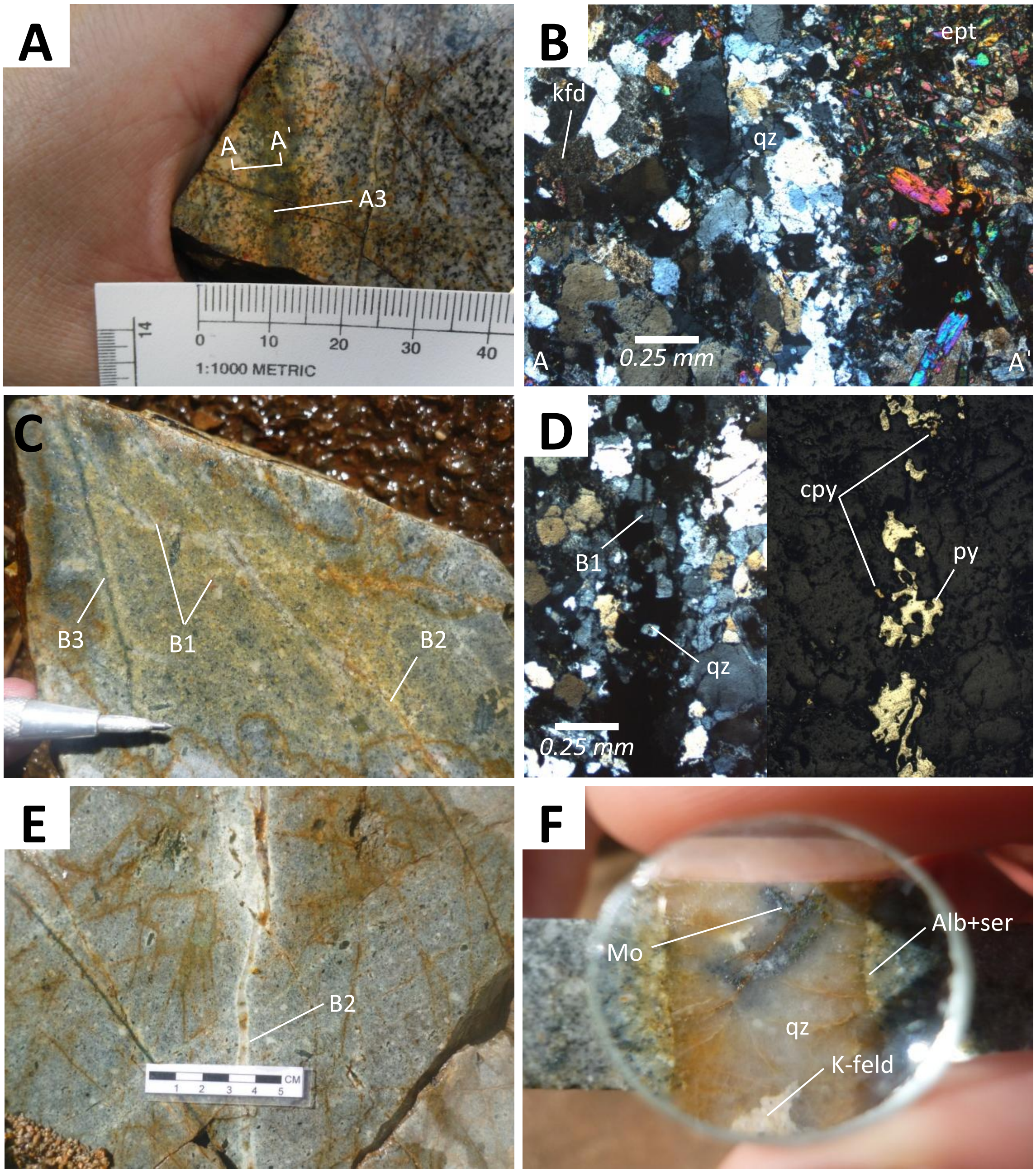

Figure 4.8. A: *A3 subtype veinlet, composed of K-feldespar-epidote-chlorite-pyrite±chalcopyrite (sample AY-19) cutting the PGD. Note the banded veinlet with epidote-quartz±chlorite in its central part and potassic feldspar halo,* ***B:*** *Photomicrograph of A3-type veinlet (sample AY-19) showing a section of veinlet from figure 4.8-A,* ***C:*** *B1 subtype veinlet cutting the PG, composed of quartz-pyrite-chalcopyrite-molybdenite, surrounded by a thin halo of sericite-albite (sample AY-24). B2 and B3 subtype veinlets cut these B1 subtype veinlets,* ***D:*** *Photomicrograph of B1 subtype veinlet in transmitted light (left) and reflected light (right), showing quartz-pyrite-chalcopyrite veinlets (sample AY-26),* ***E:*** *B2 subtype veinlets, composed of quartz-sericite and albite halo with pyrite-molybdenite-chalcopyrite±K-feldespar suture (sample AY-09, AY-24),* ***F:*** *B2 subtype veinlet, composed of quartz with thin sericite halo-albite-molybdenite±K-feldespar (sample AY-09).*

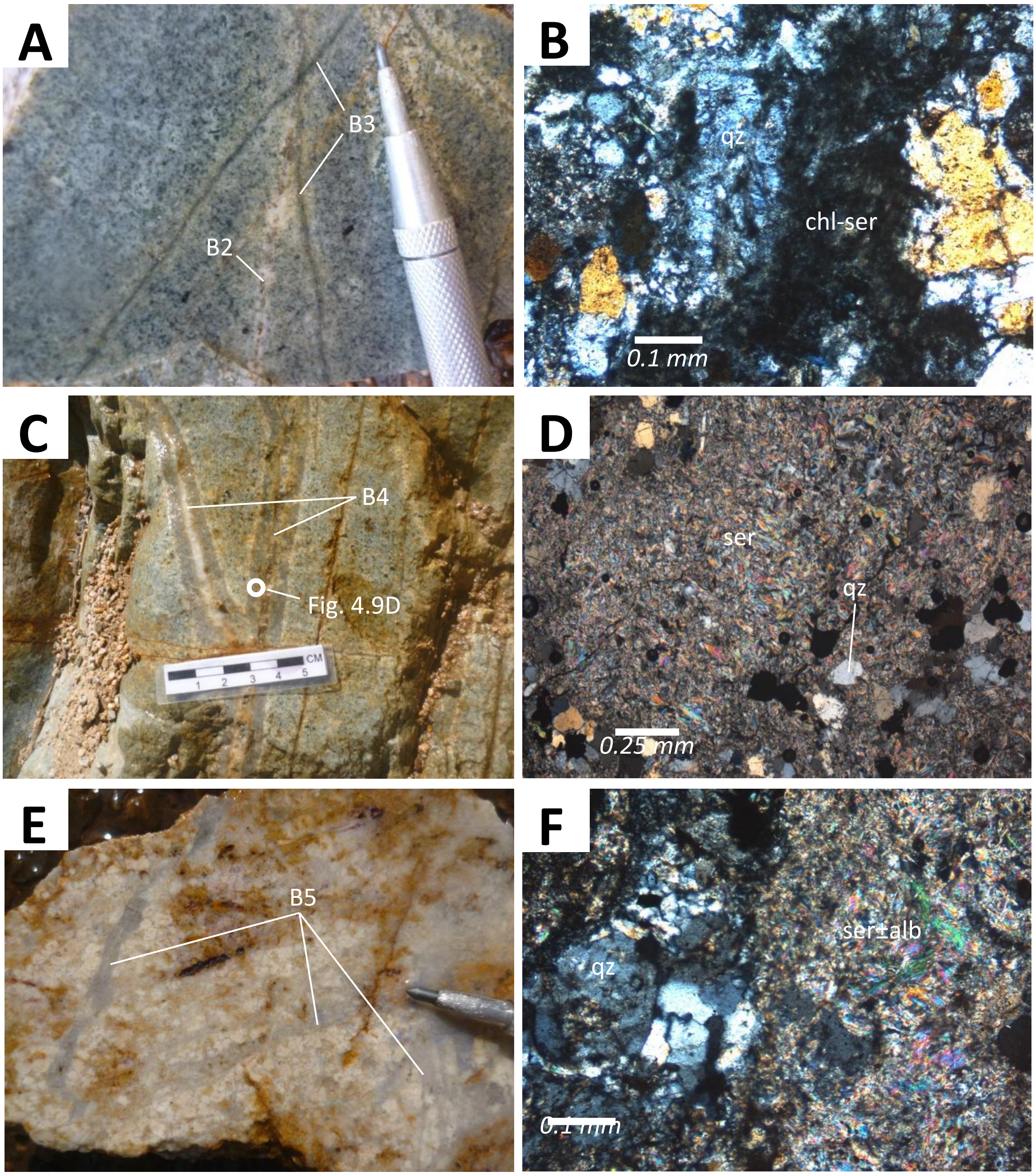

Figure 4.9. A: *B3 subtype veinlet, greenish, composed of sericite-chlorite-quartz-pyrite±chalcopyrite (AY-24, AY-26 and AY-27), and B2 subtype veinlet cutting the PG,* ***B:*** *Photomicrograph of B3 subtype veinlet (sample AY-24, AY-26 and AY-27),* ***C:*** *B4 subtype veinlet cutting the PG, of quartz-pyrite, surrounded of sericite-quartz halo reaching up to 2 cm with (sample AY-29),* ***D:*** *Photomicrograph of B4 subtype veinlet halo (sample AY-29), showing a zoom from figure 4.9-D,* ***E:*** *B5 subtype veinlets,composed of quartz-sericite-pyrite±albite. They are irregular and completely destroy the original texture of the rock (AY-41B),* ***F:*** *Photomicrograph of B5 subtype veinlet (sample AY-41B).*

Table 4.1. *Rock description, intensity and style of hydrothermal alteration and mineral association of the thesis research samples. The intensity of the alteration was made by estimating the volume occupied in the rock, on a scale from 1 (10%) to 10 (100%). Likewise, the style of occurrence was scored on a scale from 1 (for veinlets) to 10 (if it is penetrative). In this way a codification 7-1 means that 70% of the sample has a veined alteration. Ad: adularia, alb: albite, apt:apatite, BCuOx: black copper oxides, BKCuTiOx: black copper titanium oxides, cbs: carbonates, chl: chlorite, cpy: chalcopyrite, cv: covellite, dpr: diaspore, ept: epidote, GCuOx: Green copper oxides, hem: hematite, Kfd: potassic feldspar, lims: limonites, mo: molybdenum, ort: orthoclase, py: pyrite, qz: quartz, ser: sericite.*

Sample	Rock	Intensity and style of alteration	Mineralogic assemblage
Trachlydacite dyke (TD)			
AY-14	Trachlydacite	Unaltered	-
Basaltic dyke (BD)			
AY-42	Basaltic	Unaltered	-
Hydrothermal breccia (HB)			
AY-08	Hydrothermal breccia-Porphyritic diorite-granodiorite	7-6	qz-ser-chl±py±cpy±ept±GCuOx±lims
AY-37		5-3; 5-9	Qz-ser±GCuOx; Kfd
AY-38		7-6, 1-10	Qz-ser±py±cpy±GCuOx±BCuOx-cv±lims±dpr; chl-ept-clc
Intrusive inter-mineral dykes and enclaves (IIDE)			
AY-02	Mafic enclave	1-10	chl±py
AY-03	Porphyritic diorite dyke	1-1; 1-10	qz-py; chl-ept
AY-16	Porphyritic mafic dyke	1-2	qz±chl±alb±ser±py±cpy±GCuOx±lims
AY-23B	Porphyritic mafic dyke	1-1	BCuOx
AY-23B1	Porphyritic mafic dyke	1-1	qz±lims
AY-32	Porphyritic diorite dyke	Unaltered	-
AY-40	Porphyritic gabbroic diorite dyke	2-2	qz-py±cpy±ser±chl±ept±GCuOx±lims
AY-41E	Monzodiorite enclave	Unaltered	-
Porphyritic granodiorite-diorite (PGD)			
AY-05	Porphyritic diorite	1-10	chl-ept±py
AY-07	Porphyritic rock	2-1	qz±chl±alb±ser±ept±lims
AY-06	Porphyrytic rock - Hydrothermal breccia	6-4	qz-ser-chl±alb±py±cpy±mo±lims±GCuOx
AY-09		4-2	qz-ser-alb±Kfd±py-cpy-mo±cv±chl-ept±GCuOx±BCuOx±lims
AY-17		2-3	qz-ser-alb-chl-py±cpy±kfd-ept±dpr±BkCuTiOx±GCuOx
AY-18		1-8; 1-1	qz-ser-alb-py-±cpy±mo±ept±lims; K-kfd(ad)
AY-19	Porphyritic granodiorite	2-3; 2-2	qz-kfd(ort)-ept-py-±lims; qz-ser±alb±py±cpy±lims
AY-21	Porphyritic granodiorite	Unaltered	-
AY-23A		4-2	qz-ser-alb-py-cpy-mo±cv±chl-ept±GCuOx±BCuOx±lims
AY-24		5-2; 2-2	qz-ser-alb-py±cpy±mo±apt±chl-ept±dpr±cv±BCuOx±GCuOx; chl±ser±alb±py±cpy
AY-26		3-2; 2-2	qz-ser-alb-py-cpy±mo±cv±chl-ept±GCuOx±lims; chl±ser±alb±py±cpy
AY-33		3-2; 2-5	Kfd; ept±chl±py±cpy±GCuOx
AY-34		6-9; 1-10	Kfd; ept±chl±py±cpy±GCuOx
AY-39	Porphyritic diorite	1-1	ept
Porphyritic granodiorite (PG)			
AY-10		4-3	py±qz±cpy±mo±chl±ept±lims±cv±GCuOx
AY-11		3-3	py±qz±cpy±mo±chl±ept±lims±GCuOx
AY-13		1-9	chl-ept
AY-15		7-8	qz-ser±chl±ept-lims
AY-22	Porphyritic granodiorite	Unaltered	-
AY-23C		1-1	qz-kfd(ad)
AY-23D		4-2	qz-ser-alb-py-cpy-mo±cv±chl-ept±GCuOx±BCuOx±lims
AY-23E		5-3	qz-ser-alb-py-cpy-mo±cv±chl-ept±GCuOx±BCuOx±lims
AY-27		3-2; 1-2	qz-py-ser±cpy±chl±ept±lims
AY-29		4-3	qz-ser-py
AY-41A		7-8	qz±ser-lims
AY-41B		8-8	qz±ser-lims
AY-41C		7-8	qz-ser-lims (hem)
AY-41D		7-8	qz-ser±chl±ept-lims
Incahuasi granodiorite (IG)			
AY-01	Granodiorite	1-10; 1-1	chl±py; qz-chl-cbs±alb±ept
AY-04	Sienogranite-monzogranite?	1-1; 1-10	qz-ept-chl-py-cbs; chl-ept-py
AY-12		1-2	chl-ept
AY-20		1-10	chl
AY-45	Granodiorite	1-10	chl

4.6. SUPERGENIC PROCESS

The Yanac prospect has been weakly oxidized, partially leached and superimposed by a supergenic event, expressed by weak argilization of the rocks. It occurs irregularly and mainly in the porphyritic granodiorite and porphyritic granodiorite-diorite. Sulfides were oxidized to limonites (mainly jarosite), sericite and feldspars are altered to clays, and plagioclase and K-feldspar have been weakly argillizated, although retain their original habit.

An oxidation and leached alteration is characterized by occurrence of limonite, apparently jarosite (annex 1) > goethite > hematite. Locally, associated with coquimbite [$Fe_2(SO_4)_3 9H_2O$] and aluminocopiapite [$(Mg,Al)(Fe,Al)_4(SO_4)_6(OH)_2 20H_2O$] (annex 1), manganese oxides in disseminations, impregnations or veinlets type stock work, locally with weak appereance of gossan coexisting mainly with pyrite veinlets and weak presence of sulphides and green oxide ores of copper in areas with higher elevation. Present in the hydrthermal alteration A and to a lesser extent in the hydrothermal alteration B (Fig. 4.3, table 4.1: samples AY-11, AY-13, AY-22, around sample AY-41A and Fig. 4.10: A). Towards the NW margin of the hydrothermal system, there are areas with plenty oxidized pyrite veinlets mostly with a N-S unidirectional strike.

A mixed mineralized zone with oxide and supergenic enrichment occurs mainly between the porphyritic granodiorite-diorite and the porphyritic granodiorite, and the south area belonging to the Hydrothermal breccia. This area is characterized by dense stockwork and hydrothermal breccia, with primary sulfides minerals of pyrite, chalcopyrite, molybdenite, and secondary covellite around chalcopyrite (Fig. 4.10: B, C, E and F). Boxworks of pyrite were filled by limonite, diaspora, green copper oxides (possible malaquite) and black copper oxides (possibly copper pitch, copper-wad, neotocite) (Fig. 4.3, table 4.1: samples AY-09, AY-10, AY-23A, AY-23D, AY-23E, AY-24, AY-26, AY-38, Fig. 4.10: D, E and Fig. 4.11: A, B).

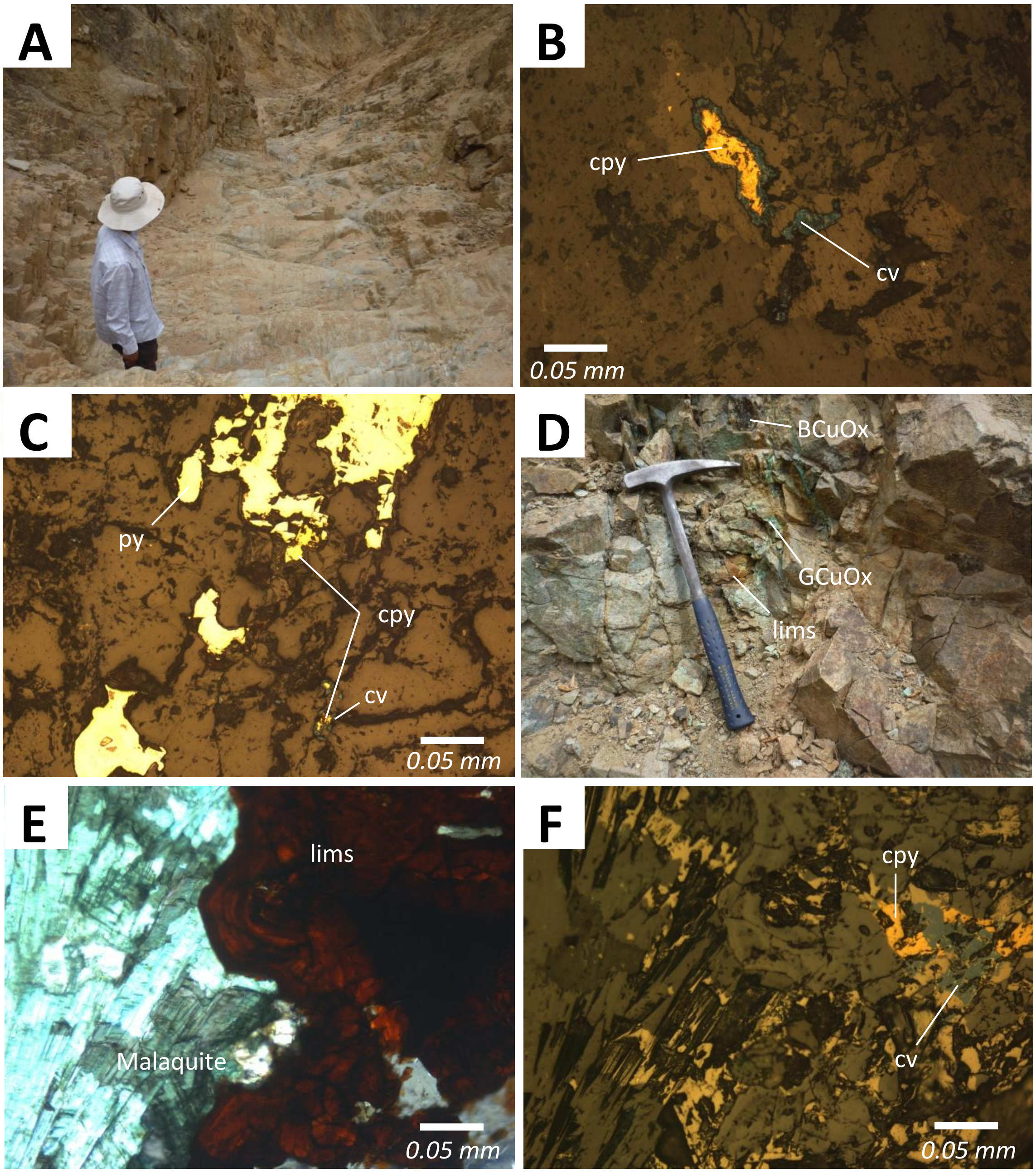

Figure 4.10. A: *Stockwork veinlet type, locally with weak appearance of gossan mainly coexisting with pyrite veinlets and weak presence of sulfides and copper oxidezed minerals (araound AY-11),* ***B:*** *Photomicrograph of disseminated chalcopyrite in reflected light with secondary enrichment of covellite (AY-09),* ***C:*** *Photomicrograph of coexisting pyrite and chalcopyrite in veinlet with secondary enrichment of covellite around chalcopyrite (AY-10),* ***D:*** *Mixed zone of oxides and supergene enrichment in a zone of stockworks, containing limonite and black and green copper oxides in the PG (around AY-23B),* ***E:*** *Photomicrograph of malaquite and formation of limonites after copper sulfides (around AY-23A),* ***F:*** *Figure 4.10-E in reflected light, showing supergene enrichment of covellite after chalcopyrite in the PG (around AY-23A).*

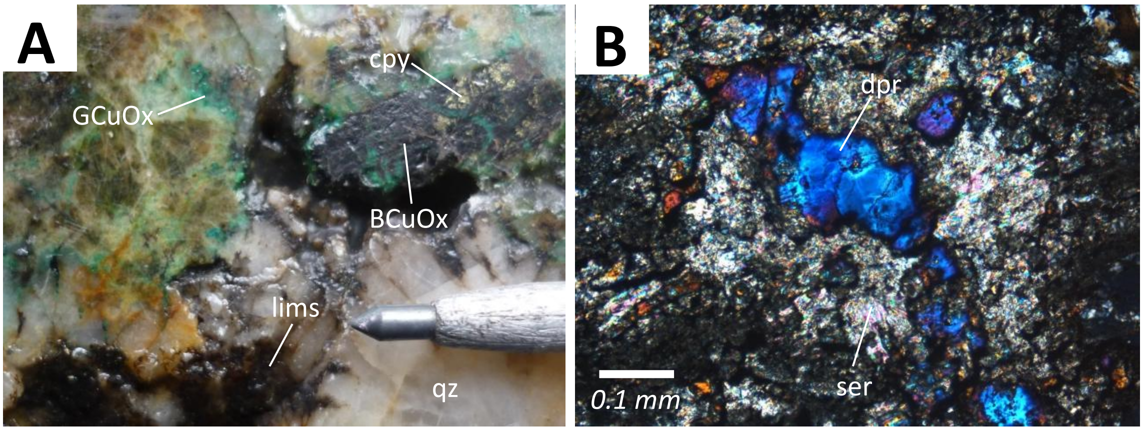

Figure 4.11. A: *Mixed zone of oxides and supergene enrichment showing limonites, black and green copper oxides, chalcopyrite, in the HB (Already AY-38),* ***B:*** *Photomicrograpg of PGD, showing diaspore in the mixed zone of oxides and supergene enrichment with sericite (AY-17).*

4.7. PARAGENETIC SEQUENCE

A paregenetic sequence of alteration and mineralization of the Yanac prospect (Fig. 4.12) is proposed for the diferent assemblages of identified veinlets determinated before. First, the phase A had a precipitation of mainly quartz and pyrite with lower presence of chlorite, albite, carbonates, epidote and K-feldspar with a poor chalcopyrite and molybdenite mineralization.

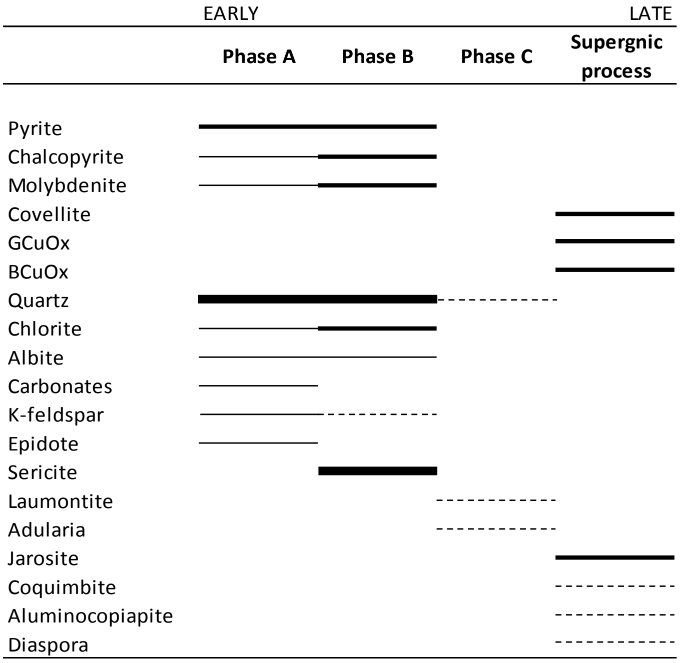

Figure 4.12*. Paragenetic sequence of the alteration and mineralization to the formation of the Yanac prospect. GCuOx: green copper oxides, BCuOx: Black copper oxides.*

Later, a phase B is characterized predominantly by quartz with sericite, moderate chlorite and pyrite, weak albite, traces of K-feldspar and a major mineralization of chalcopyrite and molybdenite in the system. Phase C is characterized by local precipitation of laumontite, quartz and adularia, not altering with considerable intensity the rock. The latest phase, of supergenic process, produce mainly jarosite, secondary covellite, green and black copper oxides, and local presence of coquimbite, aluminocopiapite and diaspore.

4.8. GEOCHEMISTRY

In this study all analyses with less than around 3% of loss on ignition (LOI) were used for chemical characterization of the granites. Chemical analysis data of the selected samples is presented in table 4.2.

The Harker diagrams are useful to present data in a graphical form of major oxides and trace elements in terms of silica, although they do not necessarily represent lines of chemical evolution of parental magmas.

The diagrams (Figs. 4.13, 4.14) of the Yanac prospect show positive linear tendency of SiO_2 with Na_2O, K_2O, Ba, Nb and Ta, except for the trachydacite dyke sample, there is not a good correlation whit the K_2O, probably due to a different magmatic origin. Negative correlations are observed between SiO_2 and Al_2O_3, Fe_2O_3, TiO_2, MgO, CaO, V, Y and Eu, but the trachydacite dyke show a marked difference with the $Al_2O_{3,}$ CaO and Y. Additionally, a positive and a posterior inflexion to a negative tendency in the SiO_2 with Zr and Sr, indicate the domain of the crystallization of a new mineral. The correlations show patterns coherent to the petrography, in this respect, P_2O_5 content depends fundamentally on the apatite, mineral with presence in rocks less differentiated. Moreover, the positive correlations between SiO_2 and Na_2O along with a negative correlation of SiO_2 and CaO is consistent with the decrease of the anorthite content in the plagioclase for the rocks reacher in quartz. The decrease of MgO, CaO and Fe_2O_3 with increase in SiO_2 is related with the decrease of the amphibole proportion in the more evolved rocks. The negative tendency of V is useful pointer to the presence of Fe-Ti oxides (titanomagnetite). Zr is characteristically incompatible in mafic magmas and it may behave as compatible element in zircon-saturated (silicic) magmas. Ba is an incompatible element that substitutes for K in K-

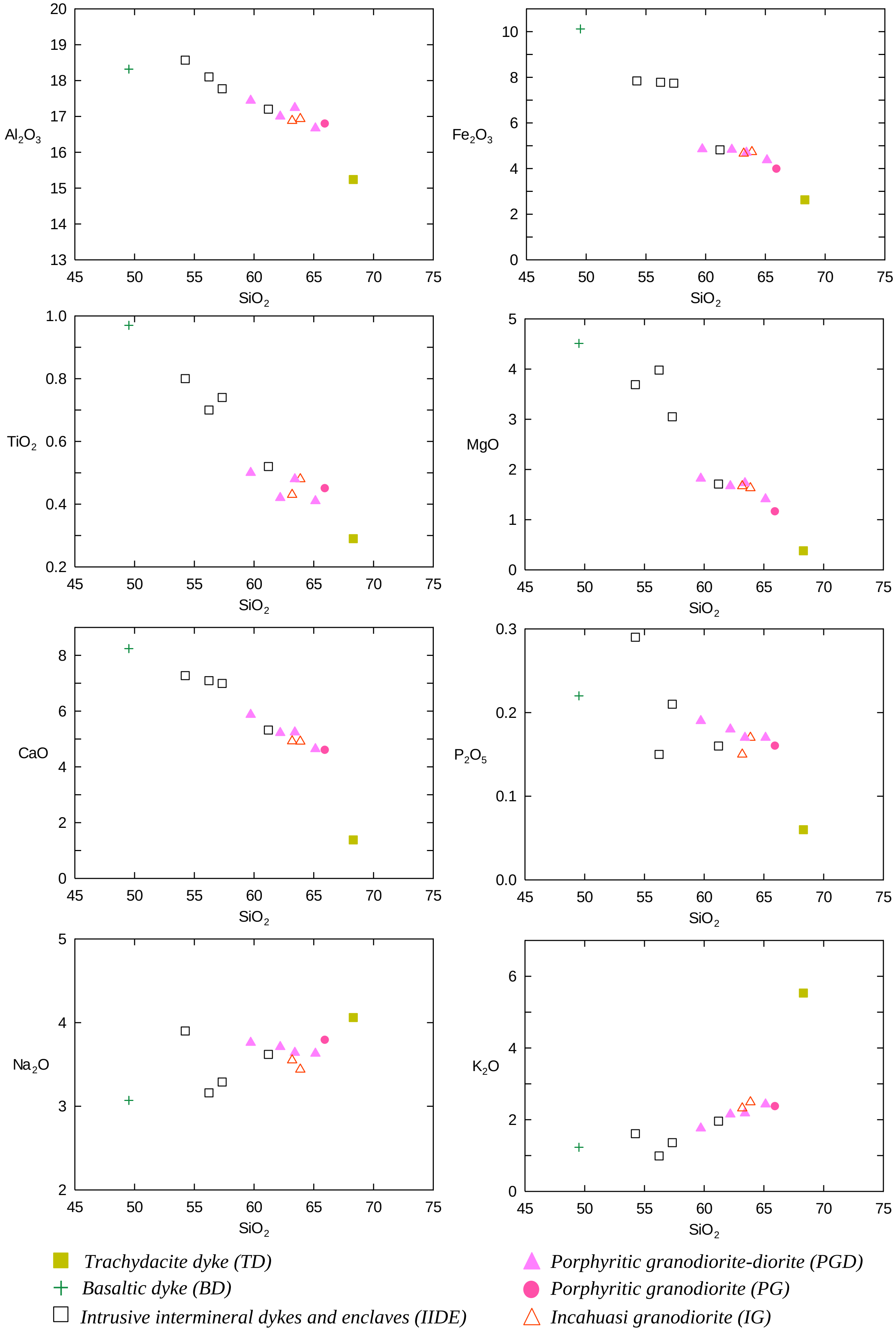

Figure 4.13. *Harker type diagrams of major elements for the rocks of the Yanac prospect.*

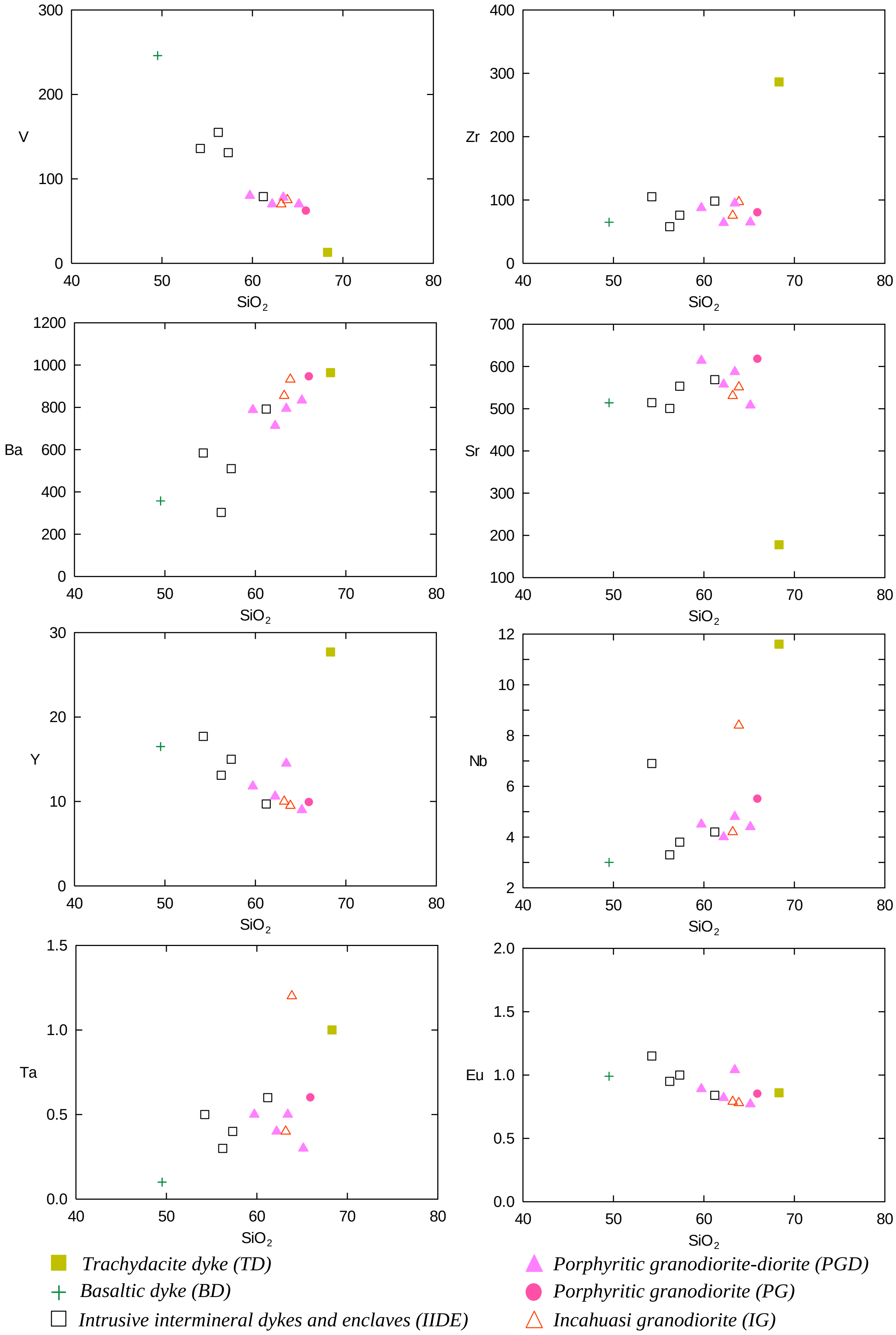

Figure 4.14. *Harker type diagrams of the trace elements for the rocks of the Yanac Intrusive Complex.*

feldspar, micas, or hornblende. Sr and Eu substitute readily for Ca in plagioclase and K in K-feldspar.

Decrease in Sr concentrations indicates feldspar removal from a series of related magmas. Sr is more incompatible under mafic rocks because of the absence of feldspar. Y has a high partition coefficient in amphibole. Its behavior is strongly affected by REE-rich accessory minerals probably such as apatite. Nb and Ta are incompatible elements in most magmas. These elements show that could be substituiting Ti into Ti-rich phases, probably such as titanite or Fe-Ti oxides.

Unaltered samples of the Incahuasi granodiorite (IG), porphyritic granodiorite (PG), porphyritic granodiorite-diorite (PGD) and intrusive intermineral dykes and enclaves (IIDE) (table 4.2) have SiO_2 values from 63.2 to 63.9, 65.95, 59.7 to 65.1 and from 54.2 to 61.2 wt.%, respectively, the basaltic dyke (BD) with 49.5 and trachydacite dyke (TD) with 68.3 wt.%. The total alkalis (Na_2O + K_2O) range from 5.9 to 6.0 wt.% for the IG; 6.2 wt.% for the PG; from 5.5 to 6.1 wt.% for the PGD; from 4.2 to 5.6 wt% for the IIDE; and two samples with different composition with 4.3 wt.% for the basalt and 9.6 wt.% for the trachydacite dykes. According to Middlemost (1985), IG is classified as granodiorite with aproximation to diorite composition; PG is classified as granodiorite; PGD samples, as granodiorite-diorite; gabbroic diorite-diorite-monzodiorite for IIDE; and basalt and trachydacite for later dykes. All rocks are classified as subalkaline series, according to Irving and Baragar (1971) (Figs. 4.15, 4.16, table 4.2).

The rocks have rates of MgO/TiO_2 from 3.4 to 3.9 for the Incahuasi granodiorite (IG), 2.6 for the porphyritic granodiorite (PG), from 3.4 to 4.0 for the porphyritic granodiorite-diorite (PGD), from 3.3 to 5.7 for the intrusive inter-mineral dykes (IIDE) and two samples of 1.3 for the trachydacite and 4.6 for the basalt of the volcanic later dykes; K_2O/Na_2O is from 0.65 to 0.7 for the IG, 0.6 to the PG, 0.5 to 0.7 for the PGD, 0.3 to 0.5 for the IIDE and ratios of 0.4 for the basalt and 1.4 for the trachydacite dykes. Al_2O_3 values vary from 16.88 to 16.93 wt.% for IG, 16.79 for the PG, from 16.7 to 17.4 wt.% for the PGD, from 17.2 to 18.6 wt.% for the IIDE, and of 18.3 wt.% for the basalt and 15.2 wt. % for the trachydacite of the later dykes. CaO from 4.91 to 4.92 wt.% for the IG, 4.6 to the PG, from 4.6 to 5.9 wt.% in the PGD, from 5.32 to 7.27 wt .% to IIDE and of 8.24 wt.% for the basalt and 1.38 wt.% for the trachydacite dykes.

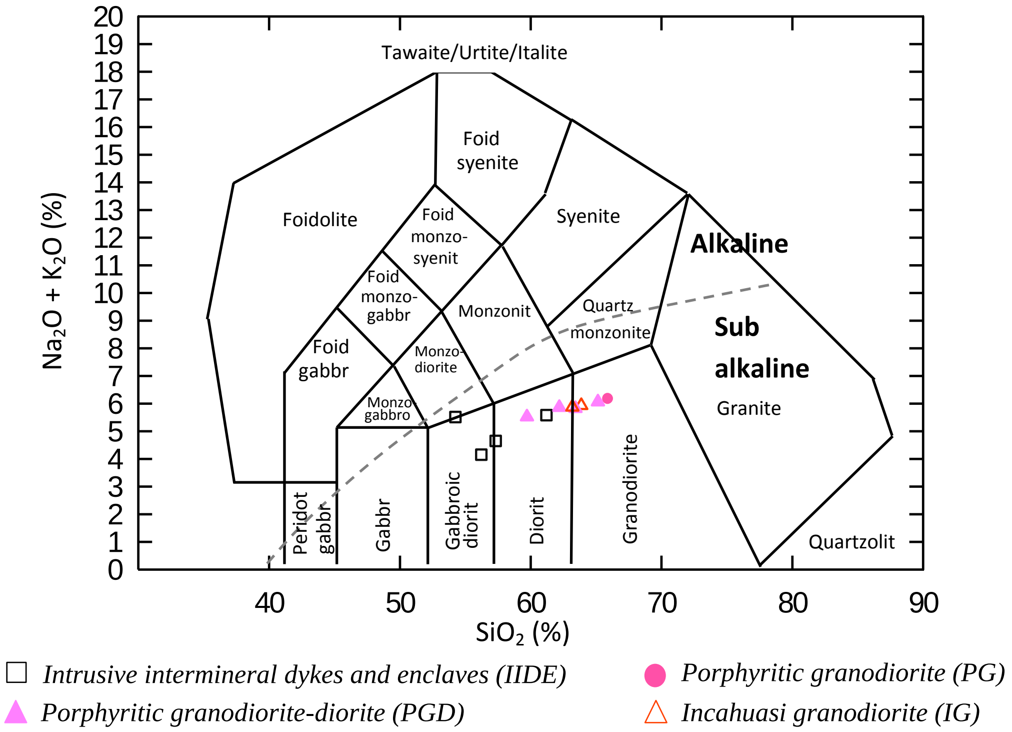

Figure 4.15. *Geochemical classification diagram for the intrusive rocks of the Yanac prospect, according to the proposal of Middlemost (1985). The dashed line represents the division between alkaline and subalkaline series of Irving and Baragar (1971).*

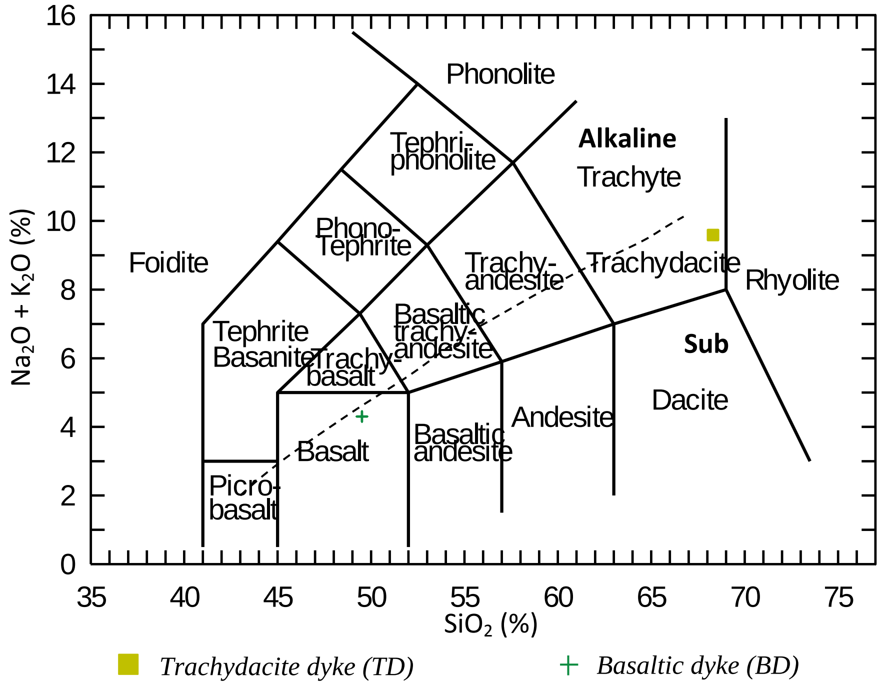

Figure 4.16. *Total alkalis-SiO*$_2$ *(TAS diagram) showing fields for volcanic rock names (LeBas et al., 1986) for samples AY-14 and Ay-42, trachydacite and basalt respectively. The dashed line represents the alkaline compared to subalkaline discrimination from Irvine and Baragar (1971).*

There are Cu low grades from 21 to 57 ppm for the IG, 36 ppm for the PG, from 18 to 191 ppm for the PGD, from 16 to 296 ppm for the IIDE, and 164 for the basalt and 18 ppm for the trachydacite dykes; the content of Mo is from 0.1 to 0.5 ppm for the IG, 2 ppm for the PG, from 0.3 to 4.8 ppm for the PGD, from 0.2 to 1.6 ppm for the IIDE and 0.8 ppm for the basalt and 0.3 ppm for the trachydacite. The Au content is below 0.7 ppb for all unaltered samples.

The geochemical data of the rock samples submitted to hydrothermal alteration mainly show that for the unaltered samples of the porphyritic granodiorite (PG) and porphyritic granodiorite-diorite (PGD), the average content of SiO_2 varies from 63.2 wt.% to 67.7 wt.% in the case of the weak hydrothermal alteration B, to 71.1 wt.% in the case of the strong hydrothermal alteration B, and 73.2 wt.% for the hydrothermal breccia (HB), indicating an input of silica of the related solutions to the system and favoring quartz deposition in veinlets. K_2O varies from 2.2 wt.% (PG and PGD) to 4.1 wt.% in the weak hydrothermal alteration B, and to 9.2 wt.% in the strong hydrothermal alteration B (table 4.2), evidenced by the presence of sericite in the alteration. It is 1.0 wt% in the HB, coherent with the absence of sericite in the samples. Fe_2O_3, MgO, CaO and Na_2O vary from an average of 4.7 wt.% (PG and PGD) to 2.8 wt.% (weak hydrothermal alteration B) and 1.5 wt.% (strong hydrothermal alteration B) for Fe_2O_3; 1.7 wt. % (PG and PGD) to 1.0 wt.% (weak hydrothermal alteration B), 0.26 wt.% (strong hydrothermal alteration B) and 0.63 wt.% (HB) for MgO; from 4.6 wt.% (PG and PGD) to 2.8 wt.% (weak hydrothermal alteration B) and 0.18 wt.% (strong hydrothermal alteration B) for CaO; and from 3.0 wt.% (PG and PGD) to 2.8 wt.% (weak hydrothermal alteration B), 0.75 wt.% (strong hydrothermal alteration B) and 0.37 wt.% (HB) for Na_2O, coherent with hydrothermal alteration of the ferromagnesian and plagioclase primary minerals. In the case of the HB, there are also higher Fe_2O_3 and CaO values, respectively 5.63 wt.% and 6.48 wt.%, indicating that there is coexistence of hydrothermal alteration A with Weak hydrothermal alteration B (table 4.2, Figs. 4.7, 4.8, 4.9).

Table 4.2. *Major and trace element in whole-rock data, mayor oxide values are in weight percent, while trace elements are reported in ppm. *Au in ppb.*

	Incahuasi granodiorite (IG)		Porphyritic granodiorite (PG)	Porphyritic granodiorite-diorite (PGD)				Intrusive inter-mineral dykes and enclaves (IIDE)				Trach. dyke (TD)	Basal. dyke (BD)	Weak hydrothermal alteration B			Strong hydrothermal alteration B		Hydrothermal breccia (HB)
%	**AY-01**	**AY-45**	**AY-22**	**AY-05**	**AY-39**	**AY-19**	**AY-21**	**AY-03**	**AY-32**	**AY-40**	**AY-41E**	**AY-14**	**AY-42**	**AY-17**	**AY-18**	**AY-23D**	**AY-41B**	**AY-41D**	**AY-38**
SiO_2	63.87	63.19	65.95	59.72	62.19	63.42	65.14	61.2	57.33	56.23	54.24	68.31	49.52	67.29	71.7	63.98	70.63	71.57	73.22
TiO_2	0.48	0.43	0.45	0.5	0.42	0.48	0.41	0.52	0.74	0.7	0.8	0.29	0.97	0.39	0.63	0.46	0.32	0.46	0.2
Al_2O_3	16.93	16.88	16.79	17.44	17	17.24	16.67	17.2	17.77	18.1	18.57	15.24	18.32	16.25	14.82	16.44	13.97	14.27	8.32
Fe_2O_3	4.73	4.66	3.98	4.85	4.83	4.7	4.37	4.82	7.74	7.78	7.84	2.63	10.12	3.33	0.34	4.87	1.56	1.5	5.03
MnO	0.06	0.12	0.07	0.09	0.06	0.08	0.07	0.08	0.16	0.15	0.23	0.06	0.18	0.04	0.02	0.1	<0.01	<0.01	0.12
MgO	1.63	1.67	1.16	1.82	1.67	1.73	1.41	1.71	3.05	3.98	3.69	0.38	4.51	1.06	0.25	1.61	0.17	0.35	0.63
CaO	4.91	4.92	4.6	5.87	5.22	5.24	4.64	5.32	6.99	7.09	7.27	1.38	8.24	3.77	0.55	4.14	0.17	0.19	6.48
Na_2O	3.44	3.55	3.79	3.76	3.71	3.64	3.63	3.62	3.29	3.16	3.9	4.06	3.07	3.44	2.28	2.63	0.59	0.91	0.37
K_2O	2.49	2.32	2.37	1.76	2.15	2.18	2.43	1.96	1.36	0.99	1.61	5.53	1.23	2.24	8.05	1.99	10.56	7.89	1
P_2O_5	0.17	0.15	0.16	0.19	0.18	0.17	0.17	0.16	0.21	0.15	0.29	0.06	0.22	0.14	0.1	0.18	0.03	0.05	0.07
LOI	1.00	1.8	0.4	3.8	2.3	0.8	0.8	3.2	1.1	1.4	1.3	1.8	3.4	1.7	0.7	2.9	1.8	2.6	3.8
TOT/C	0.02	0.02	0.02	0.02	0.02	0.02	0.02	0.02	<0.02	<0.02	<0.02	0.19	0.2	0.02	<0.02	<0.02	0.02	<0.02	0.6
TOT/S	0.02	0.02	0.02	0.02	0.02	0.02	0.02	0.02	<0.02	<0.02	<0.02	<0.02	<0.02	0.05	<0.02	<0.02	0.07	0.09	0.02
Sum	99.72	99.69	99.73	99.74	99.77	99.73	99.76	99.75	99.74	99.77	99.76	99.74	99.76	99.67	99.43	99.34	99.78	99.76	99.24
A/CNK	0.98	0.98	0.98	0.93	0.95	0.96	0.98	0.97	0.91	0.94	0.87	1.00	0.86	1.09	1.10	1.17	1.10	1.37	0.62
FeOt/(FeOt+MgO)	0.73	0.72	0.76	0.71	0.73	0.71	0.74	0.72	0.70	0.64	0.66	0.86	0.67	0.74	0.55	0.73	0.89	0.80	0.88
ppm																			
Ba	932	855	945	788	713	794	833	792	510	303	584	964	357	911	2848	776	852	753	168
Be	1	<1	1	<1	3	3	<1	2	3	<1	3	2	<1	<1	1	2	<1	<1	<1
Co	8	48.1	4.7	6.7	4.4	7.6	6.8	6.8	14.8	17.4	15.3	2.3	22.3	3.9	1.9	2.9	1.6	0.9	6.5
Cr	30	<20	40	<20	30	20	40	40	<20	50	<20	20	<20	60	<20	<20	<20	30	20
Cs	1.3	5.5	3.7	1.3	1	1.6	6.1	2.5	2.1	3.9	1.6	2.4	9.7	3.9	2.2	5.4	3	3.2	3
Ga	17.8	15.1	17	17.1	15.8	17.4	15	17.2	18.1	16.7	18.1	14.1	18.1	16.3	7.8	17.1	15.6	18.4	14.6
Hf	2.9	2.3	2	2.3	2.1	2.6	1.7	3.2	2.7	1.9	3.6	7.8	1.7	2	8.7	2.3	1.8	3.1	1.4
Nb	8.4	4.2	5.5	4.5	4	4.8	4.4	4.2	3.8	3.3	6.9	11.6	3	5.9	8.4	4.3	4.5	5.1	5.1
Rb	59.2	62	61.4	41.2	52.5	48.5	61.9	50.5	36.9	39.4	41.8	183.3	50.7	60.8	250.7	57	283.5	201.3	49.2
Sc	6	7	5	8	7	7	6	7	13	17	14	6	22	5	10	8	4	5	4
Sn	107	3	5	12	4	8	5	15	4	5	4	10	4	7	7	5	8	8	108
Sr	551	530.4	617.4	613.9	557.5	587.1	508	568.8	553.1	500.6	514.2	177.8	513.9	587.7	242.8	483.7	116	171	515.6
Ta	1.2	0.4	0.6	0.5	0.4	0.5	0.3	0.6	0.4	0.3	0.5	1	0.1	0.5	0.7	0.4	0.5	0.4	0.7
Th	7.1	6.1	5.6	4.8	4.4	5.8	5.8	5.5	3.6	3.3	6.9	21.5	1.8	5.2	28.9	5.4	6. 7	7.1	4.1

It continues next page

Table 4.2. *(Continued).*

	Incahuasi granodiorite (IG)		Porphyritic granodiorite (PG)	Porphyritic granodiorite-diorite (PGD)				Intrusive inter-mineral dikes and enclaves (IIDE)				Trach. dyke (TD)	Basal. dyke (BD)	Weak hydrothermal alteration B			Strong hydrothermal alteration B		Hydrothermal breccia (HB)
ppm	**AY-01**	**AY-45**	**AY-22**	**AY-05**	**AY-39**	**AY-19**	**AY-21**	**AY-03**	**AY-32**	**AY-40**	**AY-41E**	**AY-14**	**AY-42**	**AY-17**	**AY-18**	**AY-23D**	**AY-41B**	**AY-41D**	**AY-38**
U	1.4	2	1.3	1.1	1.8	1.4	1.6	1.5	1	0.7	2.2	5.9	0.6	1.5	5.7	1.7	2.8	2.5	1.7
V	75	70	62	80	70	78	70	79	131	155	136	13	246	60	63	79	34	48	85
W	2.6	324.5	0.9	1.3	0.9	2	1.8	1.1	1.5	1.5	1.1	2.4	0.8	2	10.7	1.8	27.7	27.4	4.8
Zr	97	75.4	80.1	87.5	64	94.7	64.7	98.2	76	57.9	105.1	286.3	64.9	82.8	335.7	71.3	59.2	101.4	42
Y	9.5	10	9.9	11.8	10.6	14.5	9	9.7	15	13.1	17.7	27.7	16.5	10.1	19.5	11.7	2.7	2.2	7.1
Ag	<0.1	<0.1	<0.1	<0.1	<0.1	0.1	<0.1	<0.1	0.2	0.2	<0.1	<0.1	0.5	0.7	0.2	1	13.7	6.5	3.4
As	<0.5	1	<0.5	<0.5	0.6	<0.5	<0.5	0.6	<0.5	1	0.7	1	2.4	1	0.7	1.6	<0.5	<0.5	1.9
***Au**	0.6	<0.5	0.6	<0.5	<0.5	0.7	<0.5	<0.5	<0.5	<0.5	0.6	<0.5	<0.5	7.2	<0.5	9.1	42.4	33.1	0.7
Bi	<0.1	<0.1	<0.1	<0.1	<0.1	<0.1	<0.1	<0.1	<0.1	<0.1	<0.1	<0.1	<0.1	<0.1	0.3	0.2	0.6	0.7	0.2
Cd	<0.1	<0.1	0.1	0.4	0.1	<0.1	0.2	0.2	1.4	0.5	0.6	1	0.6	<0.1	<0.1	0.4	<0.1	<0.1	0.5
Cu	56.5	20.6	36	71.3	18.2	190.9	23.9	15.5	89	295.8	24.7	17.8	164	514.3	751.3	3627.7	319.2	367	4512.6
Hg	<0.01	<0.01	<0.01	<0.01	<0.01	<0.01	<0.01	<0.01	<0.01	<0.01	<0.01	<0.01	<0.01	0.02	<0.01	0.01	<0.01	<0.01	0.01
Mo	0.1	0.5	1.9	0.5	4.8	0.6	0.3	1.6	0.3	0.4	0.2	0.3	0.8	46.7	61	10.9	7.6	62.7	239.6
Ni	2.2	2.2	1.9	2.2	1.9	2.1	2.2	2.7	1.9	7.5	5.4	0.9	4.5	2	1.3	5	0.5	1	1.7
Pb	0.8	8.2	1	1.3	1.3	0.7	1.4	1.2	9.5	1.4	1	3.1	31.1	1.2	8.4	1.1	2	3.8	7.7
Sb	<0.1	0.1	<0.1	<0.1	<0.1	<0.1	<0.1	<0.1	<0.1	<0.1	<0.1	<0.1	<0.1	<0.1	0.1	0.1	0.1	0.1	0.6
Se	<0.5	<0.5	<0.5	<0.5	<0.5	<0.5	<0.5	<0.5	<0.5	<0.5	<0.5	<0.5	<0.5	<0.5	<0.5	<0.5	4.1	4.9	2.5
Tl	<0.1	<0.1	<0.1	<0.1	<0.1	<0.1	<0.1	<0.1	<0.1	<0.1	<0.1	<0.1	<0.1	<0.1	<0.1	<0.1	<0.1	<0.1	<0.1
Zn	18	40	16	55	17	19	26	28	248	76	63	59	94	35	11	132	4	11	35
La	21.9	19.4	22.4	17.9	13	28.9	17.7	20.4	13.4	13.4	18.2	35.3	10.3	18.8	18.1	14.1	6.4	5.8	43
Ce	41.6	36.8	41.3	36.2	25.4	56	31.1	39	30.2	26	42.8	71.6	25	37	43.2	27.4	10.3	9.2	72.3
Pr	4.21	3.88	4.3	4.02	2.99	6.07	3.45	4.13	3.47	2.8	5.24	8.03	3.25	4.08	4.68	3.18	1.06	0.97	7.79
Nd	16.1	12.3	16.8	16.4	12	18.4	13.5	13.2	13.4	11.9	23.6	30.7	14.5	16.7	19	11.9	3.1	4.3	25.3
Sm	2.49	2.67	2.94	3.02	2.57	3.87	2.33	2.74	2.98	2.33	4.43	6.01	3.43	3	3.52	2.66	0.65	0.77	3.48
Eu	0.78	0.79	0.85	0.89	0.82	1.04	0.77	0.84	1	0.95	1.15	0.86	0.99	0.82	0.31	0.78	0.12	0.18	0.81
Gd	2.16	2.25	2.48	2.55	2.22	3.06	2.13	2.36	2.87	2.61	3.98	5.32	3.5	2.34	3.3	2.19	0.48	0.55	2.63
Tb	0.29	0.32	0.34	0.34	0.32	0.46	0.27	0.32	0.44	0.36	0.54	0.77	0.49	0.32	0.5	0.33	0.07	0.08	0.27
Dy	1.65	2.1	1.62	1.77	2.12	2.42	1.83	1.94	2.51	2.11	3.32	4.72	2.9	1.86	3.3	2.23	0.33	0.49	1.17
Ho	0.32	0.35	0.33	0.33	0.33	0.5	0.32	0.34	0.51	0.43	0.67	0.9	0.65	0.33	0.64	0.4	0.09	0.1	0.2
Er	0.88	1.02	0.86	1.14	1.16	1.48	0.98	1.02	1.56	1.46	2.01	3.07	1.75	0.96	1.72	1.19	0.35	0.32	0.64
Tm	0.15	0.17	0.14	0.18	0.18	0.21	0.14	0.15	0.22	0.2	0.29	0.41	0.26	0.16	0.31	0.17	0.06	0.05	0.09
Yb	1	0.98	1.07	1.14	1.29	1.49	1	1.16	1.6	1.3	1.67	3.07	1.74	0.91	1.89	1.21	0.46	0.41	0.59
Lu	0.17	0.17	0.18	0.19	0.16	0.22	0.17	0.18	0.21	0.17	0.28	0.45	0.23	0.15	0.25	0.18	0.1	0.06	0.1

The analyzed samples belong to calc-alkaline series , except for the trachydacite dyke (sample AY-14), , according to Peccerillo and Taylor (1976) classification (Fig. 4.17).

Regarding the alumina saturation index (ASI = Al_2O_3 / (CaO + Na_2O + K_2O) (molar), the analyzed rocks are mainly classified as metaluminous. Sample AY-14 has higher aluminum saturation index (ASI) and lower A/Na+K. It is plotted between mataluminous to peraluminous fields (Fig. 4.18).

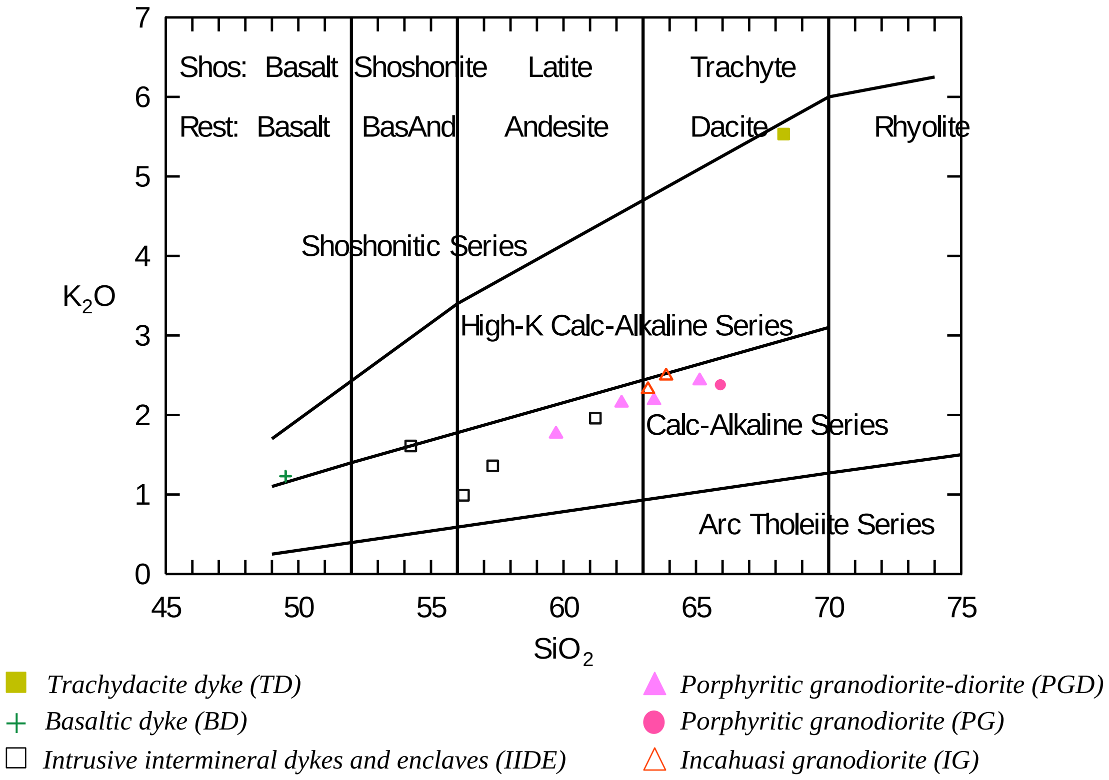

Figure 4.17. *Diagram of Peccerillo and Taylor (1976) to distinguish different types of series in subalkaline rocks.*

Some authors propose that some trace elements and rare earth elements can be used to help constain the tectonic setting of granites, as well as the petrogenetic histories of the rocks. Among them, tectonic discrimination diagrams proposed by Pearce *et al.* (1984) are widely used. In these diagrams, the samples of the Yanac prospect are grouped into the field of volcanic arc granites (Fig. 4.19).

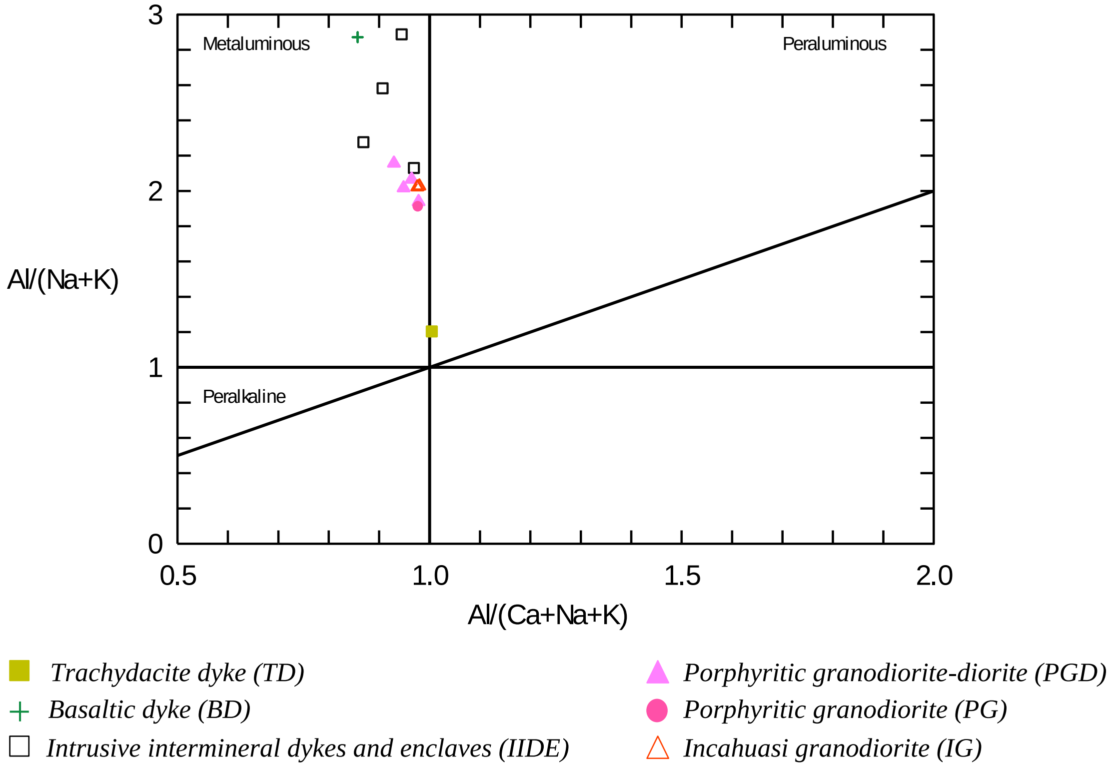

Figure 4.18. *A/NK vs A/CNK (molar) diagram, Maniar & Piccoli (1989).*

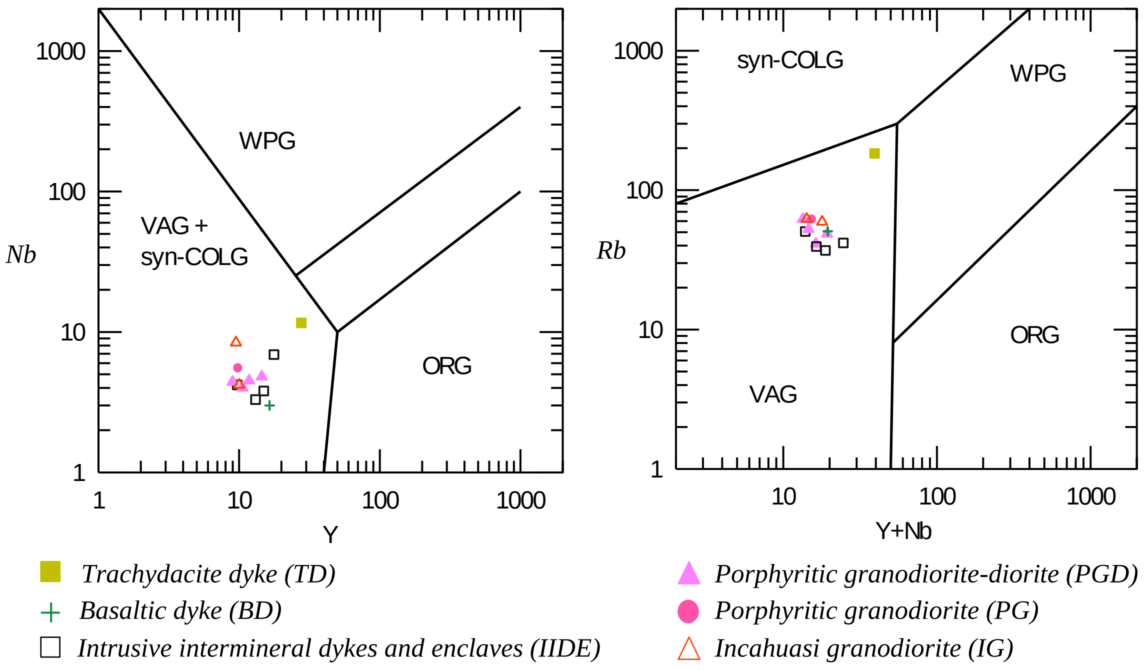

Figure 4.19. *Nb vs. Y and Rb vs. Y+Nb tectonic discrimination diagram of Pearce et al. (1984) for granitic rocks. Ocean Ridge Granites (ORG), Syn-colisional Granites (syn-COLG), Volcanic Arc Granites (VAG), Within Plate Granites (WPG).*

The behavior of the rare earth elements depends on the partition coefficient between a crystalline solid and a liquid (magma). The patterns of rare earth elements (REE) can help in identifying the type of magma in relation to tectonic setting.

A first observation in relation to the patterns of the REE of the analyzed samples (Fig. 4.20) is uniformity. Anomalous behavior is noted in relation to the content of silica, as the sample of trachydacite composition (sample AY-14) of later dykes that is more enriched in REE in relation to the other and has negative Eu anomaly, consistent with its possible magmatic evolution. The second observation in relation to the patterns is the LREE enrichment in relation to the HREE. This could mean that there was involvement of thick continental crust, or subducted sediments with fluids (Winter, 2009).

REE spectra of the samples are moderately fractionated. The ratio Lan / Ybn varies from 14.2 to 15.7 in the IG, is 15.0 for the PG, from 7.2 to 14.0 in the PGD, from 6.0 to 12.6 in the IIDE, 4.2 for the basalt and 8.2 for the trachydacite dykes.

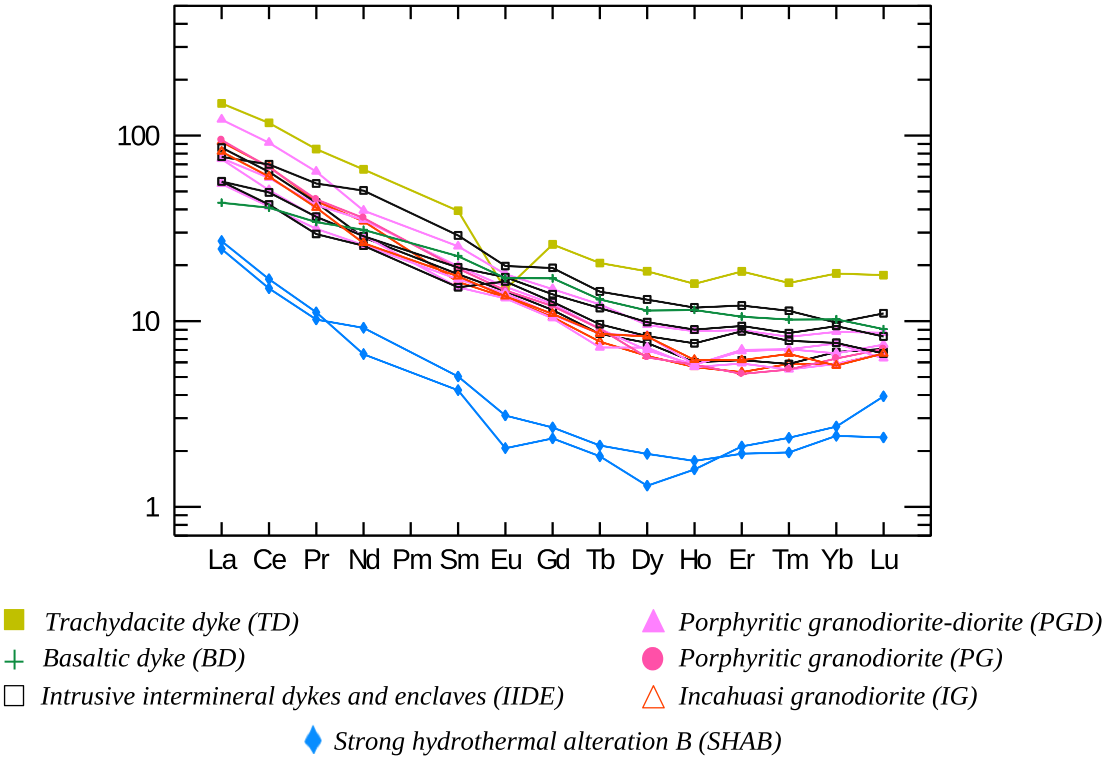

Figura 4.20. *Diagram of Rare Earth Elements for the samples of the Yanac prospect, normalized to chondrite of Sun and McDonough (1989).*

Using a multielementar diagram according to the scheme proposed by Wood *et al.* (1979), with LILE (Large Ion Litophile Elements) in the left and HFSE (High Field Strength Elements) on the right, normalized to the primordial mantle (Fig. 4.21), it is observed enrichment of LILE in relation to HFSE, positive anomaly of Sm, which is common in volcanic arc rocks (Pearce *et al.*, 1984). The enrichment in these elements is attributed to a change in the mantle wedge by aqueous fluids derived from dehydration of an altered oceanic crust and the subducted sediments (Winter, 2009) and negative anomaly of Ta and Nb, characteristic of magmas in subduction zones (Winter, 2009).

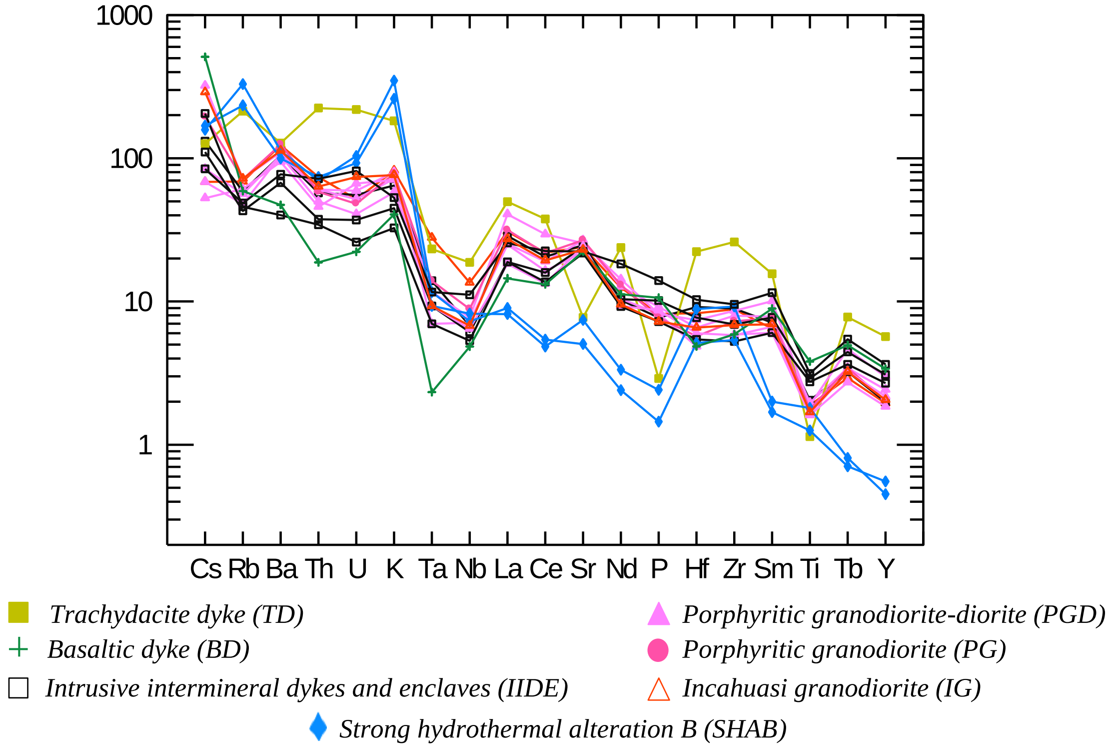

***Figure 4.21**. Multielementar diagram for samples of the Yanac prospect, normalized to the primordial mantle according the order proposed by Wood et al. (1979).*

4.10. RADIOGENIC ISOTOPES

U-Pb and Lu-Hf isotopic compositions from zircon crystals of different granitic rocks were obtained in order to help the distinction of different generations of magmatism and related mineralization.

4.10.1. U-Pb

The results obtained for the samples are presented in the annex 4. The obtained data are interpreted as the granites crystallization ages. For the Incahuasi granodiorite, data range from around 68 to 81 Ma., with a slight differential association of populations of zircons, one being the group of zircons concentrated around of 71 Ma., with a representative age of 70.6 ± 1.0 Ma. obtained (Fig. 4.3, sample AY-45, Fig. 4.22). The other possibles populations ages are interpreted as an inheritance from older magmatic pulses.

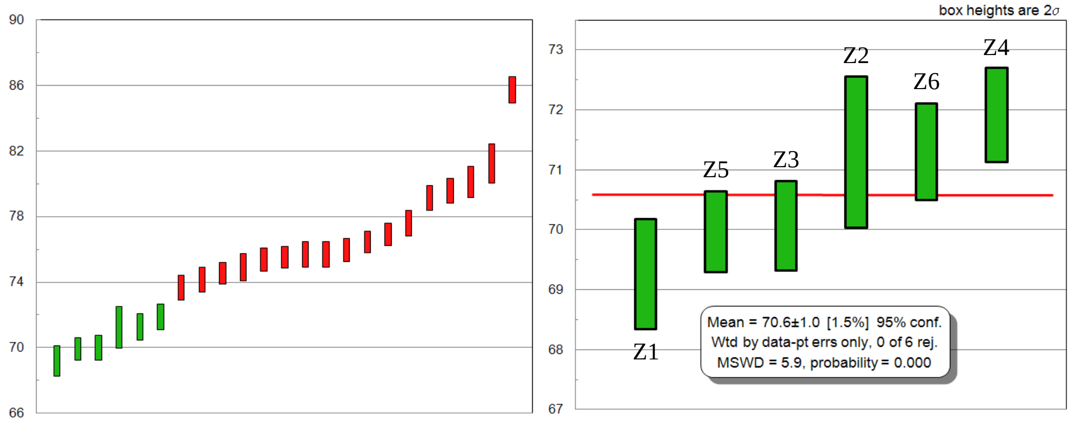

Figure 4.22. *U-Pb ages in zircons of the Incahuasi granodiorite.of the sample AY-45, and zircons used to obtain the age of the rock .*

In this sense, the ages obteined for the porphyritic granodiorite vary from 70 to 80 Ma. Although their relative emplacement observed in the field in relation to the Incahuasi granodiorite is posterior, this unit has a slight higher age with a small population of 71.0 ± 1.0 Ma., indicating that this inconsiderable difference is within an error of 1 Ma. for both lithologhical units. These zircons are interpreted as the last magmatic crystallization phase of the unit, although there is a less dispersed and larger population with older ages that represent inheritance of previous magmatic zircons (Fig. 4.3, sample AY-22, Fig. 4.23).

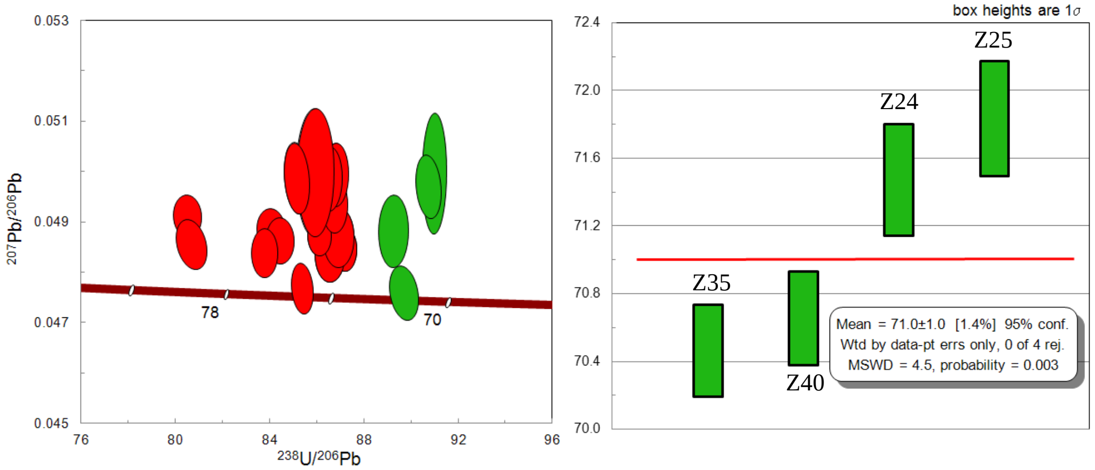

Figure 4.23. *U-Pb* Tera-Wasserburg diagram *to the porphyritic granodiorite of the sample AY-22 and zircons used to obtain the age of the rock.*

Following the same criteria of the younger zircons representing the last stages of crystallization, an intercept at 67.75 ± 0.80 Ma. was obtained for a population of zircon crystals from the porphyritic granodiorite-diorite (Fig. 4.3: sample AY-21; Fig. 4.24), in ages that vary from 66 to 80 Ma.

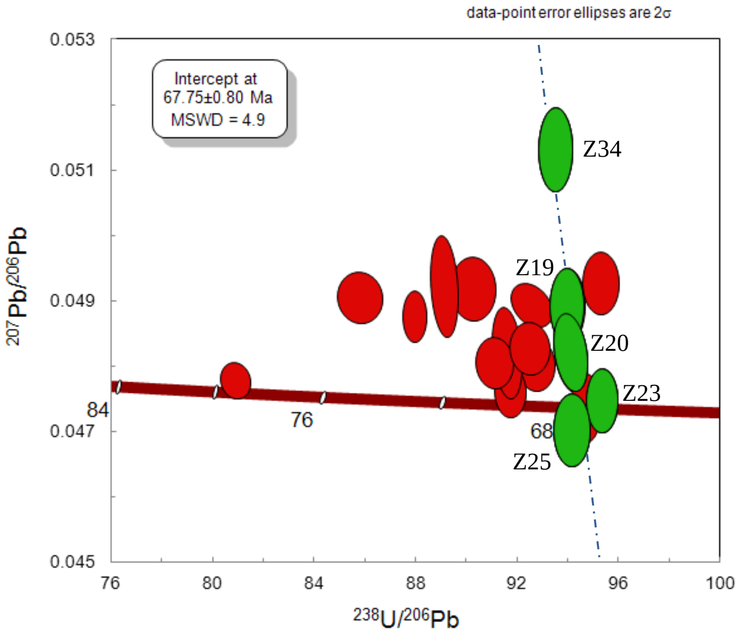

Figure 4.24. *U-Pb Tera-Wasserburg diagram to the porphyritic granodiorite-diorite, with zircons used to obtain the age of the rock. Sample AY-21*

4.10.2. Lu-Hf

Hafnium isotopes were analyzed on each dated zircon of the representative populations of crystallization, to constrain the nature of the magma source.

The zircon crystals selected for the Lu-Hf analyses are from the zircons used to obtain the ages from the porphyritic granodiorite (AY-22) and from the porphyritic granodiorite-diorite (AY-21). T_{DM} values of the studied rocks generally varies between 460 and 740 Ma (Fig. 4.25), indicating a similar evolution trend. εHf(T) calculated values from the PG vary between +0.5 and +6.65; and from -0.28 to +4.75 for the PGD (annex 5), which are coherent with mantle-derived magma, with contribution from the continental crust.

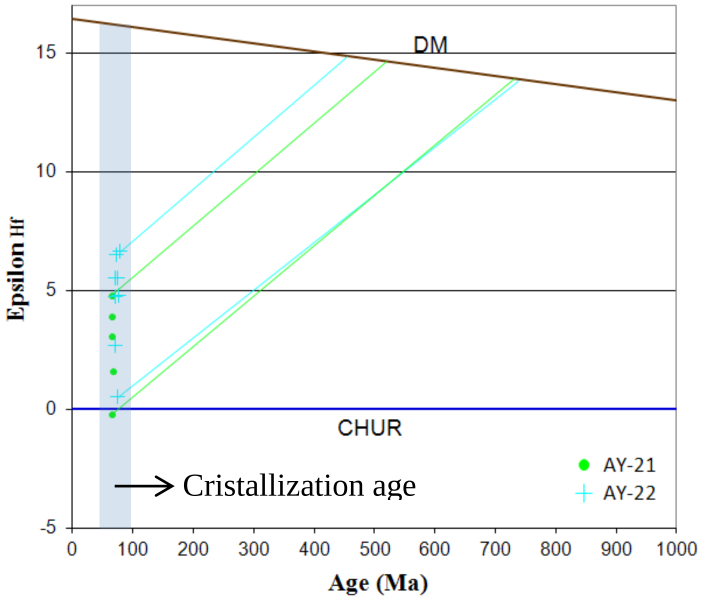

Figure 4.25. *Isotopic evolution diagram of εHf(T) through time with the evolution models of CHUR and depleted mantle (DM). Crystallization age for porphyritic granodiorite (AY-22) is 71.0 Ma., and for the porphyritic granodiorite-diorite (AY-21) is 67.8 Ma., determined by U-Pb method.*

4.10.3. Nd and Sr

Results of Sm-Nd and Rb-Sr isotope are summarized in annex 6. The diagram of isotopic correlation $^{143}Nd/^{144}Nd$ in relation to the $^{87}Sr/^{86}Sr$, shows the relative positions of the isotope data in the studied zone. The Incahuasi granodiorite, porphyritic granodiorite, porphyritic granodiorite-diorite, intrusive intermineral dykes, enclaves and basaltic dykes have an εNd from -1.11 to 1.72 and $^{87}Sr/^{86}Sr$ (i) from 0.70450 to 0.70472, interpreted as a source mainly of the depleated mantle. The Nd T_{DM} values of these lithological units generally vary between 520 and 850 Ma. The trachydacite dyke has an εNd of -2.33 and $^{87}Sr/^{86}Sr$ (i) of 0.70778 and TDM of 850, which suggest that this unit was derived from materials with crustal affinities (Fig. 4.26).

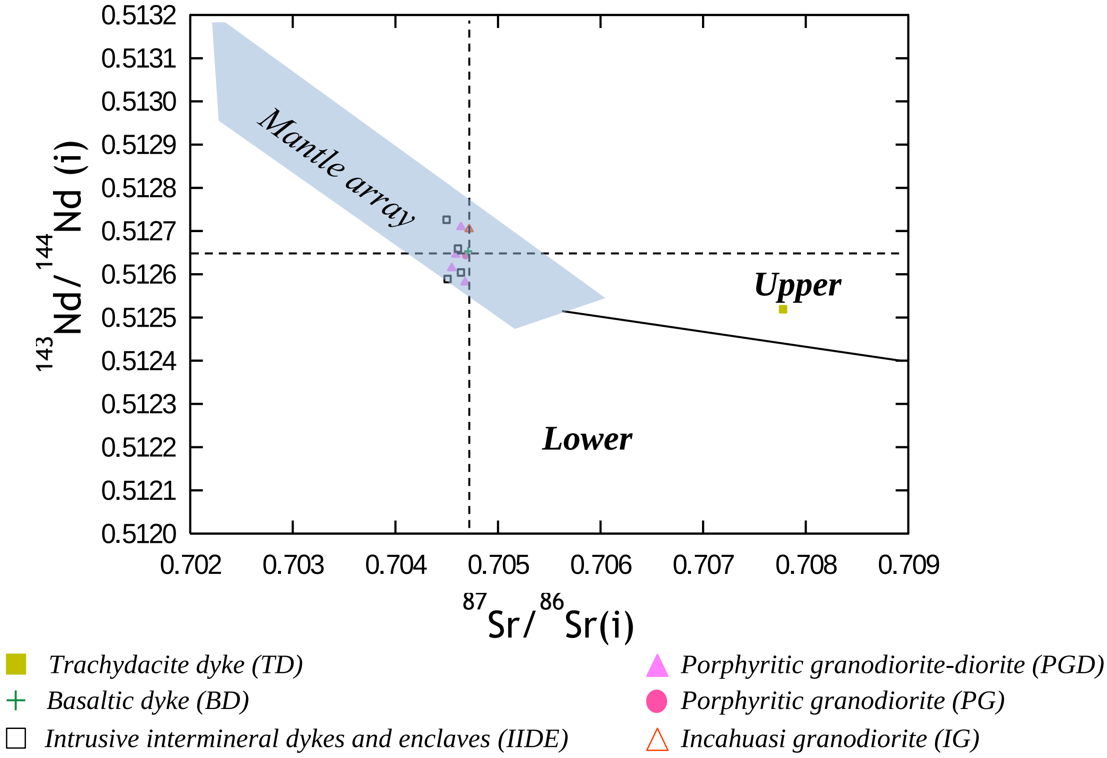

Figure 4.26. *143Nd/144Nd(i) vs.*87Sr/86Sr(i) isotope correlation diagram showing the relative positions of depleted and enriched mantle sources. Most non-enriched mantle reservoirs plot in the upper left "depleted" quadrant, whereas most crustal rocks plot in the lower right "enriched" quadrant. Upper and lower crust tend to plot in different positions in the cristal quadrant, Rollinson (1993).

4.9. MINERAL CHEMISTRY

As a tool to characterize chemically and petrologically some essential minerals, as well as to contribute to the understanding of the conditions of crystallization of the granitic rocks and tectonic environment, biotite and amphibole were analyzed by electron microprobe.

4.9.1. Biotite

According to the International Mineralogical Association (IMA) (Rieder *et al.*, 1999) classification scheme, biotite crystals in the studied samples fall within the field outlined by four end members: annite [$KFe^{2+}_3AlSi_3O_{10}(OH)_2$], siderophyllite

[$KFe^{2+}_2AlAl_2Si_2O_{10}(OH)_2$], phlogopite [$KMg_3AlSi_3O_{10}(OH)_2$], and eastonite [$KMg_2AlAl_2Si_2O_{10}(OH)_2$]. The biotite data in the Yanac prospect are presented in the annex 2. The biotite was plotted in a diagram Mg / (Mg + Fe) x Al^{IV} for Li-poor trioctahedral micas (Fig. 4.27). For the four types of lithological units (PG, IG, IIDE, PGD) the mineral is located in the between annite and phlogopite, with XFe = Fe / (Fe + Mg) between 0.32 and 0.47 for the porphyritic granodiorite (PG), between 0.41 and 0.42 for the regional intrusive Incahuasi (IG), between 0.42 and 0.44 for the inter-mineral intrusive dykes and enclave (IIDE), and 0.41 for the porphyritic granodiorite-diorite (PGD). Moreover, there is a considerable dispersion in relation to the content of Al^{IV} (2.1 to 2.4, 2.2 to 2.3, 2.1 to 2.3 and 2.3 for the last one, respectively). The contents of TiO_2 and BaO are high, with average values of 4.2% and 0.5% for PG, 4.1% and 0.7% for the IG, 4.1% with 0.7% for the IIDE and 3.7% and 0.8 for the PGD (annex 2).

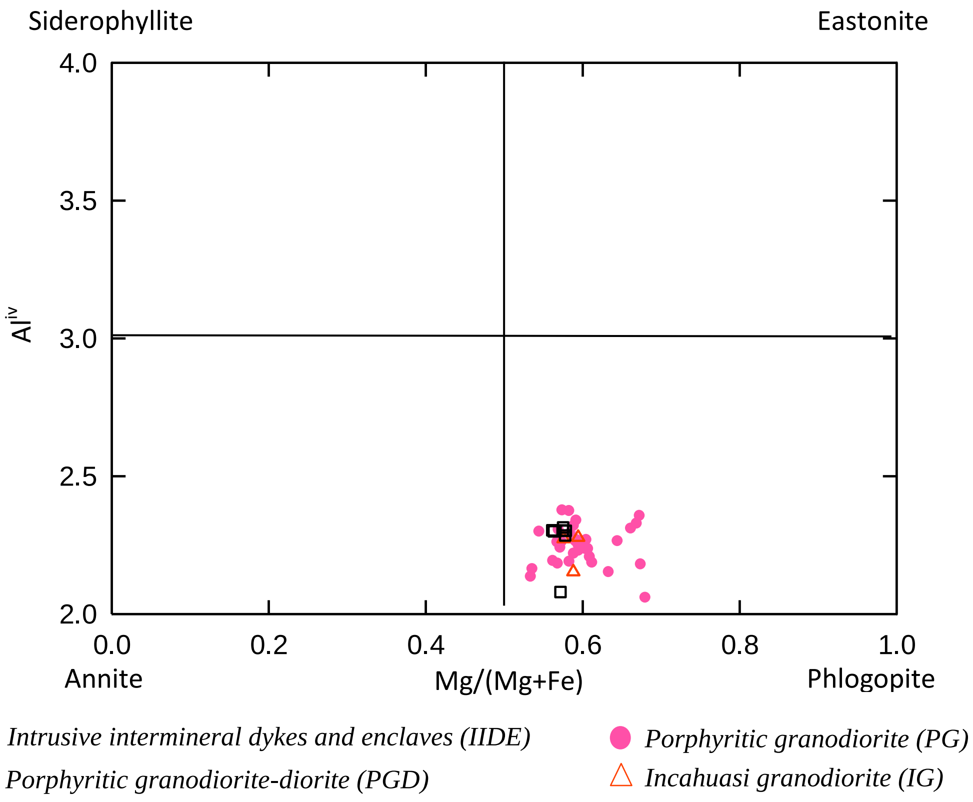

Figure 4.27. *Biotite compositions for the PG, IG, IIDE and PGD of the Yanac system in a Mg/(Mg+Fe) x* Al^{iv} *(a.f.u) diagram, Rieder et al., 1999.*

The biotite interpreted as primary in the petrography of PG on the zones with presence of alteration as well as undisturbed areas have high TiO_2 values, with a range of 3.0 to 4.8%, MgO contents between 10.2 and 15, 4% and Al_2O_3 from 12.7 to 17.0%. The primary biotite of IG rocks have TiO_2 content in the range from 4.0 to 4.1%, MgO and Al_2O_3 content with values between 13.5 and 13.9% and 12.9 and 13.6%, respectively. The IIDE biotites show TiO_2 values between 3.8 and 4.4%, MgO between 12.6 and 13.6 and Al_2O_3 between 12.6% and 13.4%. The PGD biotite has 3.7% TiO_2, 14.0% MgO and 13.7% Al_2O_3 (Annex 2). The different biotites of the lithologic units defined by petrography are chemically discriminated in the triangular diagram of Nachit *et al.* (2005) (Fig. 4.28). All fall in the primary biotites field.

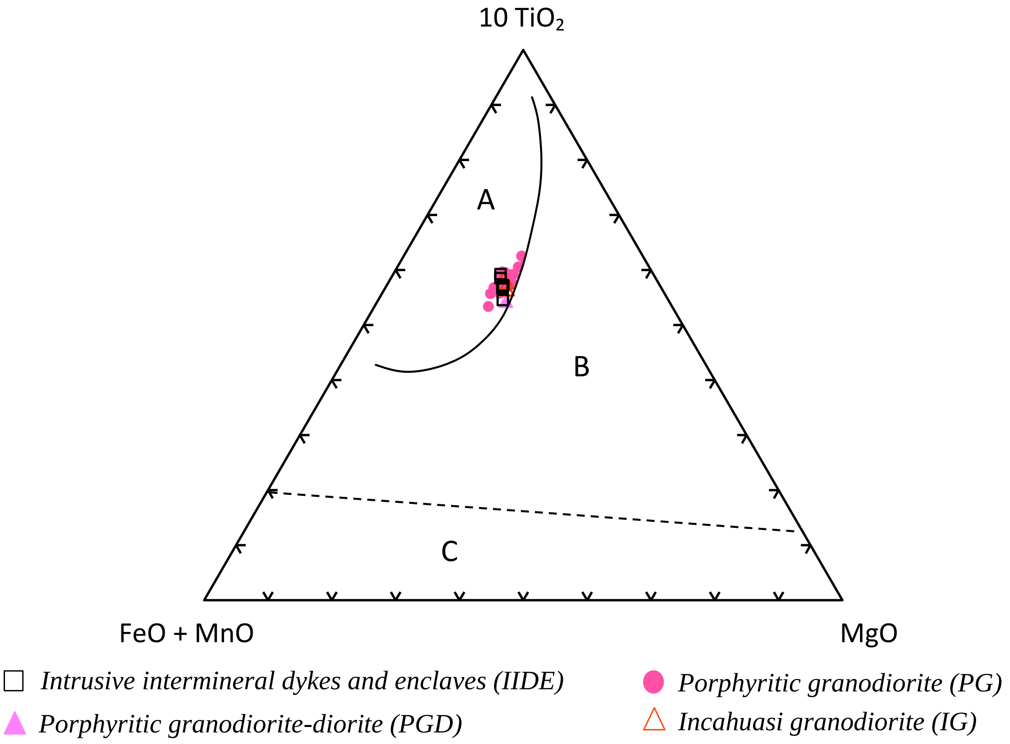

Figure 4.28. *Discrimination diagram of biotites for the PG, IG, IIDE and PGD of the Yanac system, Nachit et al. (2005). Fields correspond to A: primary biotites, B:reequilibrated biotites, C: neoformed biotites.*

In tectonic discrimination diagrams proposed by Abdel-Rahman (1994), analyses of primary biotites were plotted in the field of biotites from rocks of calc-alkaline suite (Fig. 4.29 a and b).

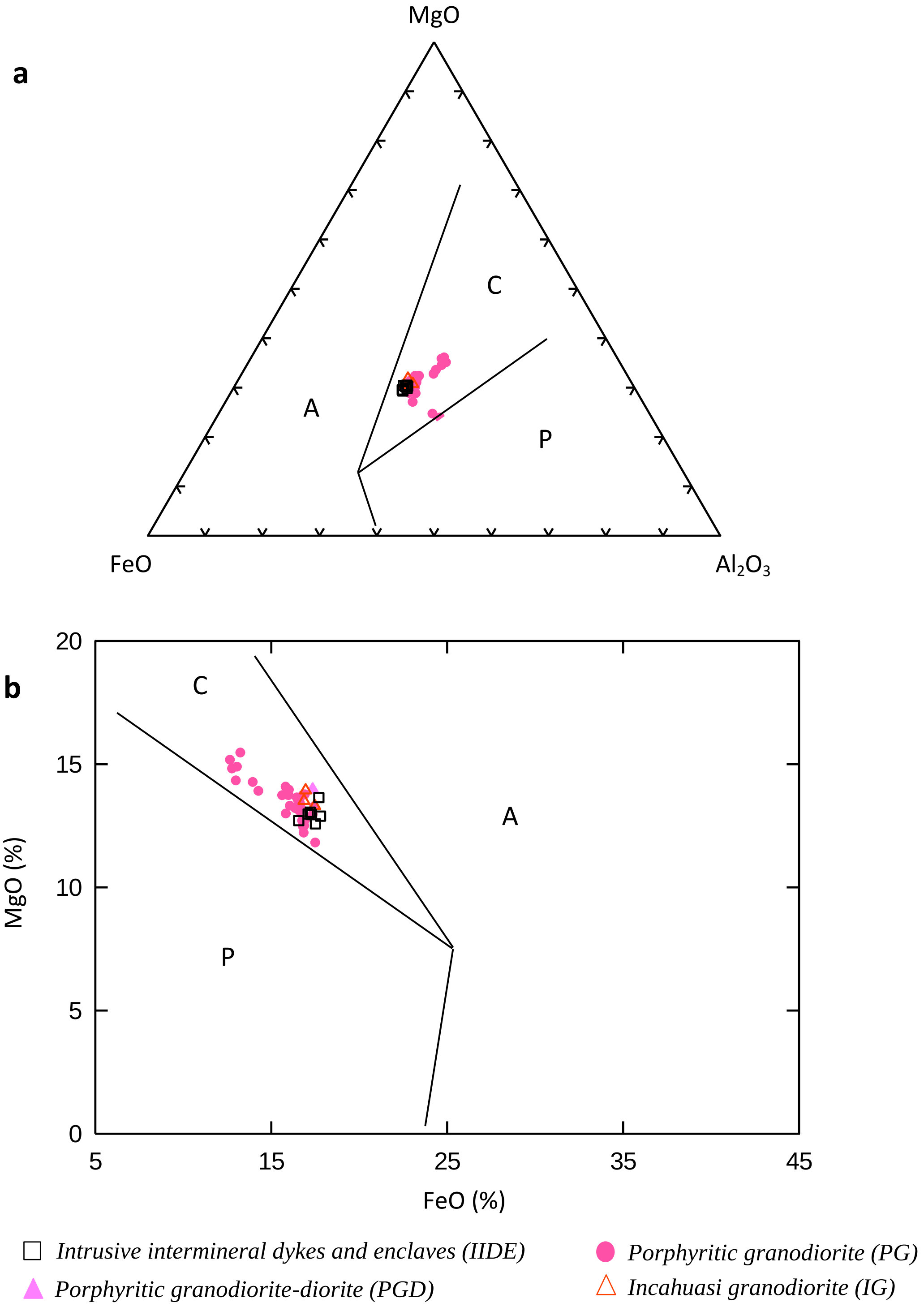

Figure 4.29. *Biotites of the PG, IG, IIDE and PGD from the Yanac system in the tectonic discrimination diagrams proposed by Abdel-Rahman (1994).* ***a.*** *MgO-FeO*-*Al_2O_3 *diagram,* ***b.*** *MgO-FeO* diagram. A=Alkaline granites, C=Calc-alkaline granites, P=Peraluminous granites.*

The simplified formula for the biotite is $I_2M_6T_8O_{20}A_4$, where I represents the interlayer site; M, the octahedral site, T, the tetrahedral site; O, oxygen, and A, anions. The average structural formula for the studied types of biotite, calculated for 22 oxygens equivalent, corresponds to:

Primary biotite for the porphyritic granodiorite (PG):
$(K_{1.41}, Na_{0.07}, Ba_{0.03})_{1,5}$ $(Mg_{3.00}, Fe_{2.00}, Al^{vi}_{0.23},Ti_{0.47})_{5.7}Si_{5.75}Al^{iv}_{2.23}O_{20}(OH_{3.82}F_{0.14}Cl_{0.04})$

Primary biotite for the regional intrusive Incahuasi (IG):
$(K_{1.55}, Na_{0.07}, Ba_{0.04})_{1.66}$ $(Mg_{3.03}, Fe_{2.14}, Al^{vi}_{0.08},Ti_{0.47})_{5.72}Si_{5.76}Al^{iv}_{2.24}O_{20}(OH_{3.93}F_{0.04}Cl_{0.03})$

Primary biotite for the porphyritic inter-minerals dykes and enclaves (IIDE):
$(K_{1.62}, Na_{0.07}, Ba_{0.04})_{1.73}$ $(Mg_{2.96}, Fe_{2.21}, Al^{vi}_{0.06},Ti_{0.47})_{5.7}Si_{5.72}Al^{iv}_{2.27}O_{20}(OH_{3.89}F_{0.06}Cl_{0.06})$

Primary biotite for the porphyritic granodiorite-diorite (PGD):
$(K_{1.03}, Na_{0.08}, Ba_{0.05})_{1.73}$ $(Mg_{3.16}, Fe_{2.20}, Al^{vi}_{0.17},Ti_{0.42})_{5.7}Si_{5.72}Al^{iv}_{2.28}O_{20}(OH_{3.82}F_{0.15}Cl_{0.03})$

4.9.2. Amphibole

The results of the analyses for amphibole are found in annex 3. The classification is based on the chemical contentes of the standard amphibole formula $A_{0-1}B_2{}^{VI}C_5{}^{IV}T_8O_{22}(OH)_2$ (Leake et al., 1997). All analyzed centers and borders of the amphibole grains belong to the calcic amphibole group. For amphibole classification, it was considered the following parameters: in the case of the PG, PGD, IG and IIDE, data have $(Ca+Na)_{M4} \geq 1.0$ and $Na_{M4} < 0.5$. The amphibole compositions have average values of $Ca_{M4} = 1.74$, $Si = 7.16$, $(Na+K)_A = 0.07$ and $Mg/(Mg+Fe^{2+}) = 0.93$ for the PG; $Ca_{M4} = 1.78$, $Si = 7.07$, $(Na+K)_A = 0.15$ and $Mg/(Mg+Fe^{2+}) = 0.85$ for the PGD; $Ca_{M4} = 1.81$, $Si = 7.01$, $(Na+K)_A = 0.27$ and $Mg/(Mg+Fe^{2+}) = 0.72$ for the IG; $Ca_{M4} = 1.78$, $Si = 6.91$, $(Na+K)_A = 0.31$ and $Mg/(Mg+Fe^{2+}) = 0.72$ for the IIDE, where structural formulae are:

Amphibole of the PG:
$K_{0.05}, Ca_{1.74}, Na_{0.26}[Mg_{3.36}Fe_{0.27}{}^{2+}Mn_{0.31}(Al_{0.003}Fe_{1.2}{}^{3+})]\ Si_{7.16}Al_{0.84}O_{22}(OH)_2$

Amphibole of the PGD:
$K_{0.07}, Ca_{1.78}, Na_{0.22}[Mg_{3.20}Fe_{0.56}{}^{2+}Mn_{0.19}(Al_{0.063}Fe_{0.98}{}^{3+})]\ Si_{7.07}Al_{0.93}O_{22}(OH)_2$

Amphibole of the IG:

$K_{0.08}$, $Ca_{1.81}$, $Na_{0.19}[Mg_{2.98}\,Fe_{1.14}^{2+}Mn_{0.08}Ti_{0.11}(Al_{0.15}Fe_{0.53}^{3+})]\,Si_{7.01}Al_{0.99}O_{22}(OH)_2$

Amphibole of the IIDE:

$K_{0.07}$, $Ca_{1.78}$, $Na_{0.22}[Mg_{2.89}Fe_{1.17}^{2+}Mn_{0.07}Ti_{0.14}(Al_{0.19}Fe_{0.53}^{3+})]\,Si_{6.91}Al_{1.09}O_{22}(OH)_2$

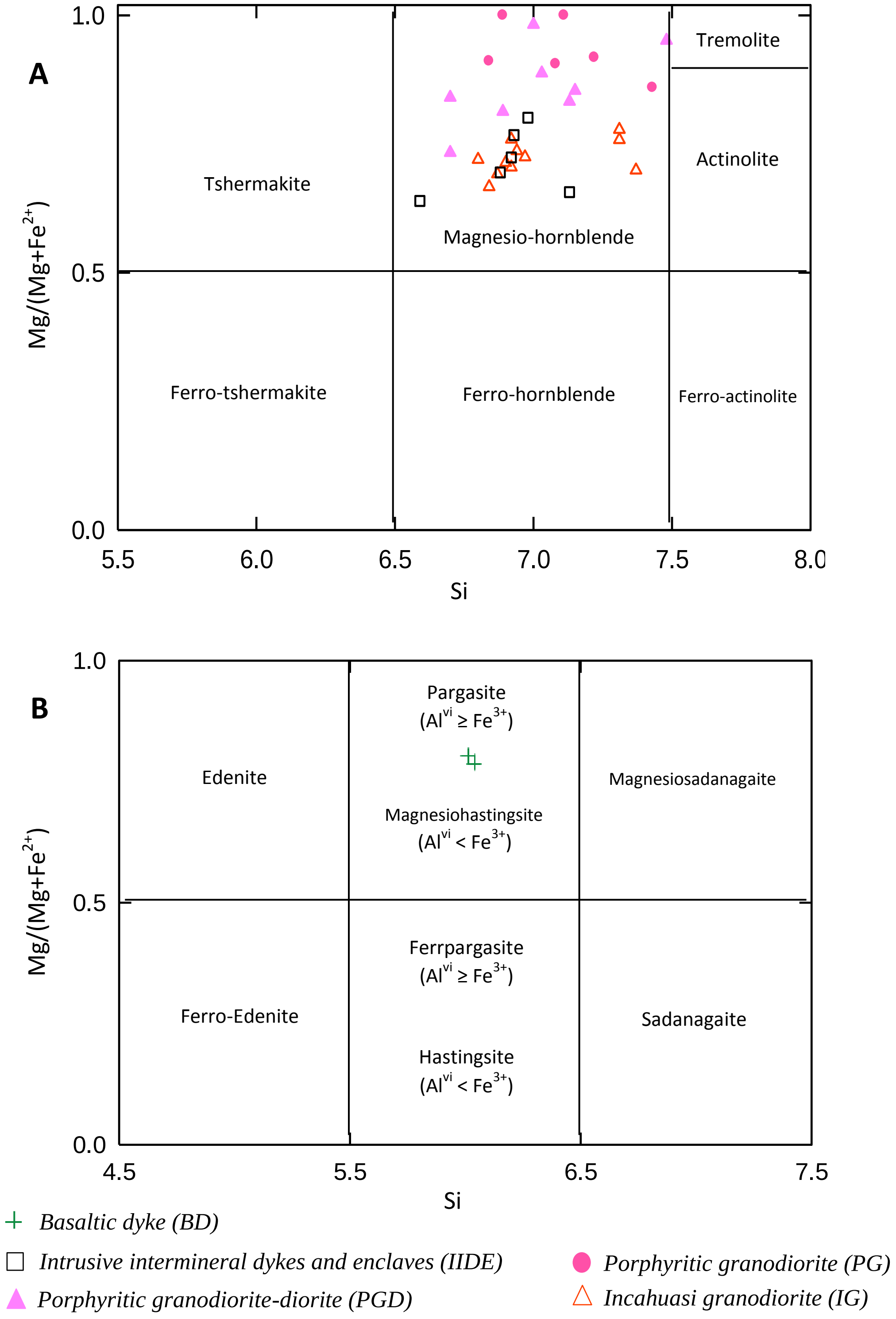

Figure 4.30. Classification diagram for the calcic amphipoles, according to *Leake et al (1997).* ***A.*** *$Ca_B \geq 1.50$, $(Na+K)_A \leq 0.5$ and $Ca_A < 0.5$.* ***B.*** *$Ca_B \geq 1.50$, $(Na+K)_A \geq 0.50$ and $Ti < 0.50$.*

Thus, for the PG, PGD, IG and IIDE, the data correspond to magnesio-hornblendes (Fig. 4.30).

In the case of the basaltic dyke, $(Ca+Na)_{M4} \geq 1{,}0$ and $Na_{M4} < 0.5$, $Ca_{M4} = 1.97$, Si = 6.014, $(Na+K)_A = 0.75$, $Mg/(Mg+Fe^{2+}) = 0.80$ e $Al^{vi} > Fe^{3+}$, so that, according to the nomenclature proposed by Leake *et al*. (1997), two analyses of amphibole in the core and border in the basaltic dyke (sample AY-42) correspond to pargasite, with the following structural formula:

Amphibole for the basaltic dyke:
$K_{0.06}, Ca_{2.01}, Na_{0.02}[Mg_{3.29}Fe_{0.85}^{2+}Mn_{0.01}Ti_{0.23}(Al_{0.38}Fe_{0.24}^{3+})]\ Si_{6.04}Al_{1.96}O_{22}(OH)_2$

4.11. DISCUSSION

4.11.1 Tectonic setting

Petrography and geochemistry in the Yanac prospect include the coarse-grained Incahuasi granodiorite of the coastal batholith, small stocks of a fine to medium-grained porphyritic granodiorite and a medium-grained porphyritic granodiorite-diorite , hydrothermal breccia, basalt and trachydacite post-mineral dykes. The presence of gabbroic diorite-diorite-monzodiorite inter-mineral dykes and enclaves in Yanac often suggests that enclaves derive from the dismemberment of such synplutonic basic dykes and shows that mixing between new basic magma and various stages of the Incahuasi granodiorite, porphyritic granodiorite and porphyritic granodiorite-diorite magmas was possible. These features are characteristic of the Coastal Batholith of Peru and analogous batholiths (Pitcher and Bussell, in Pitcher *et al.*, 1985, Pichowiak and Breitkreuz, 1984). They may indicate a mixing of a hot mafic melt injected into colder felsic magma.

The Incahuasi granodiorite, porphyritic granodiorite, porphyritic granodiorite-diorite, intrusive inter-mineral dykes and enclaves, all with magnesium-hornblende, have a sub-alkaline tendency in the calc-alkaline series. They are metaluminous, with ASI range = 0.87-0.89, SiO_2 = 54-66%, MgO/TiO_2 = 2.6-5.7, Al_2O_3 = 16.7-18.6 and $K_2O/Na_2O < 1$. They are petrographic and chemically consistent with I-type granites from volcanic arcs (table 4.3). The multielementar diagram of these rocks shows enrichment of the LILE in relation to the HFSE and significant negative anomalies of Nb and Ta, which is coherent with magmas associated with subduction zones in active continental margins (Winter, 2009). The enrichment of the LREE in relation to the HREE indicates the probable involvement of thick continental crust or subducted sediments with fluids (Winter, 2009). The presence of magnetite as accessory mineral (table 4.3) in the Incahuasi granodiorite, porphyritic granodiorite and porphyritic granodiorite-diorite is a characteristic parameter for determining these units within oxidized magmas (Ishihara, 1997). Primary biotite of the Incahuasi granodiorite, porphyritic granodiorite, porphyritic granodiorite-diorite and intrusive intermineral dykes and enclaves have Mg/(Mg+Fe) ratios varying between 0.54 and 0.68 and Al^{IV} between 2.06 and 2.38, composition compatible with biotites from granites of calc-alkaline orogenic suites (Abdel Rahman, 1994).

Compared chemical data between the post-mineral dykes and chemical signature of I and S magmas classification (table 4.3) of White and Chappell (1983), Clarke (1992) and Whalen (1985). The dyke with a basaltic composition and pargasite amphibole, is metaluminous, with ASI = 0.86, SiO_2 = 49.5%, MgO/TiO_2 = 4.6, Al_2O_3 = 18.3, and $K_2O/Na_2O < 1$. The basaltic dyke presents enrichment of the LILE in relation to the HFSE, significant negative anomalies of Nb and Ta and enrichment of the LREE in relation to the HREE, which are coherent with magmas associated with subduction zones in active continental margins and indicates the probable involvement of thick continental crust or subducted sediments with fluids (Winter, 2009). The trachydacite dyke is weak peraluminous, with ASI = 1.0, SiO_2 = 68.3%, MgO/TiO_2 = 1.3, Al_2O_3 = 15.2, and $K_2O/Na_2O > 1$. The multielementar diagram and REE with pronounced negative Eu anomaly of this rock (Figs. 4.20 and 4.21), have a different geochemical signature comparing with the Incahuasi granodiorite, porphyritic granodiorite, porphyritic granodiorite-diorite, intermineral dykes and enclaves and the basaltic dyke. The trachydacite dyke is interpreted probably as an S-type magma (table 4.3). The basaltic and trackydacite dykes are emplaced after the intrusions of the Incahuasi granodiorite, porphyritic granodiorite and porphyritic granodiorite-diorite, with unknown ages and may represent later episodes in the evolution of the coastal batholith.

The U-Pb ages obtained from zircon of the Incahuasi granodiorite (70.6 ± 1.0 Ma.), porphyritic granodiorite (71.0 ± 1.0 Ma.) and porphyritic granodiorite-diorite (67.75 ± 0.80 Ma.) were interpreted as the crystallization age of the rocks. These ages, which are younger ages for the Arequipa segment of the coastal batholith (~106 to 80 Ma.), confirm that the coastal batholith has an Upper Cretaceous age (Beckinsale *et al*., 1985; Moore and Agar, 1985; Mukasa and Tilton, 1985a; Pitcher, 1985; Mukasa, 1986a).

Table 4.3. *Comparison table of the I and S type magmas in Yanac, following a S-I-A-M magmas classification of White and Chappell (1983), Clarke (1992) and Whalen (1985).*

Magma Type	**SiO2**	**K_2O/Na_2O**	**Ca, Sr**	**Al/(Ca+Na+K) molar**	**Cr, Ni**	**Miscellaneous**
I Magma	**54-76%**	**Low**	**High in mafic rocks**	**Low, metaluminous to weakly peraluminous**	**Low**	**High LILE /HFSE, medium Rb, Th, U; amphibole, magnetite**
Incahuasi granodiorite (IG)	63.2-63.9	0.65-0.7	CaO: 4.91-4.92, Sr: 530-551	Metaluminous	Cr: <20-30, Ni: 2.2	Moderate-high LILE/HFSE, Rb: 59.2-62, Th: 6.1-7.1, U: 1.4-2, amphibole, magnetite
Porphyritc granodiorite (PG)	65.95	0.6	CaO: 4.6, Sr: 617.4	Metaluminous	Cr: 40, Ni: 1.9	Moderate-high LILE/HFSE, Rb: 61.4, Th: 5.6, U: 1.3, amphibole, magnetite
Porphyritic granodiorite-diorite (PGD)	59.7-65.1	0.5-0.7	CaO: 4.6-5.9, Sr: 508-614	Metaluminous	Cr: <20-40, Ni: 1.9-2.2	Moderate-high LILE/HFSE, Rb: 41.2-61.9, Th: 4.4-5.8, U: 1.1-1.8, amphibole, magnetite
Intrusive inter-mineral dykes and enclaves (IIDE)	52.4-61.2	0.3-0.5	CaO: 5.32-7.27, Sr: 501-569	Metaluminous	Cr: <20-50, Ni: 1.9-7.5	Moderate-high LILE/HFSE, Rb: 36.9-50.5, Th: 3.3-6.9, U: 0.7-2.2, amphibole
Basaltic dyke (BD)	49.5	0.4	CaO: 8.24, Sr: 514	Metaluminous	Cr: <20, Ni: 4.5	Moderate LILE/HFSE, Rb: 50.7, Th: 1.8, U: 0.6, amphibole
S Magma	**65-74%**	**High**	**Low**	**High, peraluminous**	**High**	**Variable LILE/HFSE, High Rb, Th, U; biotite, cordierite, Al-silicates, garnet, ilmenite**
Trachydacite dyke (TD)	68.3	1.4	CaO: 1.38, Sr: 177.8	Weak peraluminous	Cr: 20, Ni: 0.9	Moderate LILE/HFSE, Rb: 183, Th: 21.5, U: 6

4.11.2. Hydrothermal alteration and mineralization

Grouping the samples with similar characteristics of geology, alteration and mineralization, were possible generate a hydrothermal alteration map in the Yanac prospect, associated mostly to the stockwork structures and the hydrothermal breccia (Fig. 4.31).

Based on the mineralogical assemblage present in Yanac, the observed veinlets were divided in A, B and C phases with some of these groups containing some subtypes veinlets. A and B phases were compared with some of the alteration types described by

Seedorff et al., 2005 (table 4.4), and although, all the mineralogical associations do not coincide, it was a good way to determine through a comparison, a propylitic alteration for the event A and a phyllic alteration for the phase B. The phase C, characterized by laumontite-quartz-adularia association, is not comparable with any alteration assemblages described by Seedorff et al. (2005). Phase C cuts phase B veinlets. Phase C is similar to mineralogical alteration assemblage found in low sulphidation epithermal-type deposits (Camprubi et al., 2003).

Propylitic alteration (Fig. 4.3: samples AY-04, AY-03, AY-02, AY-01, AY-05 and AY-12, AY-13, AY-22 and AY-11, Fig. 4.31) consists of minerals contained within fractures and weak selectively pervasive type of alteration. It has biotite and hornblende altered to chlorite, and albite, epidote and calcite formed over plagioclase. Sometimes, sericite may also form. Chemical reactions indicate an environment dominated by a near-neutral pH and reducing conditions (Barnes, 1997). Pyrite, ±chacopyrite and ±molybdenite contents in the veinlets of this alteration are typically low.

The phyllic alteration occurred in two intensities. The first, a weak phyllic alteration (Fig. 4.3, samples: AY-29, AY-40, AY-09, AY-24, AY-26, AY-10, AY-27, AY-23A, AY-23B, AY-23B1, AY-23D, AY-23E, AY-17, table 4.2: weak hydrothermal alteration B, Fig. 4.31), is characterized by the assemblage of the B1, B2, B3 and B4 subtype veinlets (table 4.4). It is interpreted as a transitional stage from an incipient to a true phyllic alteration in a strong stockwork, which is in accordance to Camus (2003), formed possibly by temperature decrease and incorporation of meteoric water flows into the system, whose distinctive features are the thin halos of sericite along the veinlets. Also, the Hydrothermal breccia could be related to this event for their quartz-sericite±albite±pyrite±chalcopyrite±molybdenite alteration (table 4.1). The second phyllic alteration is a stronger phyllic alteration (Fig. 4.3, samples: AY-15 and from AY-41A to AY-41D, table 4.2: strong hydrothermal alteration B, Fig. 4.31), characterized by the assemblage of the B5 subtype veinlets (table 4.4). The original texture of the altered rocks was almost completely destroyed. Strong phyllic alteration is associated with appreciable quantities of fine-grained, disseminated pyrite which is directly associated with the alteration event in substitution of former mafic minerals. Outside this alteration, probable mafic minerals are generally converted to chlorite for some distance, and plagioclase is typically partially replaced by sericite with relict albite. There is also chlorite formation inside a weak phyllic alteration zone (Fig. 4.3, B3 subtype veinlets, table 4.1: samples AY-24, AY-26 and AY-27, Fig. 4.31).

Comparing geochemical data between the porphyritic granodiorite and the strong phyllic alteration (table 4.2: strong hydrothermal alteration B), the altered rock has a higher amount of SiO_2, K_2O, by the presence of more silica and sericite, and smaller amount of CaO, Na_2O, MgO and Fe_2O_3, by the hydrothermal alteration of the ferromagnesian and plagioclase primary minerals. The amounts of Large Ion Lithophile Elements (LILE) are high (Fig. 4.21, table 4.2), whereas all high field strength elements (HFSEs), except Hf and Zr, have low concentration (Fig. 4.21, table 4.2) during sericitization. Moreover, all the rare earth elements (REEs) are low in the sericitic samples, and it seems that the LREEs have stronger depletion than the HREEs (Fig. 4.20, table 4.2). Weak and strong phyllic alteration, according to Seedorff *et al*. (2005), represent progressively more intense hydrogen metasomatism and base-cation leaching.

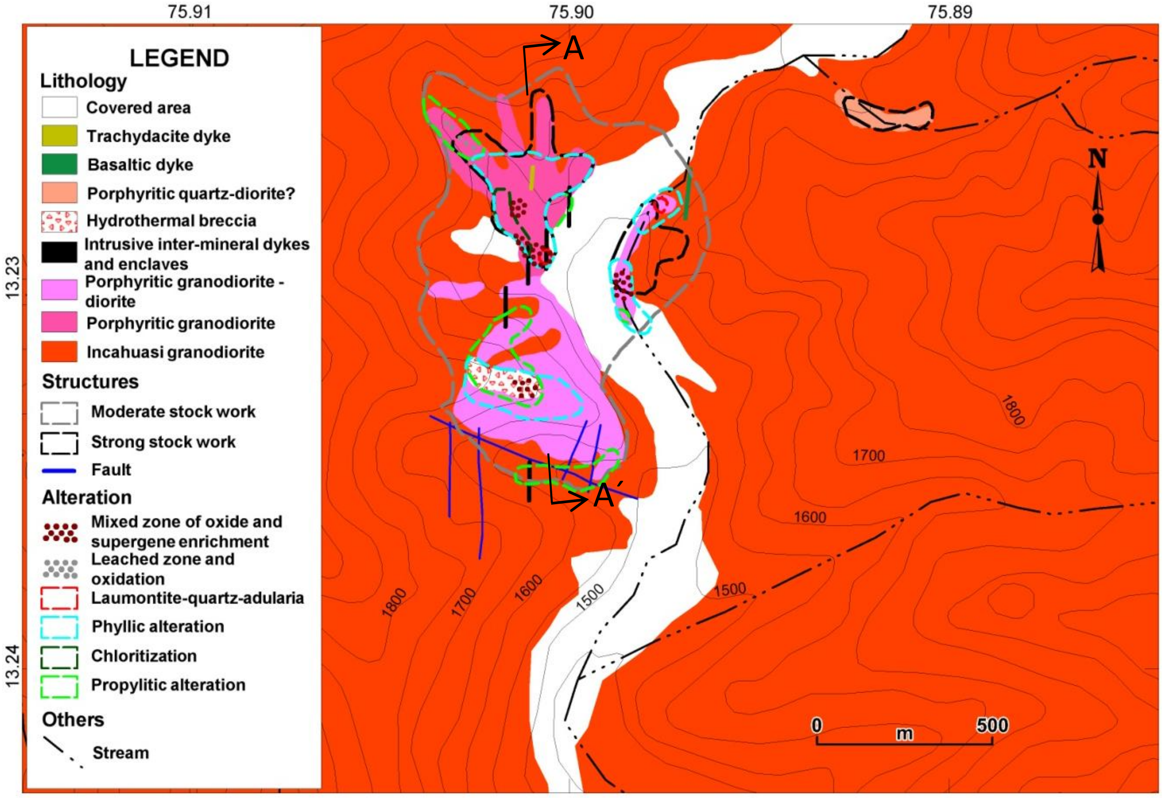

Figure 4.31. Hydrothermal alteration map of the Yanac prospect (modified of Estrella Gold Peru S.A.C., 2011).

Table 4.4. *Comparison table of the hydrothermal alteration A and B in Yanac with propylitic and phyllic alteration types of Seedorff et al.(2005).*

Alteration type (synonyms) and subtype veinlets	Silicates and Al-rich minerals (±Quartz)	Key sulfide-oxide assemblages and other opaque and Ti minerals	Carbonates, fluories, sulfates, phosphates	Commonly associated veinlet types
Propylitic	**Albite, sericite-illite, montmorillonite, chlorite, epidote, (zoisite, clinozoisite, zeolite, actinolite); relict K-feldspar, (biotite), zircon**	**(Bornite, chalcopyrite, pyrite, pyrrhotite, molybdenite, sphalerite, galena, tennantite, tetrahedrite, hematite, relict magnetite, titanite, rutile**	**Calcite or carbonate of undetermined composition, ankerite; ± relict apatite**	**Calcite, epidote, hematite, and chlorite veins with illite-defined propylitic envelopes**
A1	Chlorite-albite	Pyrite±chalcopyrite	Carbonates	Quartz-chlorite-albite-carbonates-pyrite±chalcopyrite .
A2		Pyrite±chalcopyrite±molybdenite		Pyrite-quartz±chalcopyrite±molybdenite.
A3	K-feldspar-epidote-chlorite	Pyrite±chalcopyrite		K-feldspar-epidote-chlorite-pyrite±chalcopyrite .
Sericitic (phyllic, quartz-sericite-pyrite)	**Sericite, (albite, topaz, tourmiline), chlorite, (epidote, clinozoisite)**	**Chalcopyrite+pyrite+molybdenite; pyrite; (pyrrhotite, bornite), tennantite, (arsenopyrite), sphalerite, galena, stannite, bismuthinite, cassiterite, magnetite, hematite, rutile**	**(Calcite), fluorite, (anhydrite), apatite**	**Veinlets with sericitic envelops ("D")**
B1	Sericite-albite	Pyrite-chalcopyrite-molybdenite		Quartz-pyrite-chalcopyrite-molybdenite with thin alteration halo of sericite-albite.
B2	Sericite-albite±K-feldspar	Pyrite-molybdenite-chalcopyrite		Quartz-sericite and albite halo with a pyrite-molybdenite-chalcopyrite±K-feldspar suture.
B3	Sericite-chlorite	Pyrite±chalcopyrite		Veinlets are green and composed by sericite-chlorite-quartz-pyrite±chalcopyrite assemblage .
B4	Sericite	Pyrite		Quartz-pyrite with a very pronounced sericite halo reaching up to 2 cm thick.
B5	Sericite±albite	Pyrite		Quartz-sericite-pyrite±albite that completely destroy the original texture of the porphyritic granodiorite.

Sometimes a probably progressive thermal decline of the systems combined with synmineral paleosurface degradation results in the characteristic overprinting (telescoping) and partial to total reconstitution of older by younger alteration types (Sillitoe, 2010) are present, like in the propylitic and phyllic alteration zones of AY-37, AY-38, AY-08, and AY-19, as well as, in the chloritization and phyllic alteration zone of the AY-27, AY-26 and AY-24 (Fig. 4.3, Fig. 4.31). In hydrothermal alteration C (AY-23C and AY-16 sample veins, Fig. 4.3, Fig. 4.31), the laumontite-quartz-adularia veins telescoping in a weak phyllic alteration zone could probably be interpreted as the rootsof a low sulphidation epithermal-type alteration assemblage that was eroded, indicating that the system could be representing a transition between Yanac and an eroded epithermal-type deposit.

Around a regional zone of Yanac, other occurrences emplaced around the same geologic time exist and were reported (Rivera et al., 2008) with potassic central zone with telescoping phyllic alteration surrounded by propylitic alteration and silicification, as in the Pucacorral Sur deposit (82 Ma.). Also, a potassic alteration center, surrounded by phyllic and propylitic alterations was described for the Puquio deposit (76 Ma.), and a phyllic with propylitic alterations for the Zafranal deposit (80 Ma.). Then, the types of assemblages determined to Yanac, form part of a group of ocurrences with a similar alteration type in southern Peru.

Geochemically, copper and molybdenum contents vary according to the type of alteration (Table 4.2). Copper increases from an average of 68 ppm for porphyritic granodiorite and porphyritic granodiorite-diorite to an average of 1631 ppm Cu for the weak phyllic alteration with strong stockwork and 4513 ppm for the hydrothermal breccia. Data obtained for the strong phyllic alteration provided lower than 343 ppm Cu. The average values of Mo are 2 ppm for the porphyritic granodiorite and porphyritic granodiorite-diorite, 35 ppm for the strong phyllic alteration, 40 ppm for the weak phyllic alteration and 240 ppm for the hydrothermal breccia.

Geological and geochemical data from Yanac (Fig. 4.32) show that in the weak phyllic alteration, including the hydrothermal breccia, primary sulfide minerals (chalcopyrite-pyrite), without later enrichment by supergene processes, are strongly zoned from central, with more chalcopyrite-rich veins, cutting a probably deeper older potassic alteration zone by the presence of incipient K-feldspar in the B2 subtype veinlets (table 4.4), to outward, with more pyrite-rich veinlets, interpreted to be part of a propylitic and strong phyllic alteration. This zonation is evidenced by the alteration itself and by the Cu mineralization map of Yanac (Fig. 4.32). Molybdenum shows the same behavior: it is more enriched in the weak phyllic alteration and decreases towards the propylitic and strong phyllic alteration (Fig. 4.33).

Gold content in the rocks of the Yanac prospect are low: average values of 0.5 ppb in the porphyritic granodiorite and porphyritic granodiorite-diorite to 7.2 ppb and 9.1 ppb in the weak phyllic alteration, and values of 42.4 ppb and 33.1 ppb in the strong phyllic alteration (table 4.2, Fig. 4.34).

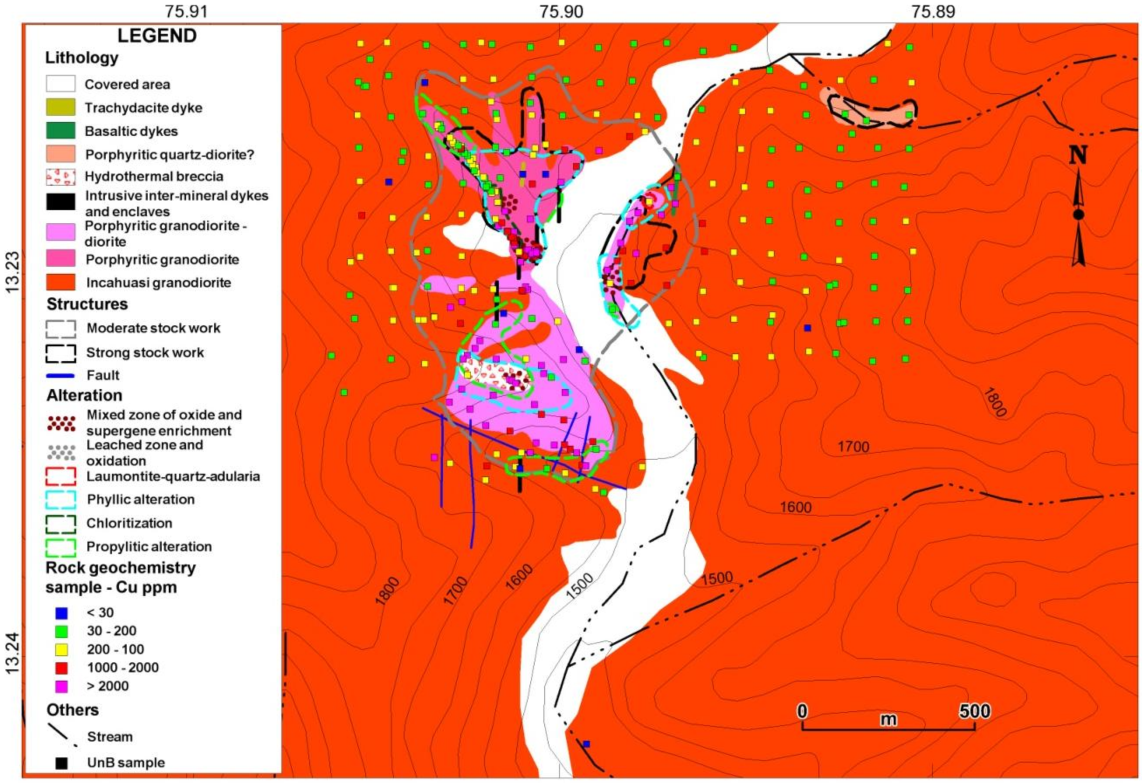

__Figure 4.32.__ Geochemical map of the Yanac prospect showing the distribution of Cu (Geochemical analyses of Cu data mainly used from Estrella Gold Peru S.A.C. and minor for sampling made in this research).

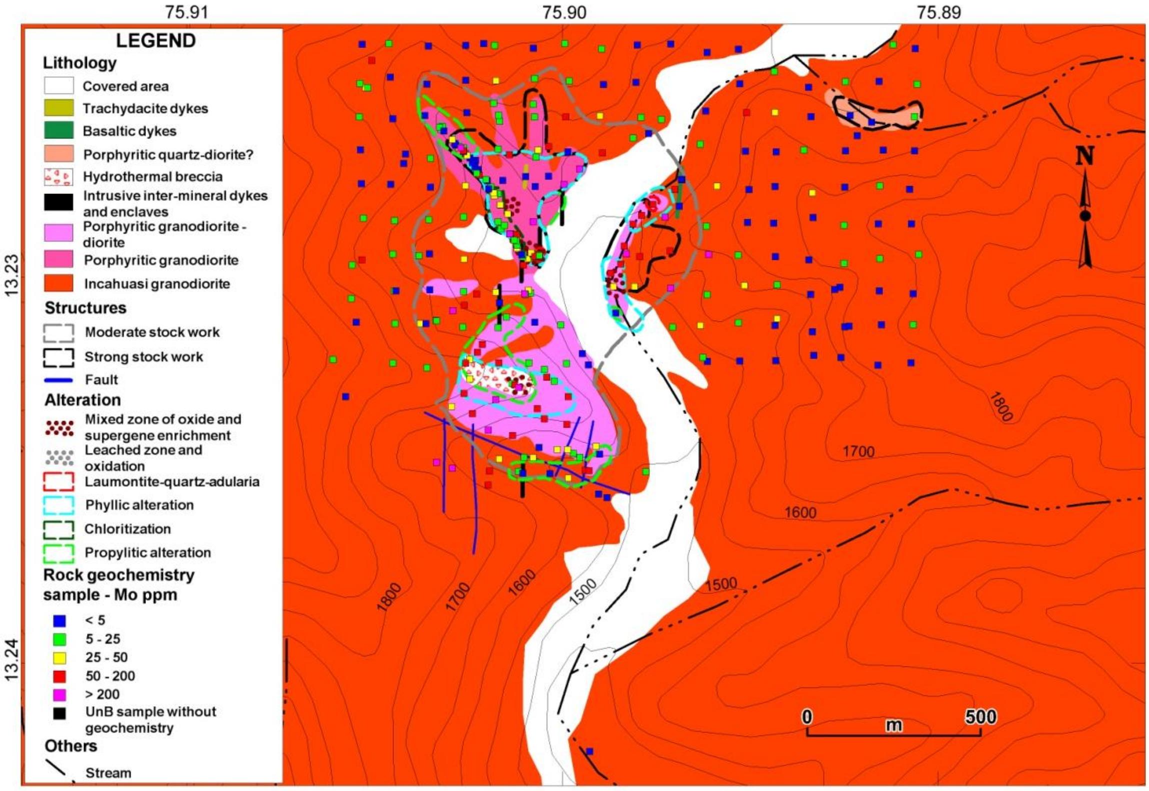

(Geochemical analyses of Mo data mainly used from Estrella Gold Peru S.A.C. and minor for sampling made in this research).

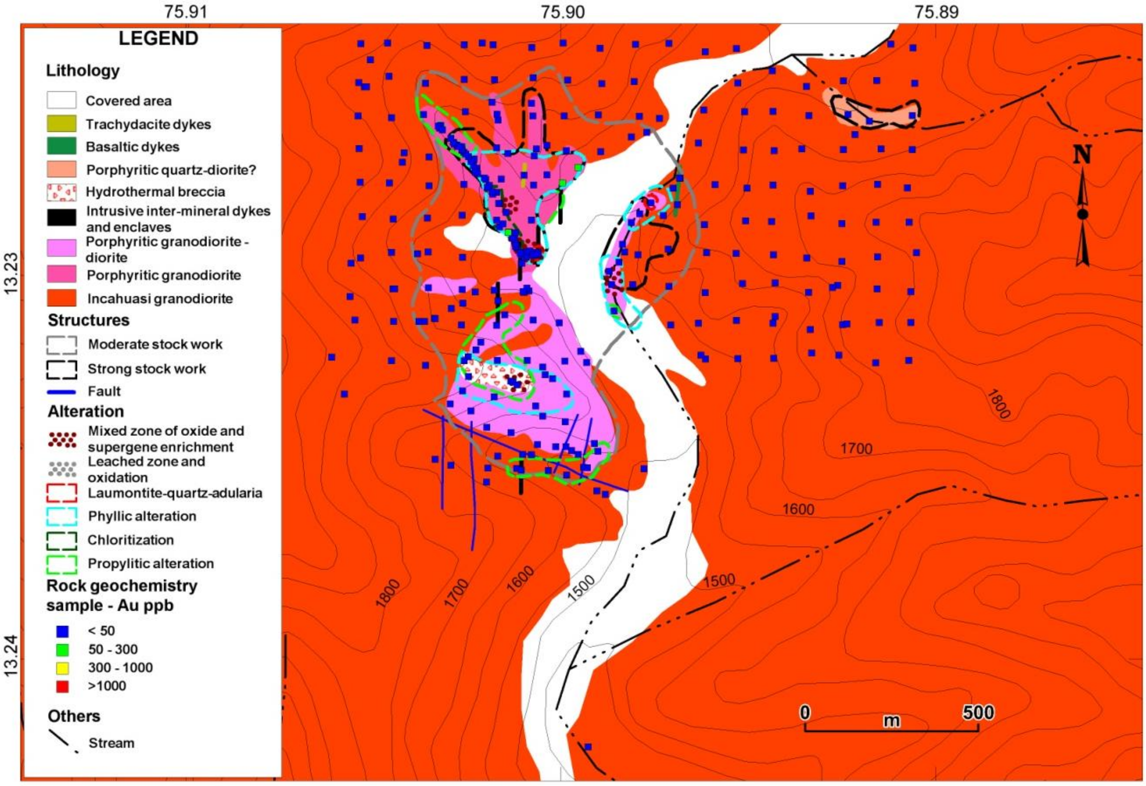

Figure 4.34. *Geochemical map of the Yanac prospect showing the distribution of Au (Geochemical analyses of Au data mainly used from Estrella Gold Peru S.A.C. and minor for sampling made in this research).*

Then, comparing the type of mineralization of Yanac with other occurrences at the southern Peru with similar ages, as Cu-Mo Pucacorral Sur deposit, with 82 Ma., Cu-Mo Puquio deposit, with 76 Ma., and Cu-Au Zafranal mineralization with 80 Ma. (Rivera *et al*., 2008), the mineralogical characteristics are similar: Yanac presents a Cu-Mo mineralization, related to a higher content of chalcopyrite in a weak phyllic hydrothermal alteration and strong stockwork zone.

4.11.3. Magma and metal genesis and evolution

For the porphyritic granodiorite and porphyritic granodiorite-diorite, εHf(T) data revealed values from -0.28 to +6.65. It means that Lu-Hf data have a mantle-derived magma, with low crustal contribution (Kinny and Maas, 2003). Comparing with the isotopic studies made for the coastal region and the lower Pacific slope of the Andes of central Peru, these results are in agreement with the contribution of recycled oceanic sediments in the genesis of Andean calc-alkaline magmas, although in many cases the evidence is obscured by interaction between the subcontinental mantle source with the continental crust (Soler and Rotach-Toulhoat, 1990).

All the different lithological units at Yanac have characteristics of I-type magmas (table 4.3), and are considered to have the same source, except for the trachydacite dyke, which presents different geochemical signature and S-type magma, with a probable supracrustal sedimentary source (table 4.3).

Although it is not possible to establish the source of the hydrothermal fluids, it is considered here the hypothesis that these were originated together with the magmas of the coastal batholith and all the processes involved to migrate up into the crust above, according the model of Wilkinson (2013). These magmas probably generated the porphyritic granodiorite-diorite, possible source of the alteration and mineralization at Yanac.

The obtained data suggest that the porphyritic granodiorite-diorite played an important role for the generation of hydrothermal solutions and Cu and Mo enrichment. The evidences are its later emplacement in relation with the others intrusives, the spatial position of the hydrothermal breccia, which is located between the Incahuasi granodiorite and the porphyritic granodiorite-diorite, the presence of moderate to pervasive stockwork structures over it and higher Cu and Mo values related to the weak phyllic alteration around the unit.

Table 4.5, contains a summary of the main characteristics of Yanac, in comparison with other types of deposits present in the district. Compared with the deposits classified as porphyry copper, which are spatial and temporally linked to subduction zones and copper provinces, like in the Andes (Sillitoe and Perello, 2005), Yanac has similarities, as the presence of multiple I-type stocks, the style of mineralization, the host rock, the metals and some of the hydrothermal alteration styles. Moreover, comparing with other deposits, the style of mineralization are similar to the epithermal deposits of high sulphidation and the style of mineralization and hydrothermal alteration, as the presence of adularia, are also found in epithermal deposits of low sulphidation.

The tectonic interpretation of the batholith and the rocks formed during the same period at Yanac, based on geochronological and geochemical data, indicate an environment of passive-active continental margin , developed over fairly moderate crust during relatively steep subduction (Middle Jurassic – Paleocene), with metallogenic implications for formation mostly of Fe oxide-Cu-Au deposits, manto-type Cu and subordinate porphyry Cu types, as indicated by Skewes and Stern (1994) and Sillitoe (1998). However, geological, geochronological and petrological characteristics obtained at Yanac indicate that a more compressive magmatic arc environment with a lower subduction angle prevailed during the upper Cretaceous longer than previously suggested, due to the majority presence of porphyry Cu mineralization in this metallogenic belt.

Table 4.5. *Comparison between the Yanac prospect and different deposit models present in southern Peru.*

Deposit	**Yanac**	**Porphyry copper deposit**	**IOCG deposit**	**Epithermal of high sulphidation**	**Epithermal of low sulphidation**
Style of mineralization	Stockwork, disseminated, hydrothermal breccia	Stockwork, disseminated, presence of hydrothermal breccias, or conttroled by fractures	Veins or breccias, stockwork, mantles	Dominated by disseminated mineralization, the replacements are frequent, rare stockwork, veins generally very rare	Veins, stockwork, veins with symmetrical banding
Host rock	Porphyritic granodiorite, I-type, calc-alkaline	Calc-alkaline to alkaline, I-type, oxidized magmas of the magnetite serie, porphyritic texture	Calc-alkaline, monzonitic, oxidized magmas of the magnetite serie	Subaereal volcanic rocks, acidic to intermediate rocks (essentially andesite-rhyodacite)	Volcanic rocks, typical rhyodacite
Age of the deposit	67.75±0.80 Ma., upper Cretaceous	Ages for southern Peru from th early Cretaceous to early Pliocene	In southern Peru only present in the early Cretaceous	Generally, Tertiary or more recent, examples for Neoproterozoic and Archean	Generally, Tertiary or more recent, examples for Neoproterozoic and Archean
Metals	Cu±Mo	Cu±Mo±Au, Mo, W ou Sn	Cu-Au-(Ag-Co-U-REE-Ba-F)	Au-Cu, Ag-Pb	Au (Ag, Pb-Zn), Ag-Pb-Zn(Au)
Hydrothermal alteration minerals	Phyllic, propylitic, presence of adularia	Potassic, Phyllic, propylitic, argillic	Extensive metasomatism Na-Ca-Cl	Advanced argillic to argillic (±sericite), extensive hypogene alunite, major hypogene kaolinite, no adularia	Propylitic to argillic, supergene alunite, occasional kaolinite, abundant adularia
Metalic mineral	Pyrite, chalcopyrite, molybdenite	Mostly pyrite, chalcopyrite, molybdenite	Abundant magnetite and/or hematite	Pyrite, electrum, sphalerite, galena (arsenopyrite)	Pyrite, enargite, chalcopyrite, tennantite, covellite
Depth		1-6 Km	Wide range of crustal depths	0.5-2 Km	0-1 Km
known deposits		Cerro Verde (Peru), Toquepala (Peru), Chuquicamata (Chile)	Raul Condestable (Peru), Mina Justa (Peru), Candelaria-Punta del cobre (Chile)	Julcani (Peru), Castrovirreyna (Peru)	Arcata (Peru), Orcopampa (Peru)
References	This dissertation, Estrella Gold Peru (2011)	Seedorff (2005), Camus (2003), Sillitoe and Perelló (2005)	Sillitoe and Perelló, 2005	Camprubi A. *et al*., 2003	Camprubi A. *et al*., 2003

The proposed metallogenic model for Yanac (Fig. 4.35) involves the generation of deep magmas in an environment of oblique subduction, such as prevailed in the central coastal region of the Peruvian Andes (Soler and Rotach-Toulhoat, 1990), probably in the lithospheric mantle, which could be the source of magmas and metals.

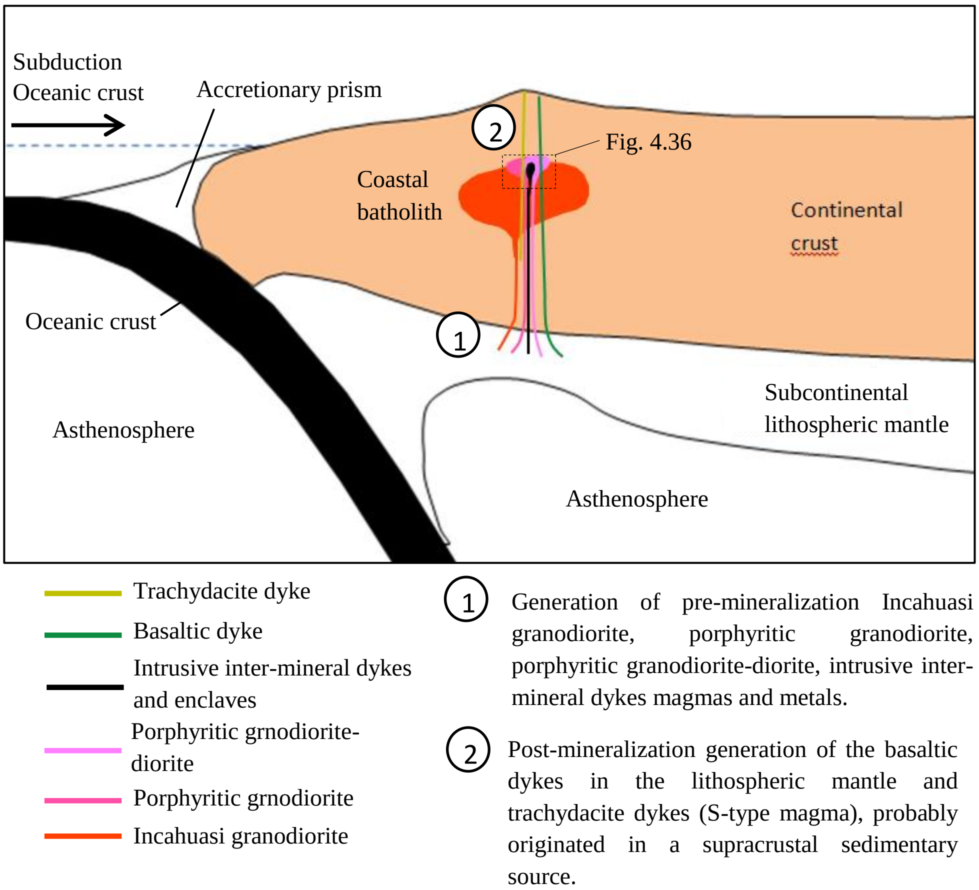

① Generation of pre-mineralization Incahuasi granodiorite, porphyritic granodiorite, porphyritic granodiorite-diorite, intrusive inter-mineral dykes magmas and metals.

② Post-mineralization generation of the basaltic dykes in the lithospheric mantle and trachydacite dykes (S-type magma), probably originated in a supracrustal sedimentary source.

Figure 4.35. *Magmatic and Metallogenic evolution proposed for the generation of copper and molybdenum in Yanac.*

The following evolution sequence is proposed for Yanac (Fig. 4.36).

During the lower to upper Cretaceous, marine sedimentary and volcanic sequences were deposited in the Cañete basin of the western Peruvian trough (Fig. 4.36a; Wilson, 1963; Cobbing, 1985; Jaillard *et al.*, 1990). Later, during the upper Cretaceous, the emplacement of the various intrusive-hypabyssal pulses started, including contemporary intrusive intermineral dykes. The Upper Cretaceous was characterized by a rising of the sedimentary and volcanic sequences during the Peruvian Phase (Palacios *et al.*, 1995), and by emplacement of large portions of the coastal batholith in the form of pulses that continued until the lower Tertiary. First, the Incahuasi granodiorite was emplaced at 70.6 ± 1.0 Ma, constituting the host rock of the Yanac porphyry (Fig. 4.36 b). Later, by the observed in the geological fieldwork, although with an inconsiderable slightly higher age of 71.0 ± 1.0 Ma. within an error of 1 Ma., occurred the intrusion of the porphyritic granodiorite (Fig. 4.36 b). The porphyritic granodiorite-diorite is much younger (67.75 ± 0.80 Ma.) and is probably responsible for the hydrothermal fluids and generation of stockwork structures, brecciation, hypogene alteration and mineralization (Fig. 4.36 c).

Cenozoic uplift and erosion of tectonic blocks exerts a powerful influence on supergene oxidation and enrichment in the central Andes since at least 42 Ma. (Sillitoe and Perello, 2005). From the Eocene to the Miocene-Pliocene, some compressive phases occurred with uplift and downlift, denominated Inca and Quechua Phases (Palacios *et al*., 1995). At Yanac, this event gave rise to the formation of jarosite, goethite, hematite, manganese oxides, green oxides ores of copper and rare coquimbite and aluminocopiapite. Also, a mixed mineralized zone with oxides and supergenic enrichment is characterized by secondary covellite around chalcopyrite, amorphous black and green copper oxides, limonites and diaspora. At this time, processes of erosion modeled the relief until the current view. Contemporaneously, subsequent phases of basaltic and trachydacite post-mineral dykes were probably emplaced (Fig. 4.36 d, e).

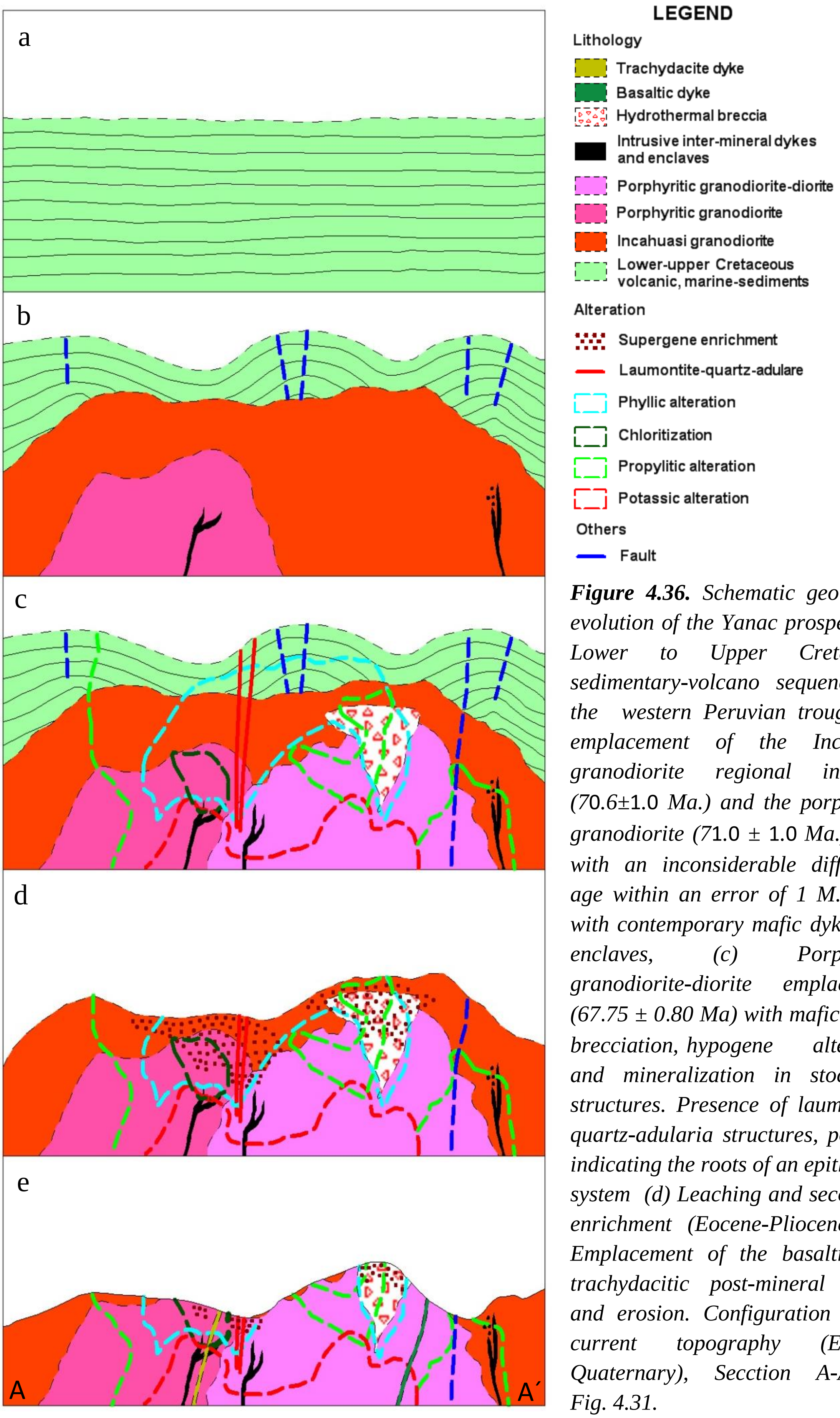

Figure 4.36. *Schematic geological evolution of the Yanac prospect, (a) Lower to Upper Cretaceous sedimentary-volcano sequences of the western Peruvian trough, (b) emplacement of the Incahuasi granodiorite regional intrusive (70.6±1.0 Ma.) and the porphyritic granodiorite (71.0 ± 1.0 Ma.), both with an inconsiderable difference age within an error of 1 M.a. and with contemporary mafic dykes and enclaves, (c) Porphyritic granodiorite-diorite emplacement (67.75 ± 0.80 Ma) with mafic dykes, brecciation, hypogene alteration and mineralization in stockwork structures. Presence of laumontite-quartz-adularia structures, possibly indicating the roots of an epithermal system (d) Leaching and secondary enrichment (Eocene-Pliocene), (e) Emplacement of the basaltic and trachydacitic post-mineral dykes, and erosion. Configuration of the current topography (Eocene-Quaternary), Secction A-A´from Fig. 4.31.*

4.12. CONCLUSIONS

The host rock of the Yanac prospect is a granodiorite with U/Pb zircon age of 70.6 ± 1.0 Ma, with undeformed, phaneritic, hypidiomorphic and equigranular medium to coarse-grained texture, belonging to the Incahuasi superunit of the coastal batholith. By relative emplacement observed in geological fieldwork, this unit is intruded by small stocks: first, by a fine to medium-grained porphyritic granodiorite of U/Pb zircon age of 71.0 ± 1.0 Ma., slightly higher than the previous lithological unit, but both within an inconsiderable error, lesser than 1 M.a. The porphyritic granodiorite is composed by plagioclase, quartz, K-feldspar, biotite and amphibole phenocrysts enveloped by a microcrystalline matrix mainly of quartz and plagioclase; and second by a medium to coarse-grained porphyritic granodiorite-diorite wit U/Pb zircon age of 67.75 ± 0.80 Ma, composed of plagioclase, quartz, K-feldspar, amphibole and biotite phenocrysts in a microcrystalline quartz and plagioclase matrix.

Gabbroic diorite-diorite-monzodiorite intermineral dykes and enclaves are contemporaneous with the Incahuasi granodiorite, porphyritic granodiorite and porphyritic granodiorite-diorite units, and together with the previous more felsic magmas probably produce mixing processes. Later, basaltic and trachydacitic dykes with volcanic texture cut the emplaced rocks.

The Incahuasi granodiorite, porphyritic granodiorite, porphyritic granodiorite-diorite, intrusive inter-mineral dykes, enclaves, and post-mineral basaltic dykes at Yanac are typical calc-alkaline in composition, metaluminous, with ASI = 0.87-0.89, SiO_2 = 54-66%, MgO/TiO_2 (2.6-5.7), Al_2O_3 (16.7-18.6) and K_2O/Na_2O (< 1) ratios, belonging to the I-type magmas. They have enrichment of the LREE in relation to the HREE, indicating involvement of thick continental crust or subducted sediments with fluids, and enrichment of the LILE in relation to the HFSE, with negative anomalies of Nb and Ta, consistent with magmas associated with subduction zones in active continental margins. By the presence of magnetite as a accessory mineral in the Incahuasi granodiorite, porphyritic granodiorite and porphyritic granodiorite-diorite, these units are considered oxidized magmas.

The primary biotites of the Incahuasi granodiorite, porphyritic granodiorite, porphyritic granodiorite-diorite and intrusive intermineral dykes and enclaves have annite-phlogopite compositions and chemical characteristics compatible with calc-alkaline orogenic suites. The classification to the amphiloes for the Incahuasi granodiorite, porphyritic granodiorite, porphyritic granodiorite-diorite and intrusive inter-mineral dykes and enclaves are mainly magnesio-hornblendes.

For the basaltic dyke, the composition of the amphibole is pargasite and has a I-type magma. Together with the trachydacitic dyke, which is interpreted as generated from S-type magma, these dykes represent later episodes in the Yanac prospect and may be related with the evolution of the coastal batholith.

Propylitic alteration is mostly restricted to lateral zones and is characterized by veinlets type A1: quartz-chlorite-albite-carbonates-pyrite±chalcopyrite, A2: pyrite-quartz±chalcopyrite±molybdenite and A3: K-feldspar-epidote-chlorite-pyrite±chalcopyrite. Weak phyllic alteration occurs in the center of the prospect, and is spatially and probably genetically related with the main concentrations of Cu and Mo. It is characterized by the following subtypes veinlets: B1: quartz-pyrite-chalcopyrite-molybdenite with weak alteration halo of sericite-albite, B2: quartz-sericite and albite halo with a pyrite-molybdenite-chalcopyrite±K-feldspar suture, B3: sericite-chlorite-quartz-pyrite±chalcopyrite, B4: quartz-pyrite with a very pronounced sericite halo reaching up to 2 cm thick. Weak phyllic alteration may be related to the hydrothermal breccia (HB) by its similarity of alteration and mineralization. Strong phyllic alteration was considered as B5 assemblage: quartz-sericite-pyrite±albite subtype veinlets. Tthey completely destroy the original texture of the rock. The latest veins observed are dominated by distinguished subtype veinlets C1: laumontite-quartz-adularia, probably interpreted as the roots for an epithermal vein system of low sulphidation that was been eroded.

The porphyritic granodiorite-diorite played an important role for the generation of hydrothermal solutions and Cu and Mo enrichment. The evidences are the latest emplacement in relation to the other intrusives, the spatial position of the hydrothermal breccia between the Incahuasi granodiorite and the porphyritic granodiorite-diorite, moderate to pervasive stockwork structures and higher Cu and Mo values related to a weak phyllic alteration around the unit.

Subsequent supergenic process and erosion at Yanac define a thin oxidation-leached zone and an undetermined thickness of a mixed of oxide and supergenic enrichment.

The porphyritic granodiorite and porphyritic granodiorite-diorite are characterized by restricted ranges of *εHf(T)* (-0.28 – +6.65) and Hf T_{DM} from 460 to 740 Ma. The Incahuasi granodiorite, porphyritic granodiorite, porphyritic granodiorite-diorite, intrusive intermineral dykes, enclaves and basaltic dykes have an εNd(t) from -1.11 to 1.72 and $^{87}Sr/^{86}Sr(i)$ from 0.70450 to 0.70472, with Nd T_{DM} values between 520 and 850 Ma. suggesting a subcontinental mantle derivation with minor crustal component of recycled oceanic sediments or precambrian basement and indicating a similar evolution trend for them. These rocks are considered as the source of magmas and Cu-Mo metals. The trackydacite dyke has εNd(T) of -2.33,$^{87}Sr/^{86}Sr(i)$ of 0.70778 and Nd T_{DM} of 850, which indicate it was derived from materials with crustal affinities.

By the style of mineralization, the host rock, the metals, the hydrothermal alteration and the metallic minerals, Yanac is interpreted within the Cu(-Mo) porphyry-type depositmodel. Considering the mineralization as having the minimum age of 67.75 ± 0.80 Ma, it is placed within the upper Cretaceous metallogenic copper belt of the Peruvian Andes and forms part of an alignment of deposits and prospects with similar characteristics, like Almacen, Lara, Puquio (76 Ma) and Pucacorral Sur (82 Ma).

Investigation in deeper parts of the prospect is encouraged, in order to verify the existence of high temperature hydrothermal assemblages and possible higher metal concentrations. Economic concentrations of Cu-Mo in the transition porphyry-epithermal at Yanac and nearby should also be considered. It is possible that as more deposits are studied along the metallogenetic late Cretaceous belt of the Central Andes, in southern Peru, other Cu-Mo±Au deposits with characteristics similar to Yanac are described.

4.13. ACKNOWLEDGEMENTS

This work was possible due to financial support from the Coordenação de Aperfeiçoamento de Pessoal de Nível Superior (CAPES) from Brazil. We also thank the Estrella Gold Peru S.A.C. Company for its financial support during the field works. Valuable comments on geochronological and isotope data from Professor Natalia Hauser and assistance from the technical staff of the Geochronological, Microprobe and Microscopy laboratories of Universidade de Brasilia is also acknowledged.

REFERENCES

- Abdel-Rahman, A.F.M., 1994, Nature of biotites from alkaline, calc-alkaline and peraluminous granites: Journal of petrology, v. 35, p. 525-541.
- Acosta, J. Quispe, J., Santisteban, A. and Acosta, H., 2008, Épocas metalogenéticas y tipos de yacimientos metálicos en la margen occidental del sur del Perú, Latitudes 14°S - 18°S [abs.]: XIV Congreso Peruano de Geología, Lima, Volumen de Resúmenes, Sociedad Geológica del Perú, 6 p.
- Atherton, M.P., and Sanderson, L.M., 1985, The chemical variation and evolution of the super-units of the segmented Coastal batholith, in Pitcher, W.S., Atherton, M.P., Cobbing, E.J., and Beckingsale, R.D., eds., Magmatism at the plate edge: The Peruvian Andes: Glasgow, UK, Blackie, p. 208–227.
- Atherton, M.P., and Webb, S., 1989, Volcanic facies, structure, and geochemistry of the marginal basin rocks of central Peru: Journal of South American Earth Sciences, v. 2, p. 241–261.
- Barnes, H.L., 1997, Geochemistry of Hydrothermal Ore Deposits, 3rd ed.: Wiley and Sons, 972 p.
- Beckinsale, R.D., Sanchez-Fernandez, A.W., Brook, M., Cobbing, E.J., Taylor, W.P., and Moore, N.D., 1985, Rb-Sr whole-rock isochron and K-Ar age determinations for the Coastal batholith of Peru, in Pitcher, W.S., Atherton, M.P., Cobbing, E.J., and Beckingsale, R.D., eds., Magmatism at the plate edge: The Peruvian Andes: Glasgow, UK, Blackie, p. 177–202.
- Bellido, E. and Narvaez, S., 1960, Geología del Cuadrángulo de Atico: Compendio Carta Geológica Nacional, v. 2, 59 p.
- Benavides-Cáceres, V., 1999, Orogenic evolution of the Peruvian Andes: The Andean cycle: Society of Economic Geologists Special Publication 7, p.61–107.
- Bühn, B., Pimentel, M.M., Matteini, M., Dantas, E.L. 2009, High spatial resolution analysis of Pb and U isotopes for geochronology by laser ablation multi-collector inductively coupled plasma mass spectrometry (LA-MC-ICP-MS): Annals of the Academia Brasileira de Ciências, v. 81, p. 99-114.
- Camprubi A., Gonzáles, E., Jordi, G., Carrillo, A., 2003, Depósitos epitermales de alta y baja sulfuración: una tabla comparativa: Boletín de la Sociedad Geológica Mexicana, v. 56, p. 10-18.
- Camus, F., 2003, Geología de los sistemas porfíricos en los Andes de Chile: Santiago de Chile, Servicio Nacional de Geología y Minería, 267 p.
- Chacón, N., 1995, Geomorfología, in Palacios O.M., Sánchez A.F., Herrera F.R., eds., Geología del Perú, 1st ed.: Lima, Firmat S.A- Editores & Impresores, p. 7–14.
- Chemale, F., Philipp, R.P., Dussin, I.A., Formoso, M.L.L., Kawashita, K., Berttotti, A.L., 2011, Lu-Hf and U-Pb age determination of Capivarita Anorthosite in the Dom Feliciano Belt, Brazil: Precambrian Research, v. 186, p. 117-126.
- Clark A.H., 1990, Geologic and geochronologic constraints on the metallogenic evolution of the Andes of southeastern Peru: Economic Geology, v. 85, p. 1520-1583.
- Clarke, D.B., 1992, Granitoid rocks, Chapman & Hall, London, UK.

- Cobbing, E.J., 1978, The Andean geosyncline in Peru, and its distinction from Alpine geosynclines: Journal of the Geological Society, London, v. 135, p. 207–218.
- Cobbing, E.J., 1985, The tectonic setting of the Peruvian Andes, in Pitcher, W.S., Atherton, M.P., Cobbing, E.J., and Beckingsale, R.D., eds., Magmatism at the plate edge: The Peruvian Andes, Glasgow, UK, Blackie, p. 3–12.
- Corfu, F., Hanchar, J.M., Hoskin, P.W.O., and Kinny, P., 2003, Atlas of zircon textures: Reviews in Mineralogy and Geochemistry, v. 53, p. 469–500.
- Corvalán, J., 1990, Geologic-tectonic framework of the Andean region: Circum-Pacific Council for Energy and Mineral Resources Earth Science Series, v. 11, p. 1–11.
- Dalmayrac, B., Laubacher, G., Marocco R., 1980, Géologie des Andes péruviennes: Travaux et Documents de l' ORSTOM, v. 122, 501 p.
- De Haller, A., Corfu, F., Fontboté, L., Schaltegger, U., Barra, F., Chiaradia, M., Frank, M., Zúñiga, J., 2006, Geology, geochronology, and Hf and Pb isotope data of the Raúl-Condestable iron oxide-copper-gold deposit, central coast of Peru: Society of Economic Geologists, v. 101, p. 281-310.
- DePaolo, D.J., 1981. A neodymium and strontium isotopic study of Mesozoic calc-alkaline granitic batholith of the Sierra Nevada and Peninsular Ranges, California, Journal Geophysical Research 86, 10470-10488.
- Estrella Gold Peru, 2011, Mapa geológico-geoquímico superficial del depósito Yanac, escala 1:10,000.
- Gioia, S.M.C.L., Pimentel, M.M., 2000, The Sm-Nd Isotopic Method in the Geochronology Laboratory of the University of Brasília. Anais da Academia Brasileira de Ciências, 72(2): 219-245.
- Gradstein, F.M., Agterberg, F.P., Ogg, J.G., Hardenbol, J., Van Veen, P., Thierry, J., and Huang, Z., 1995, A Triassic, Jurassic and Cretaceous time scale, geochronology time scales and global stratigraphic correlation: Society for Sedimentary Geology, Special Publication 54, p. 95–126.
- Guevara, C., 1980, El Grupo Casma del Perú central entre Trujillo y Mala: Boletín de la Sociedad Geológica del Perú, v. 67, p. 73–83.
- Haederle M., and Atherton M.P., 2002, Shape and intrusion style of the Coastal batholith, Peru: Tectonophysics, v. 345, p. 17–28.
- Hoskin, P.W.O., and Schaltegger, U., 2003, The composition of zircon and igneous and metamorphic petrogenesis: Reviews in Mineralogy and Geochemistry, v. 53, p. 27–62.
- ICDD, 1996, Powder Diffraction File, PDF-2 Data base Sets: International Centre for Diffraction Data, Newtown Square.
- INGEMMET, 2013, Mapa Geológico del Perú: Instituto Geológico Minero y Metalúrgico del Perú (http://geocatmin.ingemmet.gob.pe/geocatmin/).
- Injoque, J., 2002, Fe oxide-Cu-Au deposits in Peru: An integrated view, in Porter, T.M., ed., Hydrothermal iron oxide copper-gold and related deposits: A global perspective, Adelaide, Porter GeoConsultancy Publishing, vol. 2, p. 97–113.
- Irvine, T. N., Baragar, W.R.A., 1971, A guide to the chemical classification of the common volcanic rocks: Canadian Journal of Earth Science, v. 8, p. 523-548.
- Ishihara S., 1977, The magnetite-series and ilmenite-series granitic rocks, Mining Geology, v. 27, p. 293-305.

- Jackson, S.E., Pearson, N.J., Griffin, W.L., Belousova, E.A., 2004, The application of laser ablation inductively coupled plasma mass spectrometry to in situ U-Pb zircon geochronology: Chemical Geology, v. 211, p. 47-69.
- Jaillard, E., Soler, P., Carlier, G., and Mourier, T., 1990, Geodynamic evolution of the northern and central Andes during early to middle Mesozoic times: A Thetyan model: Journal of the Geological Society of London, v. 147, p. 1009–1022.
- Kinny, P.D. and Maas, R., 2003. Lu-Hf and Sm-Nd isotope systems in zircon, In Hanchar, J.M. and Hoskin, P.W.O., eds., Zircon, Mineralogical Society of America and Geochemical Society, Reviews in Mineralogy and Geochemistry, v. 53, p. 327-341.
- Leake, B.E. *et al.*, 1997, Nomenclature of amphiboles: report of the subcommittee on amphiboles of the international mineralogical association, commission on new minerals and mineral names: The Canadian Mineralogist, v. 35, p. 219-246.
- LeBAS, M.J., Le Maitre, R.W., Streckeisen, A., Zanettin, B., 1986, A chemical classification of volcanic rocks based on the total alkali-silica diagram: Journal of petrology, v. 27, p. 745-750.
- Ludwig, K.R., 2009, Isoplot, A geochronological toolkit for Microsoft Excel, Ver. 3.71.09.05.23nx. Berkeley Geochronology Center.
- Maniar, P. D. and Piccoli, P. M., 1989, Tectonic discriminations of granitoids: Geological Society of America, v. 101, p. 635–643.
- Matteini, M., Junges, S.L., Dantas, E.L., Pimentel, M.M., Bühn, B., 2010, In Situ zircon U-Pb and Lu-Hf isotope systematic on magmatic rocks: Insights on the crustal evolution of the Neoproterozoic Goiás Magmatic Arc, Brasília belt, Central Brazil: Gondwana Research, v. 17, p. 1-12.
- Middlemost, E., 1985, Magmas and magmatic rocks: An introduction to igneous petrology: Longman Scientific and Technical, 266 p.
- Moore, N.D., and Agar, R.A., 1985, Variations along a batholith: the Arequipa segment of the Coastal batholith of Peru, in Pitcher, W.S., Atherton, M.P., Cobbing, E.J., and Beckingsale, R.D., eds., Magmatism at the plate edge: The Peruvian Andes: Glasgow, UK, Blackie, p. 108–118.
- Mukasa, S.B., 1986, Common Pb isotopic compositions of the Lima, Arequipa and Toquepala segments in the Coastal batholith, Peru: Implications for magmagenesis: Geochimica et Cosmochimica Acia, v. 50, p. 771-782
- Mukasa, S.B., 1986a, Zircon U-Pb ages of super-units in the Coastal batholith, Peru: Implications for magmatic and tectonic processes: Geological Society of America Bulletin, v. 97, 241–254.
- Mukasa, S.B., and Tilton, G.R., 1985, Zircon U-Pb ages of super-units in the Coastal batholith, Peru, in Pitcher, W.S., Atherton, M.P., Cobbing, E.J., and Beckingsale, R.D., eds., Magmatism at the plate edge: The Peruvian Andes: Glasgow, UK, Blackie, p. 203–207.
- Nachit, H., Ibhi A., Abia, E., Ohoud M.B., 2005, Discrimination between primary magmatic biotites, reequilibrated biotites and neoformed biotites: Geomaterials (mineralogy), v. 337, p 1415-1420.
- Noble, D.C., Ríos C., A, Vidal, C.E., Spell, T.L., Zanetti, K.A., Angeles Z., C., Ochoa A., J.L., Cruz C., S.R., in press (b), Late Cretaceous basalt in the Río Mala valley, central Peru: Evidence for extention and mafic magmatism prior to Late Cretaceous-Paleocene plutonism and silicic volcanism, in Arce Helberg,

J.E., ed., Volumen Especial N° 6 Alberto Giesecke Matto, Sociedad Geologica del Peru.

- Noble, D.C., Vidal, C.E., Angeles Z., C., Wise, J.M., Zanetti, K.A., Spell, T.L., in press (a), Caldera-related ash-flow tuff of Paleocene age in central Peru and its significance for Late Cretaceous and Paleocene magmatism, sedimentation and tectonism, in Arce Helberg, J.E., ed., Volumen Especial N° 6 Alberto Giesecke Matto, Sociedad Geologica del Peru.
- Osterman, G., Cardozo, M., and Wauschkuhn, A., 1983, Descripción y correlación de los depósitos volcánicos-sedimentarios del Cretácico inferior en la región Lima-Cañete: Boletín de la Sociedad Geológica del Perú, v. 70, p. 35–46.
- Palacios O.M., 1995, Estratigrafía, in Palacios O.M., Sánchez A.F., Herrera F.R., eds., Geología del Perú, 1st ed., Lima, INGEMMET, Firmat S.A.- Editores & Impresores, p. 45–85.
- Palacios, O., Caldas, J., and Vela, C., 1992, Geología de los cuadrángulos de Lima, Lurín, Chancay y Chosica: Compendio Carta Geológica Nacional, v. 43, 163 p.
- Pearce, J,A., Harris, N.B., Tindle A.G., 1984, Trace element discrimination diagrams for the tectonic interpretation of granitic rocks: Journal of petrology, v. 25, p. 956-983.
- Peccerillo, A. and Taylor, S. R., 1976, Geochemistry of Eocene calc-alkaline volcanic rocks from the Kastamonu area, Northern Turkey: Contributions to Mineralogy and Petrology, v. 58, p. 63–81.
- Pichowiak S. and Breitdreuz C., 1984, Volcanic dykes in the North Chilean Coast: Geologische Rundschau, v. 73, p. 853-868.
- Pitcher, W.S. 1985, A multiple and composite batholith, in Pitcher, W. S., Atherton, M.P., Cobbing E.J., Beckinsale R.D., eds., Magmatism at a plate edge: The peruvian Andes, New York, John Wiley and Sons Inc, p. 243-249.
- Pitcher, W.S., Atherton, M.P., Cobbing, E.J., and Beckinsale, R.D., 1985, A model for the Coastal batholith, in Pitcher, W.S., Atherton, M.P., Cobbing, E.J., and Beckingsale, R.D., eds., Magmatism at the plate edge: The Peruvian Andes: Glasgow, UK, Blackie, p. 239–240.
- Polliand, M., Schaltegger, U., Frank, M., and Fontboté, L., 2005, Formation of intra-arc volcano-sedimentary basins in the western flank of the central Peruvian Andes during Late Cretaceous oblique subduction—field evidence and constraints from U-Pb ages and Hf isotopes: International Journal of Earth Sciences, v. 94, p. 231–242.
- Regan, P.F., 1985, The early basic intrusions, in Pitcher, W.S., Atherton, M.P., Cobbing, E.J., and Beckingsale, R.D., eds., Magmatism at the plate edge: The Peruvian Andes: Glasgow, UK, Blackie, p. 72–90.
- Rieder, M., 1999, Nomenclature of the micas, Mineral. Mag., v. 63, n.2, p. 267-279.
- Rivera, F., 2007, Caracterización Genética y Potencial Económico del Prospecto Pórfido de Cu-Mo Puquio: Unpublished graduation thesis, Lima, Universidad Nacional Mayor de San Marcos, p. 112.
- Rivera, F., 2012, Geología y Geocronología del Pórfido de Cu-Au Zafranal, en el Sur del Perú: XVI Congreso Peruano de Geología y SEG 2012 Conference, Lima, 5 p.

- Rivera, F., Moretti, A. y Baumgartner, R. 2008, La franja Cretácea de pórfidos de cobre en el sur del Perú: XII Congreso Latinoamericano de Geología y XIV Congreso Peruano de Geología, Lima, 2008, CD-ROM, 6 p.
- Rivera, R., Petersen, G., and Rivera, M., 1975, Estratigrafía de la costa de Lima: Boletín de la Sociedad Geológica del Perú, v. 45, p. 159–186.
- Salazar, H., and Landa, C., 1993, Geología de los cuadrángulos de Mala, Lunahuaná, Tupe, Conayca, Chincha, Tantará y Castrovirreyna: Instituto Geológico Minero y Metalúrgico del Perú, v. 44, 91 p.
- Seedorff, E., Dilles, J.H., Proffett, J.M., Jr., Einaudi, M.T., Zurcher, L., Stavast, W.J.A., Johnson, D.A., and Barton, M.D., 2005, Porphyry deposits: characteristics and origin of hypogene features, in Hedenquist, J. W., Thompson, J. F. H., Goldfarb, R. J., Richards, J. P., eds., One Hundredth Anniversary Volume, Economic Geology, p. 251-298.
- Sillitoe, R.H. and Perello, J., 2005, Andean copper province: tectonomagmatic settings, deposit types, Metallogeny, exploration, and discovery, in Hedenquist, J.W.; Thompson, J.F.H.; Goldfarb, R.; Richards, J., eds., Economic Geology One Hundredth Anniversary Volume, Society of Economic Geologists, Littleton, Colorado, USA., p. 845-890.
- Sillitoe, R.H., 1998, Major regional factors favouring large size, high hypogene grade, elevated gold content and supergene oxidation and enrichment of porphyry copper deposits, in Porter, T.M., ed., Porphyry and hydrothermal copper and gold deposits: A global perspective: Adelaide, Australian Mineral Foundation, p. 21–34.
- Sillitoe, R.H., 2003, Iron oxide-copper-gold deposits—An Andean view: Mineralium Deposita, v. 38, p. 787–812.
- Sillitoe, R.H., 2010, Porphyry copper systems: Economic Geology, v. 105, p. 3–41.
- Silva, E., 2008, Sistema Porfirítico Pucacorral Sur – Características Geológicas y Potencial Económico: Unpublished graduation thesis, Lima, Universidad Nacional Mayor de San Marcos, 97 p.
- Skewes, M.A. and Stern, C.R., 1994, Tectonic trigger for the formation of Late Miocene Cu-rich megabreccias in the Andes of central Chile: Geology, v. 22, p. 551–554.
- Soler, P., and Rotach-Toulhoat, N., 1990, Implications of the time-dependent evolution of Pb- and Sr-isotopic compositions of Cretaceous and Cenozoic granitoids from the coastal region and the lower Pacific slope of the Andes of central Peru, in Kay, S. M., and Rapela, C. W., eds., Plutonism from Antarctica to Alaska, Boulder, Colorado, Geological Society of America, special paper 241.
- Streckeisen, A., 1976, To each plutonic rock its proper name: Earth Science., v. 12, p. 1-33.
- Sun, S.S. and Mcdonough, W.F., 1989, Chemical and isotopic systematics of oceanic basalts: Implications for mantle composition and pro-cesses, In Saunders, A.D. and Norrys, M.J., eds., Magmatism in the ocean basins, Geology Sociaty of London, Special Publication, v. 42, p. 313-345.
- Tumialán P., 2003, Compendio de Yacimientos Minerales del Perú: INGEMMET, v. 10, 619 p.
- Uyeda, S. and Kanamori, H., 1979, Back-arc opening and mode of subduction: Journal of Geophysical Research, v. 84, p. 1049-1061.

- Vela, C., 1997, Nueva concepción estratigráfica de la subcuenca de Lima, ext. abs.: IX Congreso Peruano de Geología, Resúmenes Extendidos, Lima, Sociedad Geológica del Perú, Vol. Esp. 1, p. 409–412.
- Whalen, J.B., 1985, Geochemistry of an island-arc plutonic suite: the Uasilau-Yau Yau intrusive complex New Britian PNG: Journal of Petrology, v. 26, p. 319-327.
- White, A. J. R. and Chappell, B. W., 1983, Granitoid types and their distribution in the Lachlan Fold Belt, southeastern Australia, in Roddick, J. A., ed., Circum-Pacific Plutonic Terranes, Geological Society of America Memoirs, v. 159, p. 21–34.
- Wilkinson, J., 2013, Triggers for the formation of porphyry ore deposits in magmatic arcs, Nature Geoscience, Vol. 6, p. 917-925.
- Wilson, J.J., 1963, Cretaceous stratigraphy of central Andes of Peru: Bulletin of the American Association of Petroleum Geologists, v. 47, p. 1–34.
- Winter, J.D., 2009, Principles of igneous and metamorphic petrology, 2nd ed.: New Jersey, Prentice Hall, 720 p.
- Wood, D.A., Joron, J.-L., and Treuil, M., 1979, A re-appraisal of the use of trace elements to classify and discriminate between magma series erupted in different tectonic settings: Earth Planet. Sci. Letts., v. 45, p. 326-336.

ANNEX 1

DIFFRACTOGRAMS

ANNEX 1 DIFFRACTOGRAM TO SAMPLE AY-23, LAUMONTITE

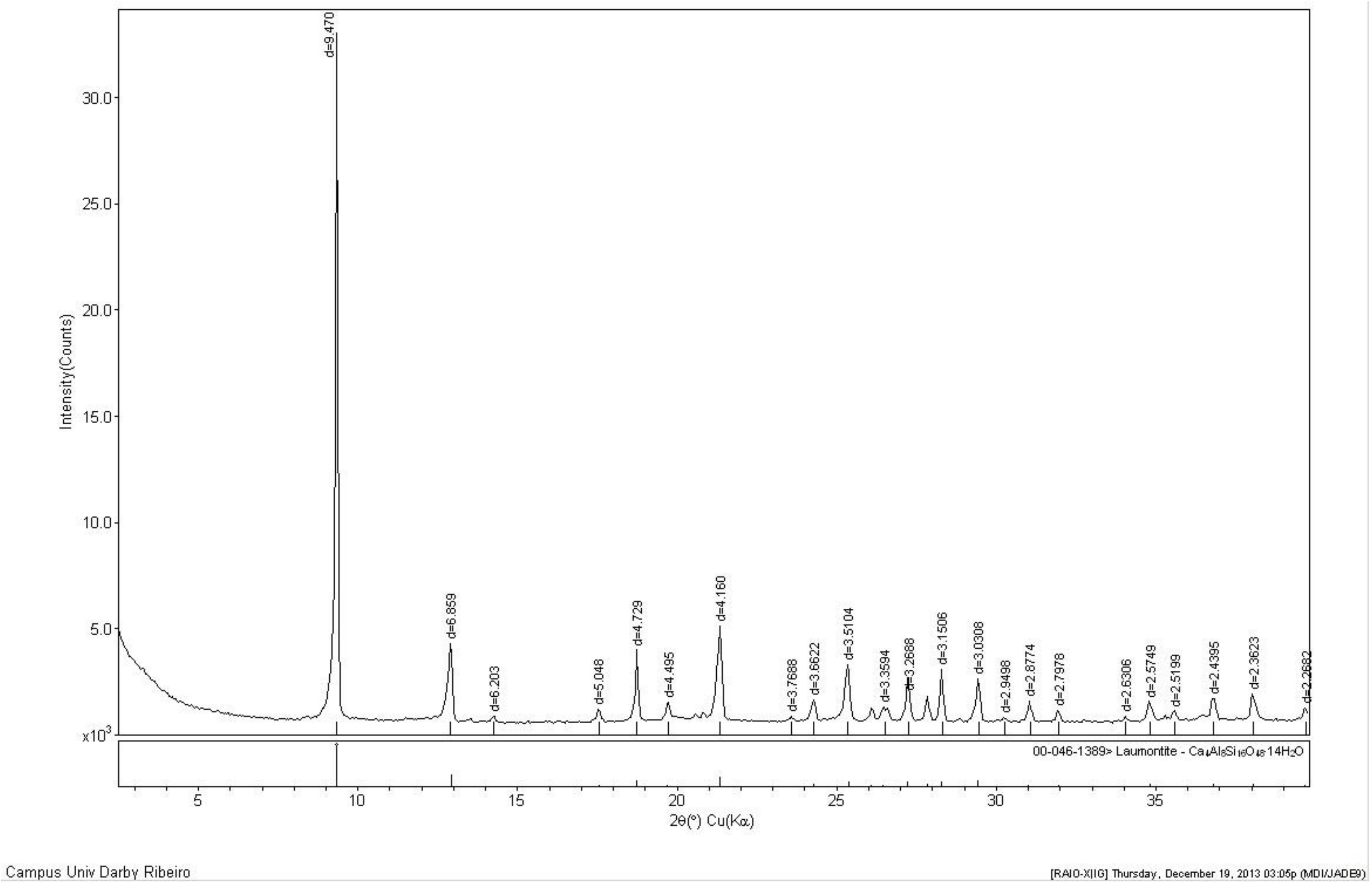

ANNEX 1 DIFFRACTOGRAM TO SAMPLE AY-18, QUARTZ-ADULARIA

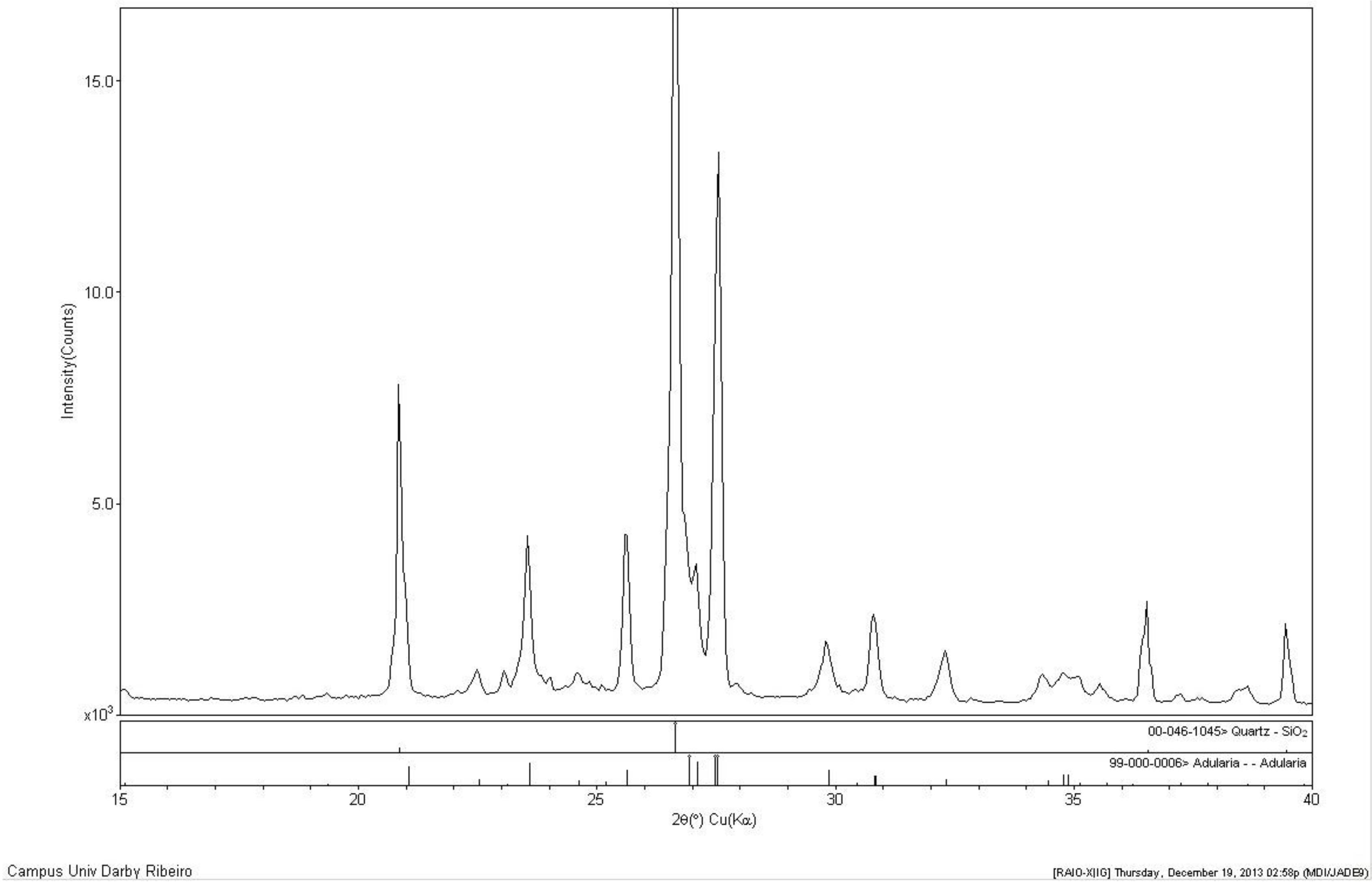

ANNEX 1 DIFFRACTOGRAM TO SAMPLE AY-41-A, JAROSITE

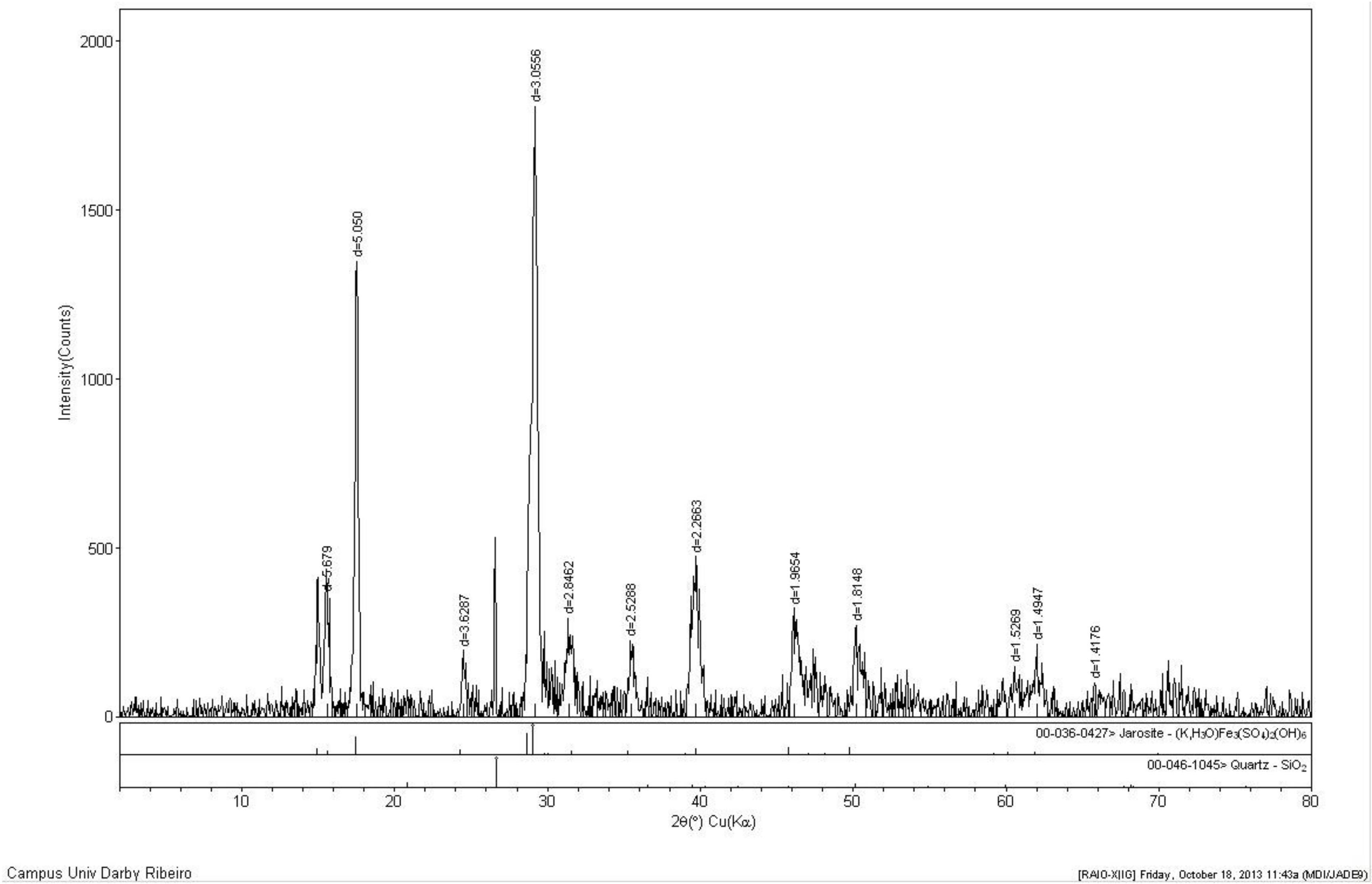

ANNEX 1 DIFFRACTOGRAM TO YELLOWISH CLAY MATERIAL, COQUIMBITE AND ALUMINOCOPIAPITE

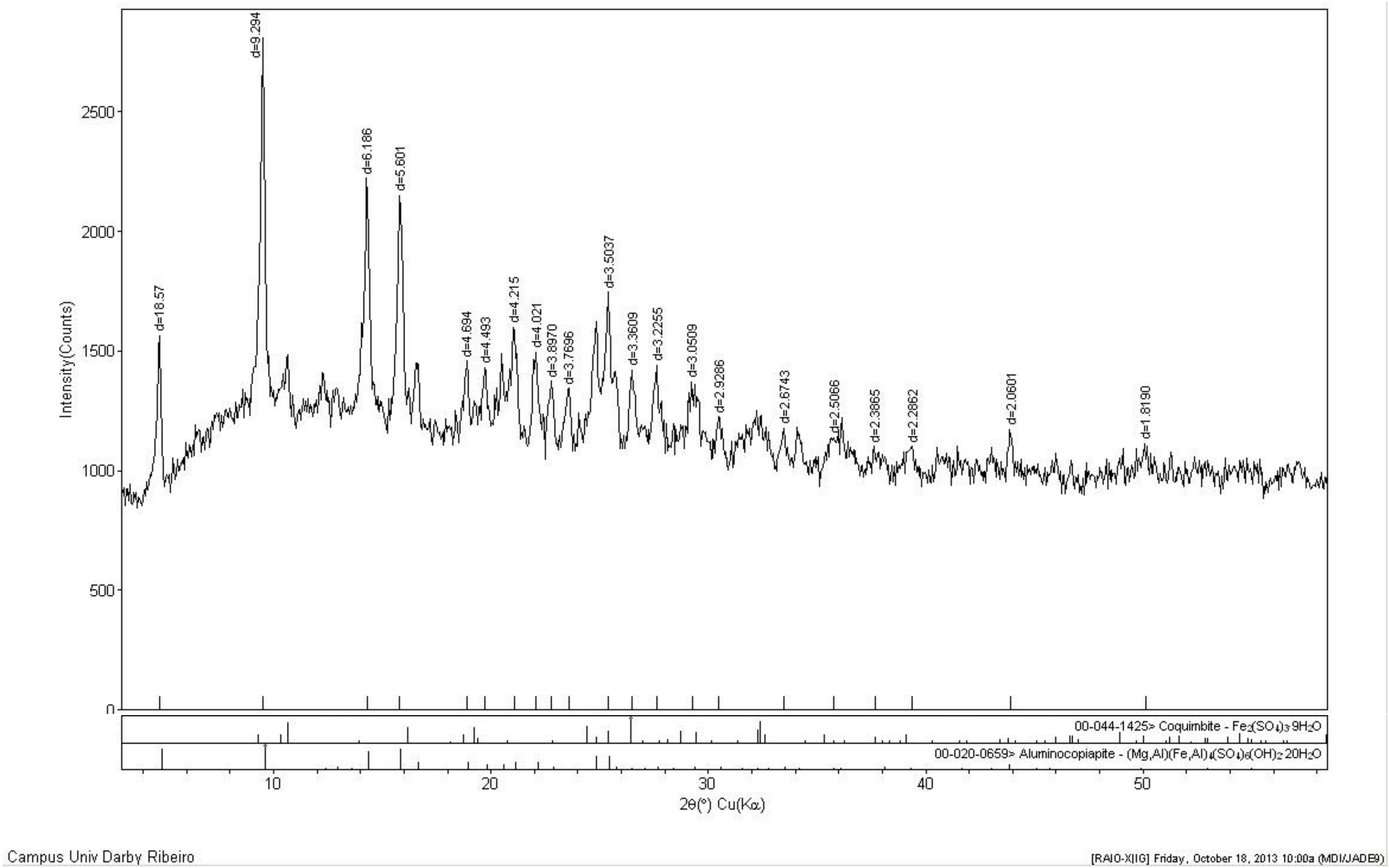

ANNEX 2

BIOTITE MINERAL CHEMISTRY

ANNEX 2 BIOTITE MINERAL CHEMISTRY

	PGD	Porphyritic granodiorite (PG									
	ay05-1	**ay23d-1**	**ay23d-2**	**ay23e-2**	**ay23e-4a**	**ay23e-4b**	**ay23e-4a1**	**ay23e-4a2**	**ay23e-4b1**	**ay23e-4b2**	**ay23e-4b3**
SiO_2	37.694	39.754	40.285	39.304	36.255	37.346	38.102	38.314	37.856	37.569	38.807
TiO_2	3.703	4.114	4.008	4.377	4.1	4.367	4.151	4.152	3.722	4.442	3.024
Al_2O_3	13.693	14.521	14.28	14.352	14.036	13.908	14.173	13.172	14.147	13.978	16.964
FeO	17.359	13.284	12.694	14.31	17.479	16.794	17.404	16.558	16.839	16.756	15.953
MnO	0.349	0.485	0.498	0.516	0.358	0.448	0.387	0.243	0.389	0.454	0.367
MgO	13.97	15.441	15.149	13.886	13.246	12.682	12.932	13.526	12.454	13.165	10.268
CaO	0.06	0.078	0.069	0.091	0.106	0.076	0.066	0.053	0.093	0.072	0.217
Na_2O	0.26	0.127	0.09	0.163	0.389	0.241	0.159	0.298	0.112	0.352	0.047
K_2O	5.311	5.964	5.516	5.599	4.546	5.242	7.965	9.345	5.633	8.997	6.509
BaO	0.8	0.647	0	0.751	0.58	0.699	0.5	0.745	0.103	0.456	0.015
Cr_2O_3	0.03	0	0	0.031	0.024	0.047	0.016	0.046	0	0	0
NiO	0.048	0.088	0	0	0	0	0	0	0	0	0
H_2O*	3.77	3.97	3.87	3.76	3.67	3.74	3.83	3.88	3.70	3.84	3.82
Cl	0.125	0.132	0.097	0.141	0.235	0.194	0.192	0.119	0.182	0.176	0.093
F	0.305	0.186	0.37	0.499	0.29	0.248	0.274	0.205	0.336	0.259	0.268
Total	97.32	98.69	96.74	97.53	95.14	95.88	100.00	100.54	95.38	100.36	96.21
Si	5.723	5.821	5.942	5.849	5.625	5.739	5.695	5.733	5.818	5.627	5.866
Al iv	2.277	2.179	2.058	2.151	2.375	2.261	2.305	2.267	2.182	2.373	2.134
Sitio T	**8.000**	**8.000**	**8.000**	**8.000**	**8.000**	**8.000**	**8.000**	**8.000**	**8.000**	**8.000**	**8.000**
Al vi	0.174	0.327	0.425	0.367	0.191	0.258	0.192	0.056	0.381	0.094	0.888
Ti	0.423	0.453	0.445	0.490	0.478	0.505	0.467	0.467	0.430	0.500	0.344
Fe	2.204	1.627	1.566	1.781	2.268	2.158	2.176	2.072	2.164	2.099	2.017
Mn	0.045	0.060	0.062	0.065	0.047	0.058	0.049	0.031	0.051	0.058	0.047
Mg	3.162	3.370	3.331	3.081	3.063	2.905	2.881	3.017	2.853	2.939	2.314
Sitio M	**6.008**	**5.838**	**5.829**	**5.783**	**6.048**	**5.884**	**5.765**	**5.643**	**5.880**	**5.690**	**5.609**
Na	0.077	0.036	0.026	0.047	0.117	0.072	0.046	0.086	0.033	0.102	0.014
K	1.029	1.114	1.038	1.063	0.900	1.027	1.519	1.784	1.104	1.719	1.255
Ba	0.048	0.037	0.000	0.044	0.035	0.042	0.029	0.044	0.006	0.027	0.001
Sitio I	**1.153**	**1.187**	**1.064**	**1.154**	**1.052**	**1.141**	**1.594**	**1.914**	**1.144**	**1.848**	**1.270**
OH*	3.821	3.881	3.803	3.730	3.796	3.829	3.822	3.873	3.789	3.833	3.848
Cl	0.032	0.033	0.024	0.036	0.062	0.051	0.049	0.030	0.047	0.045	0.024
F	0.146	0.086	0.173	0.235	0.142	0.121	0.130	0.097	0.163	0.123	0.128
Sitio A	**4.000**	**4.000**	**4.000**	**4.000**	**4.000**	**4.000**	**4.000**	**4.000**	**4.000**	**4.000**	**4.000**

ANNEX 2 BIOTITE MINERAL CHEMISTRY

	Porphyritic granodiorite (PG)										
	ay23e1-1-1	**ay23e1-1-2**	**ay23e1-1a**	**ay23e1-1b**	**ay23e1-2a**	**ay23e1-2b**	**ay23e1-3a**	**ay23e1-3b**	**ay23e1-4a**	**ay23e1-4b**	**ay23e1-1a1**
SiO_2	38.134	37.39	36.147	37.487	37.628	37.632	37.746	37.145	38.864	37.436	37.295
TiO_2	4.149	3.283	4.046	4.03	4.276	4.426	4.214	4.237	4.361	4.325	4.258
Al_2O_3	13.603	15.598	12.741	13.201	13.2	13.65	13.484	13.297	13.685	13.156	13.129
FeO	16.644	15.724	15.865	15.658	16.494	16.98	16.664	16.885	15.862	16.024	16.392
MnO	0.464	0.377	0.335	0.368	0.327	0.432	0.225	0.521	0.356	0.486	0.301
MgO	13.084	10.202	12.971	13.71	13.62	12.724	13.404	12.192	14.062	13.718	13.191
CaO	0.062	0.22	0.094	0.062	0.066	0.084	0.032	0.056	0.047	0.087	0.035
Na_2O	0.186	0.314	1.193	0.215	0.241	0.212	0.177	0.136	0.249	0.171	0.21
K_2O	5.485	6.68	5.251	5.74	5.452	5.679	5.274	5.314	5.419	5.46	9.494
BaO	0.65	0.294	0.376	0.459	0.634	0.605	0.707	0.552	0.635	0.552	0.783
Cr_2O_3	0.005	0	0	0	0.017	0	0	0	0.012	0.013	0
NiO	0	0	0	0	0	0	0	0	0	0	0
H_2O*	3.82	3.70	3.61	3.71	3.72	3.71	3.79	3.63	3.78	3.73	3.77
Cl	0.155	0.16	0.181	0.191	0.178	0.167	0.169	0.161	0.126	0.109	0.135
F	0.17	0.216	0.254	0.257	0.307	0.357	0.178	0.342	0.408	0.282	0.276
Total	96.50	94.03	92.92	94.94	95.99	96.47	95.95	94.29	97.67	95.41	99.12
Si	5.811	5.838	5.740	5.794	5.771	5.760	5.782	5.808	5.815	5.765	5.681
Al iv	2.189	2.162	2.260	2.206	2.229	2.240	2.218	2.192	2.185	2.235	2.319
Sitio T	**8.000**	**8.000**	**8.000**	**8.000**	**8.000**	**8.000**	**8.000**	**8.000**	**8.000**	**8.000**	**8.000**
Al vi	0.254	0.709	0.124	0.199	0.157	0.222	0.216	0.258	0.229	0.152	0.038
Ti	0.475	0.386	0.483	0.468	0.493	0.509	0.485	0.498	0.491	0.501	0.488
Fe	2.121	2.053	2.107	2.024	2.116	2.173	2.135	2.208	1.985	2.064	2.088
Mn	0.060	0.050	0.045	0.048	0.042	0.056	0.029	0.069	0.045	0.063	0.039
Mg	2.972	2.375	3.070	3.159	3.114	2.903	3.061	2.842	3.137	3.149	2.995
Sitio M	**5.882**	**5.573**	**5.830**	**5.899**	**5.922**	**5.864**	**5.926**	**5.875**	**5.887**	**5.929**	**5.647**
Na	0.055	0.095	0.367	0.064	0.072	0.063	0.053	0.041	0.072	0.051	0.062
K	1.066	1.330	1.064	1.132	1.067	1.109	1.030	1.060	1.034	1.072	1.845
Ba	0.039	0.018	0.023	0.028	0.038	0.036	0.042	0.034	0.037	0.033	0.047
Sitio I	**1.160**	**1.444**	**1.454**	**1.224**	**1.176**	**1.208**	**1.125**	**1.135**	**1.144**	**1.157**	**1.953**
OH*	3.878	3.851	3.824	3.824	3.805	3.784	3.870	3.788	3.775	3.834	3.832
Cl	0.040	0.042	0.049	0.050	0.046	0.043	0.044	0.043	0.032	0.028	0.035
F	0.082	0.107	0.128	0.126	0.149	0.173	0.086	0.169	0.193	0.137	0.133
Sitio A	**4.000**	**4.000**	**4.000**	**4.000**	**4.000**	**4.000**	**4.000**	**4.000**	**4.000**	**4.000**	**4.000**

ANNEX 2 BIOTITE MINERAL CHEMISTRY

	Porphyritic granodiorite (PG)										
	ay23e1-1b1	**ay23e1-2a1**	**ay23e1-2b1**	**ay23e1-3a1**	**ay23e1-3b1**	**ay23e1-4a1**	**ay23e1-4b1**	**ay23e2-2a**	**ay23e2-2b**	**ay23e2-1a**	**ay23e2-1b**
SiO_2	38.663	37.925	38.277	38.674	37.817	39.092	38.651	37.713	38.024	38.424	39.385
TiO_2	4.16	4.31	4.359	4.116	4.276	4.289	4.335	4.198	4.452	4.45	4.76
Al_2O_3	13.568	13.361	13.563	13.367	13.289	13.282	13.537	14.683	14.238	14.495	14.368
FeO	16.097	16.837	16.705	16.945	16.913	16.045	15.953	12.814	13.027	13.088	13.985
MnO	0.379	0.248	0.428	0.309	0.436	0.535	0.482	0.262	0.455	0.48	0.46
MgO	13.285	13.719	13.178	13.747	12.48	13.934	13.727	14.799	14.309	14.868	14.251
CaO	0.067	0.047	0.073	0.013	0.008	0.099	0.069	0.068	0.045	0.071	0.067
Na_2O	0.249	0.288	0.216	0.174	0.24	0.173	0.185	0.136	0.206	0.076	0.135
K_2O	9.608	9.317	9.096	8.95	9.045	9.165	9.11	9.08	9.251	9.442	9.246
BaO	0.635	0.906	0.788	0.854	0.53	0.501	0.612	0.648	0.712	0.280	0.668
Cr_2O_3	0.024	0.023	0.017	0	0.039	0.096	0.072	0.013	0.03	0.026	0.000
NiO	0	0	0	0	0	0	0	0	0	0.000	0.000
H_2O*	3.82	3.83	3.90	3.84	3.75	3.84	3.84	3.79	3.84	3.84	3.92
Cl	0.204	0.161	0.158	0.128	0.115	0.149	0.163	0.171	0.135	0.045	0.082
F	0.339	0.298	0.16	0.363	0.371	0.405	0.334	0.355	0.283	0.449	0.379
Total	100.91	101.11	100.82	101.30	99.12	101.40	100.90	98.55	98.86	99.84	101.52
Si	5.752	5.662	5.710	5.736	5.740	5.765	5.732	5.645	5.691	5.673	5.737
Al iv	2.248	2.338	2.290	2.264	2.260	2.235	2.268	2.355	2.309	2.327	2.263
Sitio T	**8.000**	**8.000**	**8.000**	**8.000**	**8.000**	**8.000**	**8.000**	**8.000**	**8.000**	**8.000**	**8.000**
Al vi	0.131	0.014	0.094	0.073	0.118	0.073	0.098	0.236	0.203	0.196	0.204
Ti	0.465	0.484	0.489	0.459	0.488	0.476	0.483	0.473	0.501	0.495	0.521
Fe	2.003	2.102	2.084	2.102	2.147	1.979	1.978	1.604	1.631	1.616	1.704
Mn	0.048	0.031	0.054	0.039	0.056	0.067	0.061	0.033	0.058	0.061	0.057
Mg	2.946	3.053	2.930	3.040	2.824	3.063	3.034	3.302	3.193	3.272	3.095
Sitio M	**5.594**	**5.685**	**5.652**	**5.713**	**5.632**	**5.657**	**5.655**	**5.649**	**5.585**	**5.639**	**5.581**
Na	0.072	0.083	0.062	0.050	0.071	0.049	0.053	0.039	0.060	0.022	0.038
K	1.823	1.774	1.731	1.693	1.751	1.724	1.723	1.734	1.766	1.778	1.718
Ba	0.037	0.053	0.046	0.050	0.032	0.029	0.036	0.038	0.042	0.016	0.038
Sitio I	**1.932**	**1.911**	**1.839**	**1.793**	**1.853**	**1.802**	**1.812**	**1.811**	**1.868**	**1.816**	**1.794**
OH*	3.789	3.819	3.885	3.798	3.792	3.774	3.802	3.789	3.832	3.779	3.805
Cl	0.051	0.041	0.040	0.032	0.030	0.037	0.041	0.043	0.034	0.011	0.020
F	0.160	0.141	0.075	0.170	0.178	0.189	0.157	0.168	0.134	0.210	0.175
Sitio A	**4.000**	**4.000**	**4.000**	**4.000**	**4.000**	**4.000**	**4.000**	**4.000**	**4.000**	**4.000**	**4.000**

ANNEX 2 BIOTITE MINERAL CHEMISTRY

	PG	Incahuasi granodiorite (IG)			Intrusive Intermineral dykes and enclaves (IIDE)						
	ay24-10	**ay12-2a**	**ay12-2b**	**ay01-2-1**	**ay16-1a**	**ay16-1c**	**ay16-1b**	**ay16-2c**	**ay16-2b**	**ay16-1-1**	**ay03-2-1**
SiO_2	37.944	38.224	38.222	39.149	37.714	36.933	36.708	37.068	37.358	36.923	39.393
TiO_2	3.88	3.98	4.355	4.103	4.39	3.97	4.009	4.035	4.429	3.808	3.999
Al_2O_3	14.388	12.962	12.901	13.598	12.968	12.701	12.633	12.826	12.836	13.43	13.20
FeO	17.536	16.956	17.478	16.861	17.807	16.56	17.217	17.097	17.512	17.71	17.29
MnO	0.35	0.42	0.408	0.285	0.443	0.466	0.416	0.424	0.388	0.384	0.262
MgO	11.790	13.935	13.302	13.51	12.889	12.707	13.05	12.977	12.575	13.64	12.95
CaO	0.056	0.024	0.111	0.006	0.038	0.081	0.085	0.077	0.053	0.085	0.051
Na_2O	0.222	0.211	0.241	0.216	0.178	0.312	0.312	0.254	0.167	0.213	0.312
K_2O	9.909	8.882	9.481	5.949	9.805	9.409	8.666	9.732	9.729	5.034	5.687
BaO	0.132	1.015	0.431	0.764	0.671	0.584	0.832	0.831	0.707	0.632	0.636
Cr_2O_3	0.052	0.000	0.017	0	0.016	0.059	0	0	0	0.000	0.010
NiO	0.000	0.000	0	0	0	0	0	0	0	0.015	0.017
H_2O*	3.86	3.93	3.96	3.93	3.86	3.76	3.77	3.84	3.85	3.76	3.86
Cl	0.154	0.126	0.11	0.109	0.268	0.245	0.255	0.211	0.198	0.143	0.156
F	0.186	0.089	0.054	0.111	0.11	0.102	0.083	0.051	0.075	0.196	0.181
Total	100.35	100.69	101.02	98.52	101.05	97.80	97.95	99.35	99.80	95.86	97.90
Si	5.702	5.722	5.713	5.847	5.676	5.715	5.678	5.673	5.688	5.698	5.920
Al iv	2.298	2.278	2.273	2.153	2.300	2.285	2.303	2.314	2.304	2.302	2.080
Sitio T	**8.000**	**8.000**	**8.000**	**8.000**	**8.000**	**8.000**	**8.000**	**8.000**	**8.000**	**8.000**	**8.000**
Al vi	0.250	0.009	0.000	0.241	0.000	0.032	0.000	0.000	0.000	0.141	0.259
Ti	0.438	0.448	0.490	0.461	0.497	0.462	0.466	0.464	0.507	0.442	0.452
Fe	2.204	2.123	2.185	2.106	2.241	2.143	2.227	2.188	2.230	2.286	2.173
Mn	0.045	0.053	0.052	0.036	0.056	0.061	0.055	0.055	0.050	0.050	0.033
Mg	2.641	3.110	2.964	3.008	2.891	2.931	3.009	2.961	2.854	3.138	2.901
Sitio M	**5.578**	**5.744**	**5.690**	**5.852**	**5.686**	**5.629**	**5.757**	**5.668**	**5.641**	**6.057**	**5.818**
Na	0.065	0.061	0.070	0.063	0.052	0.094	0.094	0.075	0.049	0.064	0.091
K	1.899	1.696	1.808	1.133	1.882	1.857	1.710	1.900	1.889	0.991	1.090
Ba	0.008	0.060	0.025	0.045	0.040	0.035	0.050	0.050	0.042	0.038	0.037
Sitio I	**1.972**	**1.817**	**1.903**	**1.241**	**1.974**	**1.986**	**1.854**	**2.025**	**1.981**	**1.093**	**1.219**
OH*	3.872	3.926	3.947	3.920	3.879	3.886	3.893	3.921	3.913	3.867	3.874
Cl	0.039	0.032	0.028	0.028	0.068	0.064	0.067	0.055	0.051	0.037	0.040
F	0.088	0.042	0.026	0.052	0.052	0.050	0.041	0.025	0.036	0.096	0.086
Sitio A	**4.000**	**4.000**	**4.000**	**4.000**	**4.000**	**4.000**	**4.000**	**4.000**	**4.000**	**4.000**	**4.000**

ANNEX 3

AMPHIBOLE MINERAL CHEMISTRY

ANNEX 3 AMPHIBOLE MINERAL CHEMISTRY

	Incahuasi granodiorite (IG)						
	ay01-2-1	**ay12-1a**	**ay12-1b**	**ay12-3a**	**ay12-3b**	**ay45-3a**	**ay45-3b**
SiO_2	52.314	48.757	48.513	52.818	51.915	48.005	47.92
TiO_2	0.928	1.023	1.159	0.929	0.923	1.145	0.927
Al_2O_3	5.058	7.042	7.166	4.773	4.215	7.624	7.072
FeO	12.402	13.845	14.27	12.887	13.025	14.415	14.326
MnO	0.612	0.573	0.748	0.789	0.85	0.637	0.713
MgO	15.067	14.354	13.932	15.668	15.537	13.409	13.77
CaO	12.615	11.881	12.048	12.091	11.819	11.639	11.323
Na_2O	1.008	1.59	1.687	1.12	0.986	1.44	1.378
K_2O	0.255	0.487	0.547	0.339	0.31	0.529	0.483
BaO	0.015	0.052	0.052	0	0	0.015	0
Cr_2O_3	0	0.046	0	0.018	0.009	0.083	0
NiO	0	0	0	0	0	0	0
H2O*	2.08	2.05	2.06	2.13	2.09	2.03	2.02
Cl	0.06	0.067	0.089	0.03	0.037	0.065	0.078
F	0.058	0.03	0.006	0.011	0	0.024	0
Total	102.436	101.797	102.273	103.605	101.719	101.063	100.012
Si	7.37	6.94	6.92	7.31	7.31	6.90	6.92
Al iv	0.63	1.06	1.08	0.69	0.69	1.10	1.08
Sitio T	**8.00**	**8.00**	**8.00**	**8.00**	**8.00**	**8.00**	**8.00**
Al vi	0.21	0.12	0.12	0.09	0.01	0.19	0.12
Ti	0.10	0.11	0.12	0.10	0.10	0.12	0.10
Cr	0.00	0.01	0.00	0.00	0.00	0.01	0.00
Fe^{3+}	0.10	0.56	0.46	0.47	0.60	0.58	0.79
Fe^{2+}	1.36	1.09	1.24	1.03	0.93	1.15	0.94
Mn	0.07	0.07	0.09	0.09	0.10	0.08	0.09
Mg	3.16	3.05	2.96	3.23	3.26	2.87	2.96
Sitio C	**5.00**	**5.00**	**5.00**	**5.00**	**5.00**	**5.00**	**5.00**
Ca	1.90	1.81	1.84	1.79	1.78	1.79	1.75
Na	0.10	0.19	0.16	0.21	0.22	0.21	0.25
Sitio B	**2.00**	**2.00**	**2.00**	**2.00**	**2.00**	**2.00**	**2.00**
Na	0.18	0.25	0.31	0.09	0.05	0.19	0.14
K	0.05	0.09	0.10	0.06	0.06	0.10	0.09
Sitio A	**0.22**	**0.34**	**0.41**	**0.15**	**0.11**	**0.29**	**0.23**
OH*	1.96	1.97	1.98	1.99	1.99	1.97	1.98
Cl	0.01	0.02	0.02	0.01	0.01	0.02	0.02
F	0.03	0.01	0.00	0.00	0.00	0.01	0.00
(Ca+Na) (B)	2.00	2.00	2.00	2.00	2.00	2.00	2.00
Na (B)	0.10	0.19	0.16	0.21	0.22	0.21	0.25
(Na+K) (A)	0.22	0.34	0.41	0.15	0.11	0.29	0.23
$Mg/(Mg+Fe^{2+})$	0.70	0.74	0.70	0.76	0.78	0.71	0.76

ANNEX 3 AMPHIBOLE MINERAL CHEMISTRY

	Incahuasi granodiorite (IG)				Intrusive interm. dykes and enclaves (IIDE)		
	ay45-2a	**ay45-2b**	**ay45-1a**	**ay45-1b**	**ay03-3-1**	**ay23b-2-1**	**ay23b-3a**
SiO_2	47.132	48.459	47.273	46.948	49.824	48.185	48.492
TiO_2	1.094	1.119	1.114	1.041	1.089	1.223	1.128
Al_2O_3	8.203	6.89	8.315	7.602	6.9	8.077	7.737
FeO	15.084	14.445	15.32	14.352	14.126	14.512	14.353
MnO	0.605	0.726	0.642	0.611	0.667	0.65	0.567
MgO	13.019	13.608	12.504	13.134	13.19	13.258	13.529
CaO	11.348	11.478	11.676	11.96	12.035	11.691	11.081
Na_2O	1.592	1.501	1.643	1.36	1.393	1.564	1.819
K_2O	0.508	0.384	0.509	0.487	0.186	0.585	0.557
BaO	0	0	0	0.045	0.015	0.104	0.134
Cr_2O_3	0	0.006	0	0.037	0.001	0	0.016
NiO	0	0	0	0	0	0	0
H2O*	1.99	2.04	2.00	1.96	2.05	2.06	2.03
Cl	0.091	0.074	0.094	0.078	0.063	0.067	0.085
F	0.066	0	0.056	0.094	0.033	0	0.051
Total	100.686	100.728	101.147	99.712	101.575	101.977	101.577
Si	6.80	6.97	6.84	6.87	7.13	6.88	6.92
Al iv	1.20	1.03	1.16	1.13	0.87	1.12	1.08
Sitio T	**8.00**	**8.00**	**8.00**	**8.00**	**8.00**	**8.00**	**8.00**
Al vi	0.19	0.14	0.25	0.18	0.30	0.24	0.22
Ti	0.12	0.12	0.12	0.11	0.12	0.13	0.12
Cr	0.00	0.00	0.00	0.00	0.00	0.00	0.00
Fe^{3+}	0.73	0.63	0.50	0.48	0.22	0.50	0.61
Fe^{2+}	1.09	1.11	1.35	1.28	1.47	1.24	1.10
Mn	0.07	0.09	0.08	0.08	0.08	0.08	0.07
Mg	2.80	2.92	2.70	2.87	2.81	2.82	2.88
Sitio C	**5.00**	**5.00**	**5.00**	**5.00**	**5.00**	**5.00**	**5.00**
Ca	1.75	1.77	1.81	1.88	1.85	1.79	1.69
Na	0.25	0.23	0.19	0.12	0.15	0.21	0.31
Sitio B	**2.00**	**2.00**	**2.00**	**2.00**	**2.00**	**2.00**	**2.00**
Na	0.20	0.19	0.27	0.26	0.23	0.22	0.20
K	0.09	0.07	0.09	0.09	0.03	0.11	0.10
Sitio A	**0.29**	**0.26**	**0.36**	**0.35**	**0.27**	**0.33**	**0.30**
OH*	1.95	1.98	1.95	1.94	1.97	1.98	1.96
Cl	0.02	0.02	0.02	0.02	0.02	0.02	0.02
F	0.03	0.00	0.03	0.04	0.02	0.00	0.02
(Ca+Na) (B)	2.00	2.00	2.00	2.00	2.00	2.00	2.00
Na (B)	0.25	0.23	0.19	0.12	0.15	0.21	0.31
(Na+K) (A)	0.29	0.26	0.36	0.35	0.27	0.33	0.30
$Mg/(Mg+Fe^{2+})$	0.72	0.72	0.67	0.69	0.66	0.70	0.72

ANNEX 3 AMPHIBOLE MINERAL CHEMISTRY

	Intrusive interm. dykes and enclaves (IIDE)			Basaltic dyke (BD)	
	ay23b-3b	**ay40-2a**	**ay40-2b**	**ay42-1a**	**ay42-1b**
SiO_2	49.362	47.48	45.187	41.27	41.633
TiO_2	0.954	0.928	2.337	2.144	2.106
Al_2O_3	6.88	6.469	9.505	13.925	13.419
FeO	14.09	13.766	14.243	8.877	8.951
MnO	0.648	0.582	0.548	0.07	0.115
MgO	14.343	14.25	12.466	14.955	15.324
CaO	10.851	11.675	12.121	12.584	13.141
Na_2O	1.47	1.344	2.116	2.836	2.757
K_2O	0.351	0.256	0.4	0.275	0.41
BaO	0.104	0.016	0.007	0.074	0.084
Cr_2O_3	0.01	0	0	0.023	0.018
NiO	0	0	0	0	0
H2O*	2.05	1.97	2.01	2.00	2.06
Cl	0.085	0.039	0.013	0	0
F	0.003	0.08	0.078	0.093	0
Total	101.185	98.858	101.027	99.124	100.013
Si	6.98	6.93	6.59	6.02	6.05
Al iv	1.02	1.07	1.41	1.98	1.95
Sitio T	**8.00**	**8.00**	**8.00**	**8.00**	**8.00**
Al vi	0.13	0.04	0.23	0.42	0.35
Ti	0.10	0.10	0.26	0.24	0.23
Cr	0.00	0.00	0.00	0.00	0.00
Fe^{3+}	0.92	0.74	0.20	0.29	0.19
Fe^{2+}	0.75	0.94	1.53	0.79	0.90
Mn	0.08	0.07	0.07	0.01	0.01
Mg	3.02	3.10	2.71	3.25	3.32
Sitio C	**5.00**	**5.00**	**5.00**	**5.00**	**5.00**
Ca	1.64	1.83	1.89	1.97	2.05
Na	0.36	0.17	0.11	0.03	0.00
Sitio B	**2.00**	**2.00**	**2.00**	**2.00**	**2.05**
Na	0.05	0.21	0.49	0.77	0.78
K	0.06	0.05	0.07	0.05	0.08
Sitio A	**0.11**	**0.25**	**0.57**	**0.82**	**0.85**
OH*	1.98	1.95	1.96	1.96	2.00
Cl	0.02	0.01	0.00	0.00	0.00
F	0.00	0.04	0.04	0.04	0.00
(Ca+Na) (B)	2.00	2.00	2.00	2.00	2.05
Na (B)	0.36	0.17	0.11	0.03	0.00
(Na+K) (A)	0.11	0.25	0.57	0.82	0.85
$Mg/(Mg+Fe^{2+})$	0.80	0.77	0.64	0.80	0.79

ANNEX 3 AMPHIBOLE MINERAL CHEMISTRY

	Porphyritic granodiorite (PG)						
	ay9 c4-6	**ay13 c1-1**	**ay13 c1-2**	**ay13 c1-5**	**ay13 c2-2**	**ay13 c2-6**	**ay13 c3-2**
SiO_2	47.867	52.997	50.411	49.733	51.099	49	51.751
TiO_2	0	0	0	0	0	0	0
Al_2O_3	6.967	2.314	4.143	4.635	3.7	4.862	3.189
FeO	13.079	10.313	12.17	13.026	11.929	13.265	11.619
MnO	2.799	1.244	1.997	4.96	4.653	1.868	0.746
MgO	14.474	17.351	15.788	15.8	16.127	15.11	16.594
CaO	11.49	11.685	11.312	11.245	11.566	11.087	11.706
Na_2O	0.96	0.415	0.866	0.953	0.768	1.194	0.62
K_2O	0.485	0.154	0.257	0.369	0.261	0.352	0.226
BaO	0.044	0	0.067	0	0	0	0.091
Cr_2O_3	0	0.007	0.027	0.046	0.003	0.023	0
NiO	0	0	0	0	0	0	0
H_2O*	2.02	2.04	2.03	2.04	2.07	2.00	1.97
Cl	0.086	0.044	0.045	0.033	0.054	0.025	0.036
F	0	0.034	0.008	0.074	0	0.042	0.157
Total	100.250	98.599	99.119	102.911	102.232	98.823	98.705
Si	6.84	7.55	7.22	6.89	7.11	7.08	7.43
Al iv	1.16	0.45	0.78	1.11	0.89	0.92	0.57
Sitio T	**8.00**	**8.00**	**8.00**	**8.00**	**8.00**	**8.00**	**8.00**
Al vi	0.01	0.00	0.00	0.00	0.00	0.00	0.00
Ti	0.00	0.00	0.00	0.00	0.00	0.00	0.00
Cr	0.00	0.00	0.00	0.01	0.00	0.00	0.00
Fe^{3+}	1.27	0.81	1.08	1.81	1.47	1.17	0.79
Fe^{2+}	0.30	0.36	0.30	0.00	0.00	0.34	0.58
Mn	0.34	0.15	0.24	0.58	0.55	0.23	0.09
Mg	3.08	3.68	3.37	3.26	3.35	3.26	3.55
Sitio C	**5.00**	**5.00**	**5.00**	**5.66**	**5.36**	**5.00**	**5.00**
Ca	1.76	1.78	1.74	1.67	1.72	1.72	1.80
Na	0.24	0.22	0.26	0.33	0.28	0.28	0.20
Sitio B	**2.00**	**2.00**	**2.00**	**2.00**	**2.00**	**2.00**	**2.00**
Na	0.03	0.00	0.00	0.00	0.00	0.05	0.00
K	0.09	0.03	0.05	0.07	0.05	0.06	0.04
Sitio A	**0.11**	**0.03**	**0.04**	**0.07**	**0.05**	**0.12**	**0.04**
OH*	1.98	1.97	1.99	1.96	1.99	1.97	1.92
Cl	0.02	0.01	0.01	0.01	0.01	0.01	0.01
F	0.00	0.02	0.00	0.03	0.00	0.02	0.07
(Ca+Na) (B)	2.00	2.00	2.00	2.00	2.00	2.00	2.00
Na (B)	0.24	0.22	0.26	0.33	0.28	0.28	0.20
(Na+K) (A)	0.11	0.03	0.04	0.07	0.05	0.12	0.04
$Mg/(Mg+Fe^{2+})$	0.91	0.91	0.92	1.00	1.00	0.91	0.86

ANNEX 3 AMPHIBOLE MINERAL CHEMISTRY

	Porphyritic granodiorite-diorite (PGD)						
	ay21 c1-2	**ay21 c1-5**	**ay21 c1-8**	**ay21 c3-1**	**ay21 c3-3**	**ay21 c4-6**	**ay21 c4-8**
SiO2	55.048	45.728	47.286	49.334	49.541	54.911	49.164
TiO2	0	0	0	0	0	0	0
Al2O3	3.757	9.445	6.641	4.847	4.61	3.146	4.908
FeO	11.576	14.736	14.422	13.228	13.066	9.565	13.706
MnO	0	0.517	1.723	3.03	2.199	0.346	1.568
MgO	16.777	12.847	13.829	15.409	14.935	19.162	14.693
CaO	11.883	11.317	11.674	11.805	11.748	12.025	11.416
Na2O	0.74	1.853	1.043	0.787	0.868	0.517	1.027
K2O	0.338	0.599	0.432	0.357	0.338	0.163	0.403
BaO	0.113	0	0.023	0.068	0.012	0	0
Cr2O3	0.017	0.002	0	0.008	0.034	0	0
NiO	0	0	0	0	0	0	0
H2O*	2.14	1.99	1.98	2.04	2.01	2.11	2.01
Cl	0.037	0.095	0.1	0.043	0.065	0.1	0.045
F	0	0	0.009	0	0.006	0.055	0
Total	102.421	99.127	99.163	100.958	99.436	102.099	98.942
Si	7.60	6.70	6.89	7.00	7.15	7.48	7.13
Al iv	0.40	1.30	1.11	1.00	0.85	0.52	0.87
Sitio T	**8.00**	**8.00**	**8.00**	**8.00**	**8.00**	**8.00**	**8.00**
Al vi	0.21	0.33	0.03	0.00	0.00	0.00	0.00
Ti	0.00	0.00	0.00	0.00	0.00	0.00	0.00
Cr	0.00	0.00	0.00	0.00	0.00	0.00	0.00
Fe3+	0.41	0.79	1.06	1.32	0.97	0.87	0.99
Fe2+	0.93	1.02	0.69	0.06	0.55	0.20	0.64
Mn	0.00	0.06	0.21	0.36	0.27	0.04	0.19
Mg	3.45	2.80	3.00	3.26	3.21	3.89	3.18
Sitio C	**5.00**	**5.00**	**5.00**	**5.00**	**5.00**	**5.00**	**5.00**
Ca	1.76	1.78	1.82	1.79	1.82	1.75	1.77
Na	0.24	0.22	0.18	0.21	0.18	0.25	0.23
Sitio B	**2.00**	**2.00**	**2.00**	**2.00**	**2.00**	**2.00**	**2.00**
Na	0.00	0.30	0.12	0.01	0.06	0.00	0.06
K	0.06	0.11	0.08	0.06	0.06	0.03	0.07
Sitio A	**0.06**	**0.41**	**0.20**	**0.08**	**0.12**	**0.03**	**0.14**
OH*	1.99	1.98	1.97	1.99	1.98	1.95	1.99
Cl	0.01	0.02	0.03	0.01	0.02	0.02	0.01
F	0.00	0.00	0.00	0.00	0.00	0.02	0.00
(Ca+Na) (B)	2.00	2.00	2.00	2.00	2.00	2.00	2.00
Na (B)	0.24	0.22	0.18	0.21	0.18	0.25	0.23
(Na+K) (A)	0.06	0.41	0.20	0.08	0.12	0.03	0.14
Mg/(Mg+Fe2+)	0.79	0.73	0.81	0.98	0.86	0.95	0.83

ANNEX 3 AMPHIBOLE MINERAL CHEMISTRY

	PGD	
	ay21 c5-3	**ay21 c5-4**
SiO_2	45.562	48.725
TiO_2	0	0
Al_2O_3	7.201	5.44
FeO	14.9	13.682
MnO	3.004	1.932
MgO	12.941	14.721
CaO	11.641	11.2
Na_2O	1.13	1.025
K2O	0.535	0.405
BaO	0	0.022
Cr_2O_3	0	0.006
NiO	0	0
H2O*	1.94	1.98
Cl	0.167	0.072
F	0	0.067
Total	98.983	99.272
Si	6.70	7.03
Al iv	1.30	0.97
Sitio T	**8.00**	**8.00**
Al vi	0.00	0.00
Ti	0.00	0.00
Cr	0.00	0.00
Fe^{3+}	1.25	1.20
Fe^{2+}	0.54	0.40
Mn	0.37	0.24
Mg	2.84	3.16
Sitio C	**5.00**	**5.00**
Ca	1.84	1.73
Na	0.16	0.27
Sitio B	**2.00**	**2.00**
Na	0.16	0.02
K	0.10	0.07
Sitio A	**0.26**	**0.09**
OH*	1.96	1.95
Cl	0.04	0.02
F	0.00	0.03
(Ca+Na) (B)	2.00	2.00
Na (B)	0.16	0.27
(Na+K) (A)	0.26	0.09
$Mg/(Mg+Fe^{2+})$	0.84	0.89

ANNEX 4

LA-ICPMS U-Pb ZIRCON DATA

Annex 4. LA-ICPMS U-Pb zircon data of the studied samples.

Spot	Th/U	^{206}Pbc (%)	^{206}Pb/^{204}Pb	^{207}Pb/^{235}U	error (%)	^{206}Pb/^{238}U	error (%)	^{207}Pb/^{206}Pb	error (%)	err. corr. (ρ)	^{207}Pb/^{235}U age (Ma)	error (Ma)	^{206}Pb/^{238}U age (Ma)	error (Ma)	^{207}Pb/^{206}Pb age (Ma)	error (Ma)	conc. (%)
Sample AY-45 (Incahuasi granodiorite)																	
Z1	0.33	0.436	4263.4	0.0689	1.6	0.011	0.7	0.0462	1.4	0.3754	67.6	1.0	69.3	0.5	9.2	34.5	752
Z5	0.32	0.557	3339.2	0.0598	1.5	0.011	0.5	0.0397	1.4	0.2454	59.0	0.9	70.0	0.3	367.6	36.6	19
Z3	0.34	0.438	4242.3	0.0651	2.1	0.011	0.5	0.0432	2.0	0.2122	64. 0	1.3	70.1	0.4	157.2	48.7	45
Z2	0.44	0.527	5489.7	0.0722	1.7	0.011	0.9	0.0471	1.4	0.5055	70.8	1.1	71.3	0.6	53.3	33.9	134
Z6	0.33	1.027	5093.7	0.0720	0.9	0.011	0.6	0.0470	0.7	0.5582	70.6	0.6	71.3	0.4	46.9	16.8	152
Z4	0.39	0.221	8398.8	0.0722	1.0	0.011	0.5	0.0467	0.8	0.4882	70.8	0.7	71.9	0.4	31.6	19.3	228
Z16	0.37	0.795	2339.7	0.0639	1.2	0.012	0.5	0.0403	1.1	0.3317	62.9	0.8	73.7	0.4	331.0	28.6	22
Z15	0.39	0.386	4812.2	0.0688	1.2	0.012	0.5	0.0431	1.1	0.3502	67.5	0.8	74.2	0.4	162.0	26.2	46
Z8	0.27	0.401	4640.3	0.0731	1.2	0.012	0.4	0.0455	1.1	0.2724	71.6	0.8	74.6	0.3	27.3	26.9	273
Z17	0.38	0.354	5250.9	0.0742	0.9	0.012	0.6	0.0460	0.7	0.5724	72.7	0.6	75.0	0.4	0.6	16.3	12824
Z12	0.37	0.372	4993.9	0.0724	0.9	0.012	0.5	0.0447	0.7	0.4257	71.0	0.6	75.4	0.3	74.7	17.7	101
Z11	0.42	0.265	7007.8	0.0735	1.0	0.012	0.4	0.0452	0.9	0.3140	72.0	0.7	75.6	0.3	44.8	21.7	169
Z13	0.44	2.199	845.0	0.0784	1.6	0.012	0.5	0.0481	1.5	0.2546	76.6	1.2	75.7	0.4	105.1	35.2	72
Z14	0.34	0.637	7538.3	0.0881	1.0	0.012	0.5	0.0540	0.9	0.4110	85.7	0.9	75.8	0.4	372.4	20.4	20
Z19	0.40	0.802	2319.0	0.0701	1.2	0.012	0.5	0.0429	1.1	0.3064	68.8	0.8	76.0	0.4	174.3	27.3	44
Z10	0.34	1.087	3556.8	0.0619	0.8	0.012	0.4	0.0376	0.6	0.4401	61.0	0.5	76.5	0.3	512.0	16.5	15
Z31	0.39	0.854	2175.1	0.0705	1.1	0.012	0.4	0.0426	1.0	0.3027	69.2	0.7	77.0	0.3	192.4	25.1	40
Z23	0.39	0.372	4999.7	0.0765	1.2	0.012	0.5	0.0458	1.1	0.3322	74.9	0.9	77.6	0.4	12.0	27.3	645
Z30	0.38	0.329	10722.2	0.0789	1.0	0.012	0.5	0.0463	0.8	0.3919	77.1	0.7	79.2	0.4	12.0	20.2	658
Z22	0.58	0.315	18942.3	0.0823	1.7	0.012	0.5	0.0480	1.7	0.2064	80.3	1.4	79.6	0.4	101.7	39.8	78
Z32	0.29	0.701	2652.4	0.0722	1.2	0.013	0.6	0.0419	1.1	0.4277	70.8	0.8	80.1	0.5	234.8	26.6	34
Z24	0.56	0.166	11179.1	0.0780	1.0	0.013	0.7	0.0446	0.6	0.7266	76.3	0.7	81.3	0.6	76.3	15.6	107
Z20	0.41	0.258	7186.0	0.0840	0.6	0.013	0.5	0.0455	0.4	0.6156	81.9	0.5	85.8	0.4	30.2	10.8	284

It continues next page

Annex 4. *(Continued).*

Spot	U ppm	Th ppm	Th/ U	^{206}Pb$_c$ (%)	^{206}Pb/ ^{204}Pb	^{207}Pb/ ^{235}U	error (%)	^{206}Pb/ ^{238}U	error (%)	^{207}Pb/ ^{206}Pb	error (%)	err. corr. (ρ)	^{207}Pb/^{235}U age (Ma)	error (Ma)	^{206}Pb/^{238}U age (Ma)	error (Ma)	^{207}Pb/^{206}Pb age (Ma)	error (Ma)	conc. (%)
Sample AY-22 (Porphyritic granodiorite)																			
Z35	590	217	0.37	0.042	43769.0	0.0757	1.6	0.0110	0.4	0.0500	1.6	0.2004	74.1	1.2	70.5	0.3	193.9	36.4	36
Z40	909	446	0.49	0.031	59647.3	0.0755	1.0	0.0110	0.4	0.0497	0.9	0.5549	74.0	0.7	70.7	0.3	181.6	21.3	39
Z24	2634	1165	0.44	0.008	222699.4	0.0732	1.0	0.0111	0.5	0.0476	0.8	0.6652	71.7	0.7	71.5	0.3	79.2	20.1	90
Z25	352	121	0.34	0.037	50541.4	0.0754	1.1	0.0112	0.5	0.0488	1.0	0.4238	73.9	0.8	71.8	0.3	139.5	22.4	51
Z38	1049	520	0.50	0.017	88154.3	0.0766	0.7	0.0115	0.4	0.0485	0.6	0.5273	75.0	0.5	73.5	0.3	122.1	13.8	60
Z7	422	119	0.28	0.028	65890.9	0.0773	0.9	0.0115	0.5	0.0487	0.8	0.5133	75.6	0.7	73.8	0.4	133.4	19.1	55
Z15	541	293	0.54	0.026	72553.7	0.0794	0.9	0.0115	0.4	0.0499	0.8	0.4108	77.5	0.7	73.9	0.3	192.3	19.1	38
Z27	645	301	0.47	0.006	288585.7	0.0784	0.8	0.0115	0.4	0.0493	0.7	0.4749	76.7	0.6	73.9	0.3	164.2	16.7	45
Z21	766	321	0.42	0.024	78352.4	0.0771	0.9	0.0116	0.5	0.0484	0.8	0.5370	75.4	0.6	74.1	0.4	117.5	17.7	63
Z30	566	236	0.42	0.023	62284.7	0.0795	0.9	0.0116	0.4	0.0499	0.8	0.4070	77.7	0.7	74.1	0.3	188.8	19.2	39
Z11	949	536	0.57	0.015	127221.4	0.0781	0.7	0.0116	0.4	0.0487	0.6	0.5737	76.3	0.5	74.5	0.3	135.2	13.0	55
Z13	1238	465	0.38	0.024	77650.2	0.0802	1.8	0.0116	0.6	0.0500	1.7	0.3213	78.4	1.3	74.6	0.4	194.5	39.0	38
Z4	2730	1732	0.63	0.005	364985.7	0.0770	0.8	0.0117	0.4	0.0477	0.8	0.5739	75.4	0.6	75.1	0.3	84.0	18.1	89
Z20	968	547	0.56	0.017	110538.5	0.0808	1.1	0.0117	0.4	0.0499	1.0	0.5511	78.9	0.8	75.3	0.3	189.5	23.6	40
Z23	1212	1173	0.97	0.011	173942.6	0.0794	0.8	0.0118	0.5	0.0486	0.6	0.6208	77.6	0.6	75.9	0.4	130.1	14.9	58
Z9	767	339	0.44	0.014	130409.0	0.0802	0.7	0.0119	0.5	0.0489	0.6	0.6606	78.3	0.6	76.3	0.4	141.0	13.7	54
Z5	553	190	0.34	0.020	93593.4	0.0797	0.8	0.0119	0.4	0.0484	0.7	0.5450	77.8	0.6	76.5	0.3	118.5	15.8	65
Z16	1405	905	0.64	0.013	147551.0	0.0830	1.0	0.0124	0.5	0.0486	0.8	0.7405	81.0	0.8	79.4	0.4	127.0	19.1	63
Z14	474	77	0.16	0.026	35831.2	0.0842	0.8	0.0124	0.5	0.0491	0.6	0.6865	82.0	0.6	79.6	0.4	153.6	13.8	52
Z36	462	162	0.35	0.032	58240.9	0.1049	1.6	0.0154	0.8	0.0494	1.5	0.7093	101.3	1.6	98.5	0.8	167.4	33.9	59
Z2	681	415	0.61	0.005	635887.7	0.3345	0.7	0.0468	0.5	0.0518	0.5	0.7979	293.0	1.7	294.9	1.4	278.1	10.8	106

It continues next page

Annex 4. *(Continued).*

Spot	U ppm	Th ppm	Th/U	^{206}Pbc (%)	^{206}Pb/^{204}Pb	^{207}Pb/^{235}U	error (%)	^{206}Pb/^{238}U	error (%)	^{207}Pb/^{206}Pb	error (%)	err. corr. (ρ)	^{207}Pb/^{235}U age (Ma)	error (Ma)	^{206}Pb/^{238}U age (Ma)	error (Ma)	^{207}Pb/^{206}Pb age (Ma)	error (Ma)	conc. (%)
Sample AY-21 (Porphyritic granodiorite-diorite)																			
Z19	119	31	0.26	0.09	21647.0	0.0718	1.1	0.0106	0.6	0.0489	1.0	0.5159	70.4	0.8	68.2	0.4	145.0	22.7	47
Z20	197	54	0.28	0.05	39100.0	0.0706	1.3	0.0106	0.6	0.0482	1.2	0.6681	69.3	0.9	68.1	0.4	109.8	27.7	62
Z23	86	28	0.32	0.11	17416.3	0.0686	1.0	0.0105	0.5	0.0475	0.8	0.5352	67.4	0.6	67.2	0.4	73.6	19.8	91
Z25	134	40	0.30	0.07	24977.8	0.0689	1.1	0.0106	0.6	0.0470	1.0	0.5395	67.6	0.7	68.1	0.4	50.9	23.0	134
Z34	127	35	0.27	0.11	10968.4	0.0757	1.2	0.0107	0.6	0.0513	1.0	0.4915	74.1	0.8	68.5	0.4	256.1	23.4	27
Z36	110	36	0.33	0.20	9470.1	0.0804	2.3	0.0112	0.7	0.0523	2.2	0.4977	78.5	1.7	71.5	0.5	298.4	50.3	24
Z7	343	130	0.38	0.05	38569.1	0.0751	1.2	0.0111	0.8	0.0492	0.8	0.7227	73.6	0.8	71.0	0.6	157.5	19.4	45
Z8	267	79	0.30	0.07	28163.9	0.0762	1.5	0.0112	0.5	0.0492	1.4	0.5247	74.5	1.1	71.9	0.4	159.1	32.9	45
Z10	482	162	0.34	0.03	36869.3	0.0765	0.8	0.0114	0.5	0.0488	0.7	0.5657	74.8	0.6	72.9	0.3	137.0	15.7	53
Z12	551	153	0.28	0.02	90831.5	0.0729	1.1	0.0108	0.7	0.0490	0.8	0.8680	71.5	0.7	69.3	0.5	145.5	18.1	48
Z13	326	115	0.35	0.04	52647.6	0.0714	1.0	0.0108	0.7	0.0480	0.7	0.7071	70.1	0.7	69.2	0.5	100.9	16.8	69
Z14	173	69	0.40	0.07	12665.3	0.0713	1.0	0.0105	0.6	0.0493	0.8	0.6032	69.9	0.7	67.3	0.4	161.6	19.1	42
Z21	109	36	0.33	0.08	23641.2	0.0690	1.1	0.0106	0.5	0.0474	0.9	0.5047	67.7	0.7	67.7	0.4	68.1	21.9	99
Z26	255	102	0.40	0.03	58258.3	0.0716	0.9	0.0109	0.5	0.0476	0.7	0.6414	70.2	0.6	69.9	0.4	79.8	16.4	88
Z27	633	128	0.20	0.01	138616.3	0.0815	0.8	0.0124	0.6	0.0478	0.5	0.8104	79.5	0.6	79.2	0.5	88.8	12.6	89
Z28	227	66	0.29	0.05	41176.7	0.0726	1.4	0.0109	0.5	0.0482	1.3	0.5893	71.1	1.0	70.0	0.4	110.1	30.8	64
Z29	817	824	1.01	0.01	143075.1	0.0788	1.1	0.0117	0.9	0.0491	0.7	0.8057	77.1	0.8	74.7	0.6	150.8	16.5	50
Z30	293	113	0.38	0.03	28010.4	0.0728	1.0	0.0110	0.7	0.0481	0.7	0.7200	71.3	0.7	70.4	0.5	102.1	16.5	69
Z31	246	77	0.31	0.04	44190.8	0.0720	1.0	0.0108	0.7	0.0483	0.7	0.7317	70.6	0.7	69.3	0.5	113.2	16.7	61
Z24	124	38	0.31	0.10	19572.3	0.0790	3.2	0.0105	0.6	0.0546	3.2	0.3244	77.2	2.4	67.4	0.4	395.1	70.7	17
Z2	238	74	0.31	0.08	23566.8	0.0810	1.2	0.0113	0.5	0.0521	1.1	0.4091	79.1	0.9	72.3	0.4	290.8	24.2	25
Z35	150	48	0.32	0.09	21100.2	0.0767	1.3	0.0107	0.6	0.0518	1.2	0.4566	75.0	1.0	68.9	0.4	276.5	26.6	25
Z17	82	25	0.30	0.13	13835.9	0.0748	1.4	0.0106	0.6	0.0510	1.2	0.4361	73.3	1.0	68.2	0.4	242.8	28.7	28
Z9	307	106	0.34	0.06	32296.5	0.0845	1.3	0.0121	0.5	0.0508	1.2	0.4041	82.4	1.0	77.2	0. 4	234.0	26.6	33

It continues next page

Annex 4. *(Continued).*

Spot	U ppm	Th ppm	Th/ U	^{206}Pbc (%)	^{206}Pb/ ^{204}Pb	^{207}Pb/ ^{235}U	Error (%)	^{206}Pb/ ^{238}U	error (%)	^{207}Pb/ ^{206}Pb	error (%)	err. corr. (ρ)	^{207}Pb/^{235}U age (Ma)	error (Ma)	^{206}Pb/^{238}U age (Ma)	error (Ma)	^{207}Pb/^{206}Pb age (Ma)	error (Ma)	conc. (%)
Z5	190	64	0.34	0.02	118337.4	0.0760	1.1	0.0111	0.5	0.0496	1.0	0.4510	74.4	0.8	71.3	0.4	175.0	23.1	41
Z38	211	94	0.45	0.15	16249.9	0.0743	1.0	0.0109	0.5	0.0494	0.9	0.4342	72.8	0.7	69.9	0.3	168.5	21.1	41
Z1	203	58	0.29	0.08	24303.1	0.0767	0.9	0.0113	0.4	0.0493	0.8	0.3847	75.0	0.7	72.4	0.3	161.6	19.4	45
Z6	285	92	0.32	0.13	20514.7	0.0755	0.9	0.0111	0.4	0.0491	0.8	0.4403	73.9	0.6	71.4	0.3	153.1	18.0	47
Z16	148	39	0.26	0.08	23735.7	0.0729	2.0	0.0108	0.5	0.0490	2.0	0.4431	71.4	1.4	69.2	0.4	148.8	45.9	46
Z3	291	95	0.33	0.06	29455.4	0.0744	0.9	0.0111	0.4	0.0488	0.8	0.4481	72.9	0.6	71.0	0.3	137.5	18.7	52
Z32	163	41	0.25	0.07	28206.6	0.0723	1.8	0.0108	0.5	0.0487	1.7	0.4781	70.8	1.2	69.0	0.4	134.3	41.0	51
Z40	160	47	0.29	0.13	14397.5	0.0711	2.4	0.0108	0.5	0.0480	2.3	0.3622	69.8	1.6	69.0	0.3	97.1	54.8	71
Z4	177	57	0.32	0.09	19614.4	0.0747	2.1	0.0113	0.5	0.0480	2.0	0.3977	73.2	1.5	72.5	0.4	97.4	47.2	74
Z39	213	67	0.31	0.21	8748.1	0.0683	1.0	0.0106	0.5	0.0466	0.9	0.4634	67.1	0.6	68.2	0.3	27.3	20.6	250
Z22	100	31	0.31	0.10	13955.6	0.0636	1.2	0.0103	0.5	0.0448	1.1	0.3930	62.6	0.8	66.0	0.3	64.6	27.7	102
Z11	322	96	0.30	0.06	30247.3	0.0664	1.4	0.0112	0.6	0.0430	1.3	0.3921	65.2	0.9	71.7	0.4	166.8	31.4	43

ANNEX 5

Lu-Hf ZIRCON DATA

Annex 5. Lu-Hf z ircon data

Sample	$^{176}Lu/^{177}Hf$	error (abs)	$^{176}Hf/^{177}Hf$	2σ	U-Pb Age (Ma)	$(^{176}Hf/^{177}Hf)t$	εHf(t)	1σ	TDM(Ga)
AY-21 (Porphyritic granodiorite-diorite)									
Z19	0.000780	0.000039	0.282853	0.000084	68	0.282852	3.88	0.2	0.56
Z20	0.000576	0.000028	0.282877	0.000060	68	0.282877	4.75	0.3	0.52
Z23	0.000591	0.000027	0.282829	0.000073	67	0.282828	3.02	0.2	0.59
Z25	0.001145	0.000055	0.282736	0.000102	68	0.282735	-0.28	0.0	0.73
Z34	0.000697	0.000028	0.282787	0.000144	69	0.282786	1.56	0.1	0.65
AY-22 (Porphyritic granodiorite)									
Z4	0.003354	0.000202	0.282757	0.000082	75	0.282752	0.51	0.0	0.74
Z5	0.001016	0.000034	0.282874	0.000042	77	0.282872	4.80	0.2	0.53
Z16	0.000624	0.000020	0.282924	0.000052	79	0.282923	6.65	0.3	0.46
Z21	0.000926	0.000057	0.282896	0.000066	74	0.282895	5.54	0.4	0.50
Z24	0.001411	0.000053	0.282819	0.000056	71	0.282817	2.70	0.1	0.61
Z25	0.001042	0.000047	0.282926	0.000070	72	0.282924	6.52	0.3	0.46
Z35	0.000690	0.000029	0.282899	0.000047	70	0.282898	5.56	0.3	0.49
Z40	0.000577	0.000015	0.282876	0.000052	71	0.282875	4.77	0.1	0.52

ANNEX 6

Sm-Nd AND Rb-Sr ISOTOPE DATA

Annex 6. Sm-Nd and Rb-Sr isotope data of the studied samples.

Sample	Sm (ppm)	Nd (ppm)	^{143}Nd/^{144}Ndi (2σ)	^{147}Sm/^{144}Nd	εNd(T)	TDM(Ga)	^{87}Sr/^{86}Sri (2σ)
AY 45	2.881	15.565	0.512704+/-3	0.112	1.296	0.520	0.70472+/-1
AY 21	2.968	16.066	0.512581+/-15	0.112	-1.109	0.700	0.70468+/-2
AY 22	3.056	17.209	0.512641+/-10	0.107	0.054	0.590	0.70469+/-1
AY 05	3.255	16.987	0.512614+/-17	0.116	-0.472	0.680	0.70455+/-1
AY 39	3.003	14.395	0.512709+/-5	0.126	1.392	0.590	0.70464+/-1
AY 19	3.413	18.569	0.512645+/-20	0.111	0.140	0.600	0.70459+/-1
AY 32	3.193	14.610	0.512589+/-20	0.132	-0.966	0.850	0.70451+/-1
AY 14	6.123	31.020	0.512519+/-13	0.119	-2.327	0.850	0.70778+/-1
AY 03	3.643	21.973	0.512604+/-20	0.100	-0.665	0.600	0.70464+/-1
AY 42	3.883	16.330	0.512653+/-12	0.144	0.288	0.850	0.70471+/-1
AY 40	2.706	12.223	0.512659+/-17	0.134	0.407	0.740	0.70461+/-1
AY 41E	5.587	26.319	0.512726+/-15	0.128	1.723	0.580	0.7045+/-2